

B U L L E T I N

DE LA SOCIÉTÉ DES SCIENCES  
ET DES LETTRES DE ŁÓDŹ

---

SÉRIE:  
RECHERCHES SUR LES DÉFORMATIONS

---

Volume LXVI, no. 1



# B U L L E T I N

## DE LA SOCIÉTÉ DES SCIENCES ET DES LETTRES DE ŁÓDŹ

---

### SÉRIE: RECHERCHES SUR LES DÉFORMATIONS

---

Volume LXVI, no. 1

Rédacteur en chef et de la Série: JULIAN ŁAWRYNOWICZ

Comité de Rédaction de la Série

Aleksandra BASZCZYŃSKA (Łódź), O. MARTIO (Helsinki),  
W. A. RODRIGUES, Jr. (Campinas, SP), B. SENDOV (Sofia), D. SHOIKHET (Karmiel),  
O. SUZUKI (Tokyo), M. VACCARO (Salerno), E. VESENTINI (Torino),  
L. WOJTCZAK (Łódź), Ilona ZASADA (Łódź), Yu. ZELINSKIĬ (Kyiv)

Secrétaire de la Série:  
EWELINA FRĄTCZAK



ŁÓDŹ 2016

LÓDZKIE TOWARZYSTWO NAUKOWE

PL-90-505 Łódź, ul. M. Curie-Skłodowskiej 11

tel. (42) 66-55-459, fax (42) 66 55 464

sprzedaż wydawnictw: tel. (42) 66 55 448, <http://sklep.ltn.lodz.pl>

e-mail: [biuro@ltn.lodz.pl](mailto:biuro@ltn.lodz.pl); <http://www.ltn.lodz.pl/>

REDAKCJA NACZELNA WYDAWNICTW  
LÓDZKIEGO TOWARZYSTWA NAUKOWEGO

Krystyna Czyżewska, Wanda M. Krajewska (redaktor naczelny),

Edward Karasiński, Henryk Piekarski, Jan Szymczak

© Copyright by Łódzkie Towarzystwo Naukowe, 2016

PL ISSN 0459–6854; e-ISSN 2450-9329

Wydanie 1.

Nakład 100 egz.

Skład komputerowy: Zofia Fijarczyk

Druk i oprawa: 2K Łódź sp. z o.o.

Łódź, ul. Płocka 35/45

[www.2k.com.pl](http://www.2k.com.pl), [2k@2k.com.pl](mailto:2k@2k.com.pl)

The journal appears in the bases *Copernicus* and *EBSCOhost*

## INSTRUCTION AUX AUTEURS

1. La présente Série du Bulletin de la Société des Sciences et des Lettres de Łódź comprend des communications du domaine des mathématiques, de la physique ainsi que de leurs applications liées aux déformations au sens large.
2. Toute communications est présentée à la séance d'une Commission de la Société par un des membres (avec deux opinions de spécialistes designés par la Rédaction). Elle doit lui être adressée directement par l'auteur.
3. L'article doit être écrit en anglais, français, allemand ou russe et débuté par un résumé en anglais ou en langue de la communication présentée. Dans tous les travaux écrits par des auteurs étrangers le titre et le résumé en polonais seront préparés par la rédaction. Il faut fournir le texte original qui ne peut contenir plus de 15 pages (plus 2 copies).
4. Comme des articles seront reproduits par un procédé photographique, les auteurs sont priés de les préparer avec soin. Le texte tapé sur un ordinateur de la classe IBM PC avec l'utilisation d'un imprimante de laser, est absolument indispensable. Il doit être tapé préféablement en *AMS-TEX* ou, exceptionnellement, en *Plain-TEX* ou *LATEX*. Après l'acceptation de texte les auteurs sont priés d'envoyer les disquettes (PC). Quelle que soient les dimensions des feuilles de papier utilisées, le texte ne doit pas dépasser un cadre de frappe de 12.3×18.7 cm (0.9 cm pour la page courante y compris). Les deux marges doivent être la même largeur.
5. Le nom de l'auteur (avec de prénom complet), écrit en italique sera placé à la 1ère page, 5.6 cm au dessous du bord supérieur du cadre de frappe; le titre de l'acticle, en majuscules d'orateur 14 points, 7.1 cm au dessous de même bord.
6. Le texte doit être tapé avec les caractères Times 10 points typographiques et l'interligne de 14 points hors de formules longues. Les résumés, les renvois, la bibliographie et l'adresse de l'auteurs doivent être tapés avec le petites caractères 8 points typographiques et l'interligne de 12 points. Ne laissez pas de "blancs" inutiles pour respecter la densité du texte. En commençant le texte ou une formule par l'alinéa il faut taper 6 mm ou 2 cm de la marge gauche, respectivement.
7. Les texte des thèorèmes, propositions, lemmes et corollaries doivent être écrits en italique.
8. Les articles cités seront rangés dans l'ordre alphabétique et précédés de leurs numéros placés entre crochets. Après les références, l'auteur indiquera son adress complète.
9. Envoi par la poste: protégez le manuscrit à l'aide de cartons.
10. Les auteurs recevront une copie de fascicule correspondant à titre gratuit.

Adresse de la Rédaction de la Série:  
Département de la Physique d'état solide  
de l'Université de Łódź  
Pomorska 149/153, PL-90-236 Łódź, Pologne

*Name and surname of the authors*

## **TITLE – INSTRUCTION FOR AUTHORS SUBMITTING THE PAPERS FOR BULLETIN**

### **Summary**

Abstract should be written in clear and concise way, and should present all the main points of the paper. In particular, new results obtained, new approaches or methods applied, scientific significance of the paper and conclusions should be emphasized.

*Keywords and phrases:*

### **1. General information**

The paper for BULLETIN DE LA SOCIÉTÉ DES SCIENCES ET DES LETTRES DE ŁÓDŹ should be written in LaTeX, preferably in LaTeX 2e, using the style (the file **bull.cls**).

### **2. How to prepare a manuscript**

To prepare the LaTeX 2e source file of your paper, copy the template file **instruction.tex** with **Fig1.eps**, give the title of the paper, the authors with their affiliations/addresses, and go on with the body of the paper using all other means and commands of the standard class/style ‘bull.cls’.

#### **2.1. Example of a figure**

Figures (including graphs and images) should be carefully prepared and submitted in electronic form (as separate files) in Encapsulated PostScript (EPS) format.



Fig. 1: The figure caption is located below the figure itself; it is automatically centered and should be typeset in small letters.

#### **2.2. Example of a table**

Tab. 1: The table caption is located above the table itself; it is automatically centered and should be typeset in small letters.

Description 1	Description 2	Description 3	Description 4
Row 1, Col 1	Row 1, Col 2	Row 1, Col 3	Row 1, Col 4
Row 2, Col 1	Row 2, Col 2	Row 2, Col 3	Row 2, Col 4

### 2.3. “Ghostwriting” and “guest authorship” are strictly forbidden

The printed version of an article is primary (comparing with the electronic version). Each contribution submitted is sent for evaluation to two independent referees before publishing.

## 3. How to submit a manuscript

Manuscripts have to be submitted in electronic form, preferably via e-mail as attachment files sent to the address **zofija@uni.lodz.pl**. If a whole manuscript exceeds 2 MB composed of more than one file, all parts of the manuscript, i.e. the text (including equations, tables, acknowledgements and references) and figures, should be ZIP-compressed to one file prior to transfer. If authors are unable to send their manuscript electronically, it should be provided on a disk (DOS format floppy or CD-ROM), containing the text and all electronic figures, and may be sent by regular mail to the address: **Department of Solid State Physics, University of Lodz, Bulletin de la Société des Sciences et des Lettres de Łódź, Pomorska 149/153, 90-236 Łódź, Poland.**

### References

[1]

Affiliation/Address

## TABLE DES MATIÈRES

1. <b>H. Puzzkarski</b> and <b>P. Tomczak</b> , Application of the surface pinning diagram to the study of existence conditions of surface spin-wave modes in (Ga, Mn)As thin films .....	11–16
2. <b>K. Szałowski</b> , <b>T. Balcerzak</b> , <b>M. Jaščur</b> , <b>A. Bobak</b> , and <b>M. Žukovič</b> , Thermodynamic properties of a Hubbard model on a cubic cluster – exact diagonalization study at quarter filling .....	17–28
3. <b>T. Ramírez Rodríguez</b> and <b>F. de L. Castillo Alvarado</b> , Analysis of the kinetics of decomposition of calcium carbonate for designing a hydrogen storage material .....	29–35
4. <b>Y. B. Zelinskii</b> , The problem of the shadows .....	37–42
5. <b>K. D. Gayan Maduranga</b> and <b>R. Abłamowicz</b> , Representations and characters of Salingaros’ vee groups of low order ....	43–74
6. <b>K. Podlaski</b> and <b>G. Wiatrowski</b> , Multi-objective optimization of vehicle routing problem using hybrid GA-PSO algorithm with modified best cost route crossover operator .....	75–91
7. <b>M. Moneta</b> , <b>M. Antoszevska-Moneta</b> , and <b>R. Brzozowski</b> , Heavy ions sputtering and implantation of surface monitored with PIXE .....	93–101
8. <b>E. Z. Frątczak</b> , <b>P. Uznański</b> , and <b>M. E. Moneta</b> , Molecular organization in pentacene thin film on SiO <sub>2</sub> surface using spectroscopic ellipsometry, infrared spectroscopy, and atomic force microscopy .....	103–122
9. <b>M. Nowak-Kępczyk</b> , An algebra governing reduction of quaternary structures to ternary structures III. A study of generators of the resulting algebra .....	123–133
10. <b>A. Baszczyńska</b> , Nonclassical parameters in kernel estimation	135–148
OBITUARY: Professor <b>Leon Mikołajczyk</b> .....	149



JUBILEE VOLUME LXV, no. 3 – LXVI, no. 2

**vol. LXVI, no. 1**

Série:

RECHERCHES SUR LES DÉFORMATIONS

*Guest Editor of the Volume*

ILONA ZASADA

*Ilona Zasada*

Ordinary Member of the  
Łódź Society of Sciences and Arts

Department of Solid State Physics  
Institute of Physics, University of Łódź  
Pomorska 149/153, PL-90-236 Łódź, Poland  
e-mail: izasada@wfis.uni.lodz.pl

## B U L L E T I N

DE LA SOCIÉTÉ DES SCIENCES ET DES LETTRES DE ŁÓDŹ

2016

Vol. LXVI

Recherches sur les déformations

no. 1

pp. 11–16

*Contribution to the jubilee volume, dedicated  
to Professors J. Lawrynowicz and L. Wojtczak*

*Henryk Puzkarski and Piotr Tomczak*

**APPLICATION OF THE SURFACE PINNING DIAGRAM  
TO THE STUDY OF EXISTENCE CONDITIONS  
OF SURFACE SPIN-WAVE MODES IN (Ga,Mn)As THIN FILMS**

**Summary**

Spin-wave resonance (SWR) is a newly emerged method for studying surface magnetic anisotropy and surface spin-wave modes in (Ga,Mn)As thin films. On the basis of recent SWR studies of (Ga,Mn)As thin films we show that the cubic surface anisotropy is an essential factor determining the configuration regions of existence of surface spin-wave modes. These proved to exist only for those directions of film magnetization that lie in the immediate vicinity of hard cubic anisotropy axes.

**Keywords and phrases:** *surface anisotropy, surface spin pinning, spin-wave resonance, (Ga,Mn)As thin films, surface pinning diagram*

**1. Introduction**

The existence of surface spin-wave modes (SSWMs) in (Ga,Mn)As thin films was first reported by Liu *et al.* [1], which observed SSWMs in both the out-of-plane configuration, with variable polar angle  $\vartheta_M$  between the magnetization of the film and its surface normal, and the in-plane configuration, with variable azimuth angle  $\varphi_M$  between the in-plane magnetization of the film and the [100] crystal axis. In the former case SSWMs only exist when the polar angle  $\vartheta_M$  is larger than a certain angle – the *out-of-plane critical angle* – while in the in-plane configuration SSWMs are observed in the azimuth angle range *between two in-plane critical angles*.

These experimental findings are interpreted theoretically in our recent papers [2–4], in which we propose an appropriate model of surface anisotropy that both explains the

existence of critical angles and allows to determine the conditions of existence of SSWMs in full agreement with the experimental data. In our model of surface anisotropy we use the concept of surface pinning parameter  $A_{surf}$ , which describes the freedom of precessing surface spins in relation to the freedom of precessing bulk spins. We have determined the functions  $A_{surf}(\vartheta_H)$  and  $A_{surf}(\varphi_M)$  describing the configuration dependence of the surface parameter in the out-of-plane and in-plane configurations, respectively. The explicit formula for the in-plane surface parameter reads [3]:

$$(1) \quad A_{surf}(\varphi_M) = 1 + a_{iso} + a_{uni} \sin^2(\varphi_M - 45^\circ) + a_{cub} [(3 + \cos 4\varphi_M) + (3 + \cos 4\varphi_M)^4].$$

We will use Eq. (1) as a basis for a pinning diagram construction.

In our model the critical angles are determined by the condition  $A_{surf}(\varphi_M) = 1$ , and the configuration angles for which SSWMs exist by the condition  $A_{surf}(\varphi_M) > 1$ . Based on these conditions, in the present paper we will discuss the impact of each of the surface anisotropy components appearing in Eq. (1), and provide a physical interpretation of their respective roles in the generation of SSWMs. To this end we will use a surface pinning diagram built in the polar coordinate system; using this pinning diagram we will obtain a graphical representation of the configuration dependence of the pinning felt by the surface spins.

## 2. Concept of surface pinning diagram

The proposed new tool that we have named the surface pinning diagram is a planar map showing how the dynamics of surface spins in a (Ga,Mn)As thin film changes with their orientation with respect to specific crystal axes that characterize the surface structure. The pinning diagram is based on a polar coordinate system lying in the plane of the film surface (see Fig. 1a). In this coordinate system the azimuth angle  $\varphi_M$  describes the orientation of the magnetization of the sample with respect to a reference axis, which is the [100] crystal axis; the distance between a point in the diagram and the pole of the coordinate system measures the value of the surface pinning parameter  $A_{surf} = A_{surf}(\varphi_M)$  corresponding to a given azimuth angle.

Introduced in papers [5, 6], the concept of surface pinning parameter  $A$  was proposed to describe the degree of freedom of surface spins in their precession. By definition the surface pinning parameter value  $A = 1$  corresponds to the natural freedom of the surface spins resulting from breaking their bonds with neighbors eliminated from the system by surface cut. This particular value of  $A$  divides the  $(A_{surf}(\varphi_M), \varphi_M)$  plane into two different regions: within the circle of radius  $A_{surf}(\varphi_M) = 1$ , where only bulk spin-wave modes exist, and region beyond this circle, in which SSWMs exist in the spectrum of allowed modes (see also [7, 8]). Against the pinning diagram in Fig. 1a we have added the crystal axes characterizing the magnetic anisotropy in the (Ga,Mn)As sample used in the spin-wave resonance (SWR) study [1] (in which the SWR measurements were performed in the (001) in-plane configuration).

## 3. Factors responsible for surface pinning

A satisfactory interpretation of the experimental SWR spectra obtained in the in-plane configuration [1] is achieved with the surface parameter described by the series presented above in equation (1) (found in an investigation discussed in detail in [3]) with the following values of the series coefficients  $a_{iso}$ ,  $a_{uni}$  and  $a_{cub}$ :

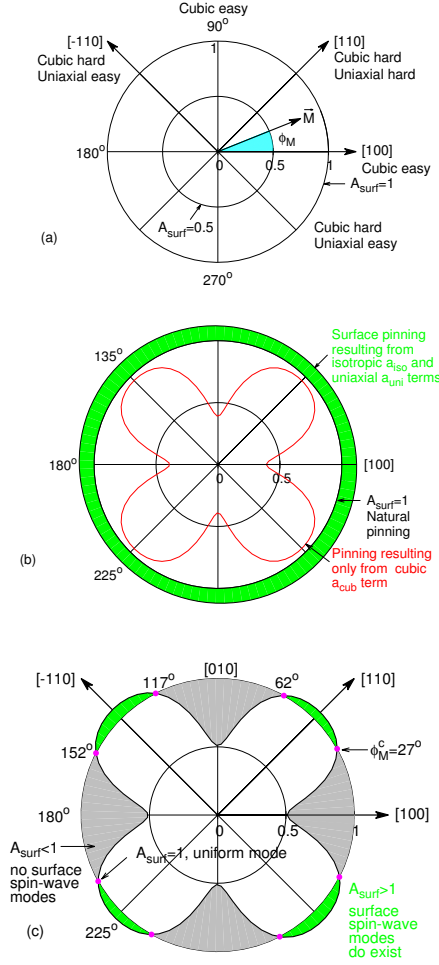


Fig. 1: Graphical representation of the evolution of the in-plane surface spin pinning in a (Ga,Mn)As thin film as described by Eq. (1) expressing the surface pinning parameter  $A_{surf}(\varphi_M)$  as a function of the in-plane azimuth magnetization angle  $\varphi_M$ . (a) The idea of *surface pinning diagram*: each point in the plane represents the surface pinning conditions described by a specific value of the surface pinning parameter  $A_{surf}(\varphi_M)$  corresponding to the given magnetization direction  $\varphi_M$ . The circle  $A_{surf}(\varphi_M) = 1$  corresponds to natural pinning conditions. (b) Configuration dependence of the surface spin pinning contributions resulting from two different factors considered separately (as indicated in the graph). (c) Magnetization angle dependence  $A_{surf}(\varphi_M)$  (solid line) of the in-plane full surface pinning parameter resulting from our model (see Eq. (1)); this theoretical curve is found to fit very well the experimental data obtained by Liu *et al.* [1]. Regions of existence of SSWMs under these full pinning conditions are marked in green.

$$(2) \quad a_{iso} = 0.1058; a_{uni} = 0.027; a_{cub} = -0.0023.$$

The series coefficients in equation (1) describe the contributions of different surface anisotropy components to the surface spin pinning in (Ga,Mn)As thin films:  $a_{iso}$  is the isotropic contribution to the pinning,  $a_{uni}$  is related to the uniaxial component, and  $a_{cub}$  describes the pinning due to the cubic anisotropy. Below we will use equations (1) and (2) as a basis for building our pinning diagram. First we will build a partial diagram, shown in Fig. 1b; then we will proceed to the full diagram, presented in Fig. 1c.

Figure 1b shows two curves, each representing the azimuth angle dependence of a part of surface pinning resulting from selected anisotropies – the total contribution of the isotropic and uniaxial anisotropies is analyzed independently of the pinning related to the cubic anisotropy. The first two contributions consonantly introduce the pinning to that region of the diagram in which SSWMs exist for any azimuth orientation (green ring in the diagram). In contrast, the pinning resulting from the cubic anisotropy, represented by a quadrifolium-like curve, is completely embedded in the region within the circle of radius  $A_{surf}(\varphi_M) = 1$ ; however, since the circle  $A_{surf}(\varphi_M) = 1$  corresponds to the natural pinning this implies that the cubic anisotropy alone will not induce SSWMs in any azimuth orientation. Thus, already at this point, before proceeding to the analysis of the full pinning diagram presented in Fig. 1c, we must realize that it will result from two above-mentioned opposite tendencies.

#### 4. Regions of SSWM existence vs. cubic surface anisotropy

As a result of the summation of the above-mentioned pinning contributions with different effects on the spins – one increasing their freedom, the other reducing it – in the full pinning diagram (Fig. 1c) the green ring is reduced to four islands that still remain within the region of surface mode existence. Each of these islands is associated with one hard cubic anisotropy axis, as indicated in Fig. 1a. Also, each island corresponds to an azimuth angle range between the two critical angles for which  $A_{surf}(\varphi_M) = 1$ ; each of these angle ranges surrounds symmetrically the cubic anisotropy axis. *It is in these azimuth angle ranges that SSWMs exist.* Beyond them the cubic anisotropy has a destructive effect on the surface modes; this destruction is apparent in regions symmetric with respect to the *easy cubic anisotropy axes*.

Now we can provide physical grounds to these observations. A hard magnetic axis is a direction in which spins are reluctant to align, and setting them in an equilibrium direction involves a high energy cost to the system. Thus, the opposite tendency – divergence from the hard axis – must be more favorable energetically. This implies that a *hard cubic anisotropy axis* plays the role of an *easy axis* for the *spin pinning*; we can refer to it as an *easy pinning axis*, i.e., an axis from which spins diverge easily, since their pinning along its direction is weaker. And vice versa: an *easy cubic anisotropy axis* defines a direction that spins are reluctant to quit (*hard pinning axis*).

Thus, the following final conclusion can be drawn from our considerations based on the pinning diagram: *in a (Ga,Mn)As thin film conditions favorable for the occurrence of surface spin-wave modes in the in-plane configuration are fulfilled first of all for those azimuth orientations of the magnetization of the sample that lie around the hard axes of cubic magnetic anisotropy.*

## Acknowledgements

This study is a part of a project financed by Narodowe Centrum Nauki (National Science Centre of Poland), Grant no. DEC-2013/08/M/ST3/00967.

## References

- [1] X. Liu, Y.-Y. Zhou, and J. K. Furdyna, *Angular dependence of spin-wave resonances and surface spin pinning in ferromagnetic (Ga,Mn)As films*, Phys. Rev. B **75** (2007), 195220.
- [2] H. Puzskarski and P. Tomczak, *Spin-Wave Resonance Model of Surface Pinning in Ferromagnetic Semiconductor (Ga,Mn)As Thin Films*, Sci. Rep. **4** (2014), 6135.
- [3] H. Puzskarski and P. Tomczak, *Spin-Wave Resonance in (Ga,Mn)As Thin Films: Probing in-plane surface magnetic anisotropy*, Phys. Rev. B **91** (2015), 195437.
- [4] H. Puzskarski and P. Tomczak, *Model for the Surface Anisotropy Field Observed in Spin-Wave Resonance in (Ga,Mn)As Thin Films*, Acta Phys. Polon. A **127** (2015), 508.
- [5] H. Puzskarski, *Quantum Theory of Spin Wave Resonance in Thin Ferromagnetic Films. Part I: Spin Waves in Thin Films, Part 2: Spin-Wave Resonance Spectrum*, Acta Phys. Polon. A **38** (1970), 217 and 899.
- [6] H. Puzskarski, *Theory of Surface States in Spin Wave Resonance*, Progr. Surf. Sci. **9** (1979), 191.
- [7] L. Wojtczak, *Cienkie warstwy magnetyczne*, Wydawnictwo Uniwersytetu Łódzkiego, Łódź 2009.
- [8] A. Urbaniak-Kucharczyk, *The Coherent Potential Approximation in the Description of Spin Wave Resonance*, Phys. Status Solidi B **189** (1995), 239.

Surface Physics Division, Faculty of Physics  
Adam Mickiewicz University  
Umultowska 85, PL-61-614 Poznań  
Poland  
e-mail: henpusz@amu.edu.pl  
ptomczak@amu.edu.pl

Presented by Marek Moneta at the Session of the Mathematical-Physical Commission of the Łódź Society of Sciences and Arts on October 29, 2015

## ZASTOSOWANIE DIAGRAMU PRZYPIĘCIA POWIERZCHNIOWEGO DO STUDIUM WARUNKÓW ISTNIENIA SPINOWO-FALOWYCH MODÓW POWIERZCHNIOWYCH W CIENKICH WARSTWACH (Ga,Mn)As

### Streszczenie

Rezonans spinowo-falowy (SWR) stwarza nową metodę badania powierzchniowej anizotropii magnetycznej i spinowo-falowych modów powierzchniowych w cienkich warstwach

(Ga,Mn)As. Na podstawie niedawnych badań SWR cienkich warstw (Ga,Mn)As wykazujemy, że sześcienna powierzchnia anizotropii jest zasadniczym czynnikiem określającym konfigurację obszarów istnienia spinowo-falowych modów powierzchniowych. Wykazujemy istnienie ich tylko w przypadkach takich kierunków magnetyzacji warstw, które są położone w bezpośrednim sąsiedztwie ustalonych sześciennych osi anizotropii.

*Słowa kluczowe:* anizotropia powierzchniowa, spinowe przypięcie powierzchniowe, rezonans spinowo-falowy, cienkie warstwy (Ga,Mn)As, diagram przypięcia powierzchniowego



## B U L L E T I N

DE LA SOCIÉTÉ DES SCIENCES ET DES LETTRES DE ŁÓDŹ

2016

Vol. LXVI

Recherches sur les déformations

no. 1

pp. 17–28

*Contribution to the jubilee volume, dedicated  
to Professors J. Lawrynowicz and L. Wojtczak*

*Karol Szalowski, Tadeusz Balcerzak,  
Michal Jaščur, Andrej Bobák, and Milan Žukovič*

**THERMODYNAMIC PROPERTIES OF A HUBBARD MODEL  
ON A CUBIC CLUSTER – EXACT DIAGONALIZATION STUDY  
AT QUARTER FILLING**

**Summary**

We study the thermodynamics of a zero-dimensional, cubic cluster described with a Hubbard Hamiltonian, focusing our interest on the magnetic properties. The range in which the studied cluster is paramagnetic is considered. The results are obtained by means of exact numerical diagonalization. Such thermodynamic quantities as entropy, specific heat, magnetic susceptibility, spin-spin correlations and double occupancy are discussed. Particular emphasis is put on the behaviour of local maxima of specific heat and susceptibility, which are analysed in terms of Schottky anomalies.

*Keywords and phrases:* Hubbard model, entropy, specific heat, magnetic susceptibility, paramagnetism, exact diagonalization, Schottky anomaly

**1. Introduction**

Low-dimensional magnetic systems attract considerable theoretical and experimental efforts. Within this field, noticeable attention is paid to the theoretical studies of zero-dimensional magnetic clusters composed of a finite, small number of atoms [1–4]. Although the existence of magnetic ordering and magnetic phase transitions in low dimensions is severely limited, yet such systems can still exhibit a range of interesting properties.

Hubbard model [5–7] is one of the successful theoretical approaches involved, among others, in the studies of low-dimensional magnetic systems exhibiting strong correlations (to mention for example its early applications to magnetic thin films [8–10]). In spite of its simplicity, it still remains a challenge for theorists. In addition to various approximate approaches to its thermodynamics, a valuable method for this model is exact diagonalization [11], being essentially free from any artefacts, which feature is of huge importance due to the complicated phase diagram of the model. However, such method is computationally very demanding, therefore its applicability is limited only to the smallest systems. This feature allows to focus the interest on zero-dimensional clusters described by Hubbard model, the magnetic properties of which were studied for various geometries and numbers of charge carriers (filling levels of energy states) [12–20]. In particular, cubic cluster attracted some attention [13, 19, 20]. However, not all the thermodynamic properties related to magnetism were systematically explored, especially beyond the half-filling case.

The aim of the present paper is to provide a systematic discussion of thermodynamics of a cubic Hubbard cluster, selecting the case of quarter-filling of the energy states.

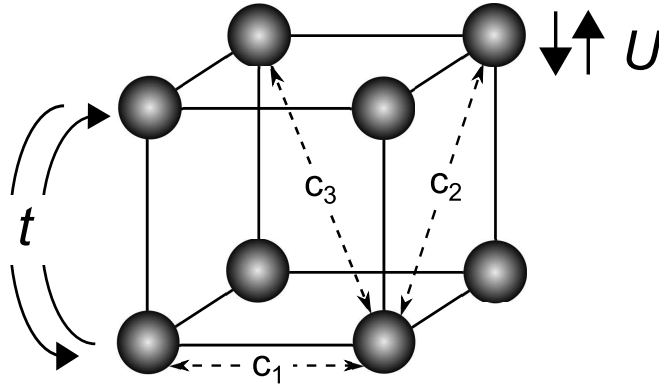


Fig. 1: A schematic view of a cubic cluster system described with a Hubbard Hamiltonian with the hopping integral  $t$  and on-site Coulombic energy  $U$ . The spin-spin correlations between first, second and third nearest neighbours are indicated with dashed lines.

## 2. Theoretical model

A schematic view of the system of interest is shown in Fig. 1. It is a zero-dimensional cluster in a form of a cube, having  $N = 8$  sites with hopping integral  $t$  between nearest neighbours only. The on-site Coulombic interaction energy is parametrized by the parameter  $U > 0$ . In our study we focus on the case with  $N_e = 4$  charge carriers (electrons) in the system, thus we deal with quarter-filling of the energy

states. Let us remind that such a molecular-like structure possesses a purely discrete energy spectrum, so we do not refer to band filling.

The system is described by the following Hubbard Hamiltonian:

$$(1) \quad \mathcal{H} = -t \sum_{\langle i,j \rangle} \sum_{\sigma=\uparrow,\downarrow} \left( c_{i,\sigma}^\dagger c_{j,\sigma} + c_{j,\sigma}^\dagger c_{i,\sigma} \right) + U \sum_i n_{i,\uparrow} n_{i,\downarrow},$$

in which  $c_{i,\sigma}^\dagger$  ( $c_{i,\sigma}$ ) creates (annihilates) an electron with spin  $\sigma$  at site labelled with  $i = 1, \dots, N$ , while  $n_{i,\sigma} = c_{i,\sigma}^\dagger c_{i,\sigma}$  is the number of electrons with spin  $\sigma$  at site  $i$ . Let us mention that  $z$ -component of the spin at site  $i$  is therefore equal to  $s_i^z = (n_{i,\uparrow} - n_{i,\downarrow})/2$ .

For the case of  $N = 8$  lattice sites with  $N_e = 4$  electrons, the Hilbert space for the studied system is spanned by

$$N_s = \frac{(2N)!}{N_e! (2N - N_e)!} = 1820$$

basis vectors. The resulting matrix ( $N_s \times N_s$ ) of the Hamiltonian  $\mathcal{H}$  for the given case can be exactly diagonalized numerically, what yields the eigenvalues and corresponding eigenvectors.

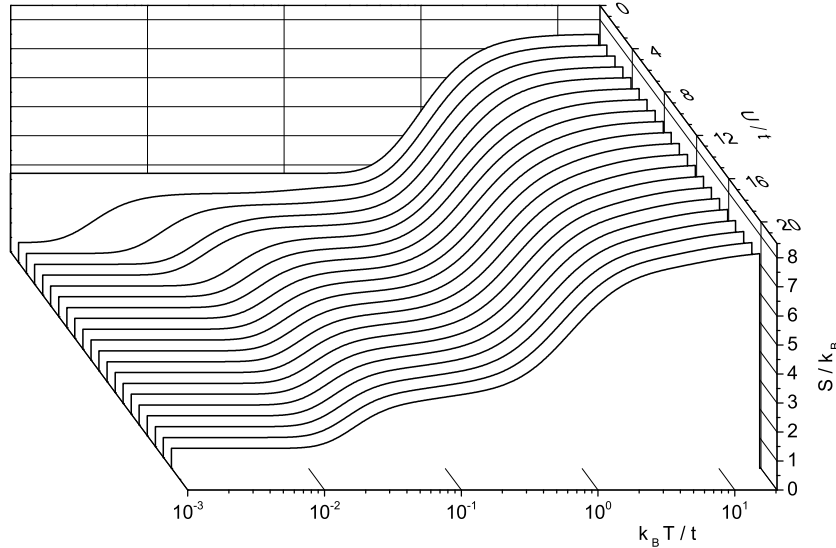


Fig. 2: The dependence of the system entropy on the normalized temperature for various values of normalized Coulombic interactions energy.

The exact thermodynamic description of our system was constructed basing on the canonical ensemble, with fixed number of electrons and temperature equal to  $T$ . The statistical operator describing the thermal state is:

$$(2) \quad \rho = \frac{1}{\mathcal{Z}} e^{-\beta \mathcal{H}},$$

where the statistical sum is given by:

$$(3) \quad \mathcal{Z} = \text{Tr} e^{-\beta \mathcal{H}} = \sum_k g_k e^{-\beta E_k},$$

$g_k$  being the degeneracy of the eigenstate with the energy equal to  $E_k$ , while  $\beta = 1/(k_B T)$  with  $k_B$  denoting the Boltzmann constant. The thermodynamic average of an arbitrary quantity  $A$  is equal to:

$$(4) \quad \langle A \rangle = \text{Tr} (\rho A).$$

Knowledge of the statistical operator and the statistical sum allows us to calculate all further thermodynamic quantities of interest, for instance, entropy, specific heat or magnetic susceptibility as well as magnetic correlations between first, second and third neighbours (see Fig. 1 for schematic explanation). In particular, specific heat  $C_h$  and magnetic susceptibility  $\chi_T$  can be determined conveniently using fluctuation-dissipation theorem, which yields:

$$(5) \quad C_h = k_B \beta^2 \left( \langle E^2 \rangle - \langle E \rangle^2 \right),$$

where

$$\langle E \rangle = \frac{1}{\mathcal{Z}} \sum_k g_k E_k e^{-\beta E_k}$$

is the internal energy and

$$(6) \quad \chi_T = \beta \left( \langle m^2 \rangle - \langle m \rangle^2 \right),$$

where

$$\langle m \rangle = \sum_{i=1}^N \langle s_i^z \rangle$$

is the average total magnetization.

The entropy is calculated from  $S = (\langle E \rangle - F)/T$ , where  $F = -k_B T \ln \mathcal{Z}$  is Helmholtz free energy. The spin-spin correlations are defined as  $c_k = \langle s_i^z s_j^z \rangle$ , where  $k = 1, 2, 3$  means that spin at site  $i$  is the  $k$ -th nearest neighbour of the spin at site  $j$  (see Fig. 1). Finally, the average double occupancy per site is expressed as

$$d = (1/N) \sum_{i=1}^N \langle n_{i,\uparrow} n_{i,\downarrow} \rangle.$$

In our calculations we found that the ground state (at  $T = 0$ ) is nonmagnetic, with total spin equal to  $S = 0$  if  $U/t \lesssim 223.7$ , what is in agreement with the results of Refs. [13, 19] (while for stronger Coulombic interactions  $U$  we deal with a ferromagnetic ground state). Since the critical strength of Coulombic interactions corresponds to extremely high  $U/t$  values, we limit our considerations to the range with zero total ground state spin, assuming  $0 \leq U/t \leq 50$ . We believe this range

is the most physically interesting and the thermodynamic properties of the cubic Hubbard cluster at quarter filling for this range were not systematically explored.

### 3. Numerical results and discussion

In this section we discuss the numerical calculations of such thermodynamic quantities as entropy, specific heat and magnetic susceptibility as well as spin correlation functions and double occupancy performed within canonical ensemble approach with exact numerical diagonalization of the Hubbard Hamiltonian. For the numerical calculations we used *Wolfram Mathematica* software [21].

The dependence of total entropy of the cubic cluster on the temperature is presented in Fig. 2 in logarithmic temperature scale, in a wide range of normalized Coulombic energies  $U/t$ . For  $U/t = 0$  (i.e. for a pure tight-binding model) a ground state exhibits 15-fold degeneracy, therefore, the entropy at  $T = 0$  reaches a noticeable residual value of  $k_B \ln 15 \simeq 2.708 k_B$ . On the contrary, for  $U/t > 0$  (in our  $U/t$  range of interest) the ground state is 2-fold degenerated, so that the residual entropy is reduced to  $k_B \ln 2 \simeq 0.693 k_B$ . The limiting, high-temperature entropy is in all cases  $k_B \ln 1820 \simeq 7.507 k_B$ . In Fig. 2 it can be noticed that some low- and high-temperature ranges can be seen, in which entropy rises fast with the temperature, signaling high values of the specific heat.

The variation of specific heat with the temperature can be followed for a range of  $U/t$  values in Fig. 3. It is evident that in the absence of Coulombic interactions a single peak is present, at the temperature close to  $k_B T/t \simeq 1$ , and it remains in that position when the Coulombic interaction  $U/t$  is switched on. What is noticeable, appearance of  $U/t > 0$  causes a low-temperature specific heat maximum to emerge, as well as the significant shift of its position with the energy of Coulombic interactions, what can be clearly seen in Fig. 3.

Contrary to the specific heat, the magnetic susceptibility indicates only a single peak in its temperature dependence for  $U/t > 0$ , as presented in Fig. 4. The height of this maximum also significantly drops when Coulombic interactions become stronger, whereas both specific heat maxima show a rather constant height. It has been verified that the inverse of susceptibility shows a linear dependence on the temperature at high temperatures, what corresponds to Curie-Weiss law with positive (ferromagnetic) Curie-Weiss temperature (not shown in the plot); note that this fact does not imply the presence of magnetic ordering in our zero-dimensional system.

As both specific heat and magnetic susceptibility exhibit the presence of pronounced maxima, it is interesting to investigate their behaviour as a function of Coulombic interactions energy as well as to explain their origin.

The temperature values  $T_{\max}$  at which such quantities as the magnetic susceptibility and the specific heat of the studied system reach their local maxima are plotted in Fig. 5 as a function of reduced Coulombic on-site energy  $U/t$ . Let us

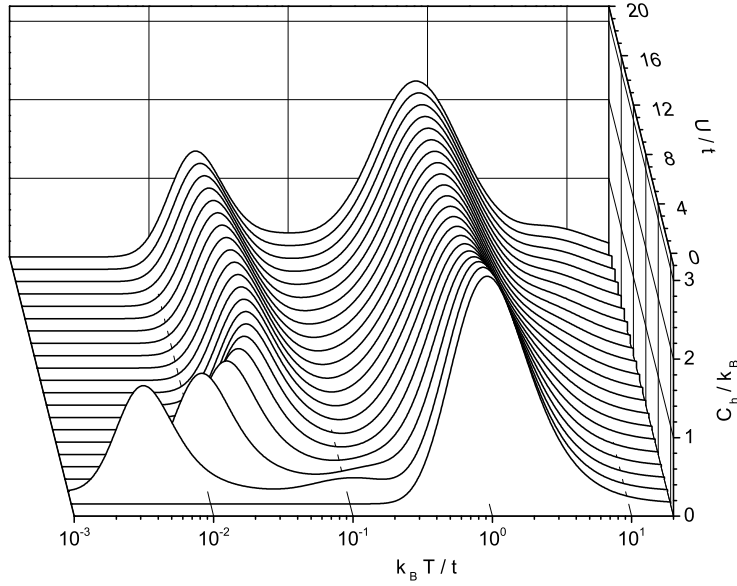


Fig. 3: The dependence of the system specific heat on the normalized temperature for various values of normalized Coulombic interactions energy.

remind that, in general, susceptibility exhibits a single peak, while specific heat develops two distinct maxima. Therefore, in the main panel of Fig. 5, only the position of low-temperature maximum of the specific heat is shown, while the inset presents the evolution of the position of high-temperature maximum. It can be noticed that the characteristic temperature of local maximum both for  $\chi_T$  and for  $C_h$  increases (starting from the zero value) until approximately  $U/t \simeq 9$ . If Coulombic interactions become stronger, the maxima shift back towards lower temperatures. The characteristic temperature at which the specific heat reaches maximum is at least twice lower than the corresponding temperature for magnetic susceptibility. The high-temperature maximum of specific heat shifts monotonically towards lower temperatures when  $U/t$  increases, however, this evolution is quite rapid for weaker  $U/t$  and then, for  $U/t \gtrsim 9$  (where point of inflection is reached) it becomes significantly slower.

In order to analyse the behaviour of the mentioned thermodynamic quantities in details, it can be useful to consider only the ground state and the first excited state. For the studied range of parameters ( $0 \leq U/t \leq 50$ ), the system of interest has a doubly degenerate ground state with total spin  $S = 0$ . The first excited state is separated in energy from the ground state by the energy gap equal to  $\Delta$  and has a degeneracy of nine, including three states with  $S = -1$ , three states with  $S = 0$  and three states with  $S = 1$ . The normalized gap value  $\Delta/t$  is plotted as a function

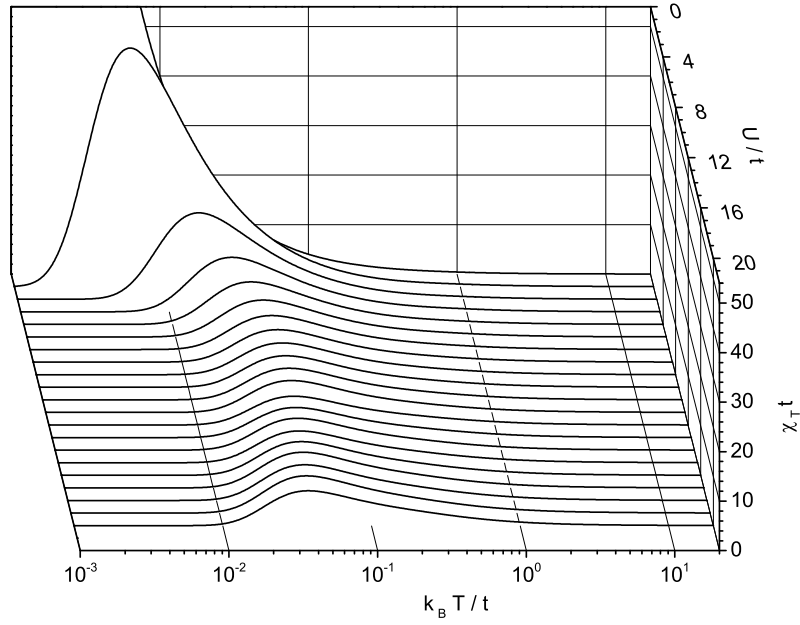


Fig. 4: The dependence of the system magnetic susceptibility on the normalized temperature for various values of normalized Coulombic interactions energy.

of the ratio  $U/t$  in Fig. 5 with dashed line (note the right vertical axis). It increases with increasing  $U/t$  reaching a maximum value at  $U/t \simeq 9.19$  and then a decrease is noticed. Such a knowledge about the energy spectrum allows us to analyse the behaviour of the selected thermodynamic quantities basing on a two-level system.

According to fluctuation-dissipation theorem, the specific heat under constant magnetic field, for the system with energy spectrum limited to the mentioned two states, can be expressed as:

$$(7) \quad C_h = k_B \beta^2 \frac{9\Delta^2 e^{-\beta\Delta}}{2 + 9e^{-\beta\Delta}} \left( 1 - \frac{9e^{-\beta\Delta}}{2 + 9e^{-\beta\Delta}} \right).$$

This function exhibits a Schottky anomaly in a form of a broad maximum at  $k_B T_{\max}/\Delta \simeq 0.3264$ .

Moreover, the magnetic susceptibility can be expressed under analogous assumptions as:

$$(8) \quad \chi_T = \frac{6\beta e^{-\beta\Delta}}{2 + 9e^{-\beta\Delta}},$$

with a Schottky maximum at somehow higher temperature, equal to  $k_B T_{\max}/\Delta \simeq 0.5656$ .

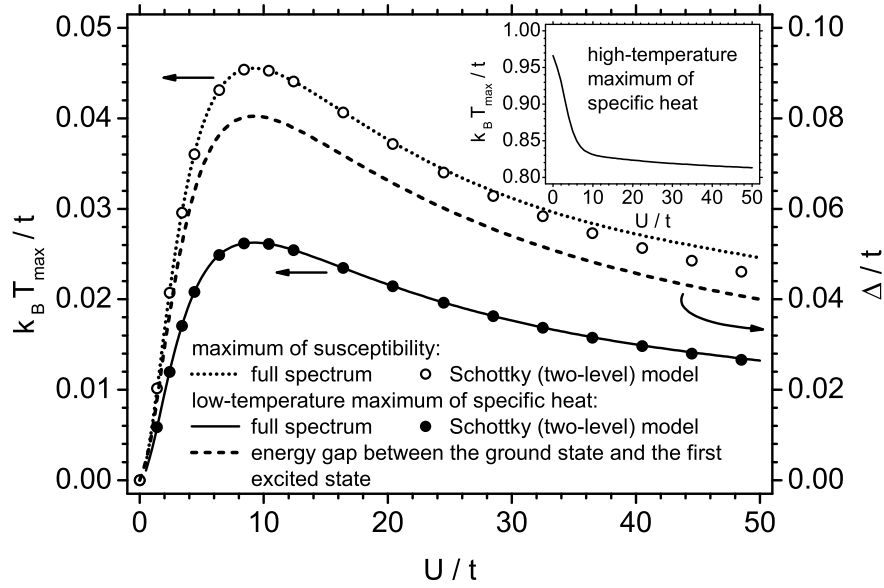


Fig. 5: The dependence of the energy gap as well as of characteristic temperatures at which magnetic susceptibility and specific heat reach local maxima on the normalized Coulombic interactions energy.

The values of magnetic susceptibility and specific heat predicted by the equations (7) and (8) based on the calculated energy gap  $\Delta$  are shown in Fig. 5 using empty and filled circles, respectively. It can be noticed, that for specific heat, a perfect agreement occurs between the results of full exact diagonalization calculations and the model involving only two states (ground state and the first excited state). Therefore, the origin of the low-temperature peak in specific heat can be explained in terms of a Schottky anomaly. In addition, the values for magnetic susceptibility also show a good agreement with the predictions of the two-level model, except at the highest studied values of  $U/t$ , i.e. for strongest Coulombic interactions. Therefore, it can be concluded that the magnetic susceptibility peak and the low-temperature peak in specific heat possess the character of Schottky anomalies and they share the variability trend with the energy gap  $\Delta$  as a function of  $U/t$ . Moreover, they can be accurately described with a model involving only two states lowest in energy and arise only in the presence of Coulombic interactions. On the other hand, the high-temperature maximum in specific heat is already present for a pure tight-binding model with  $U/t = 0$  and is unrelated to Coulombic interactions and only moderately sensitive to its occurrence.

The presented considerations show that the observed low-temperature maxima in magnetic susceptibility and specific heat are of Schottky anomaly origin, whereas



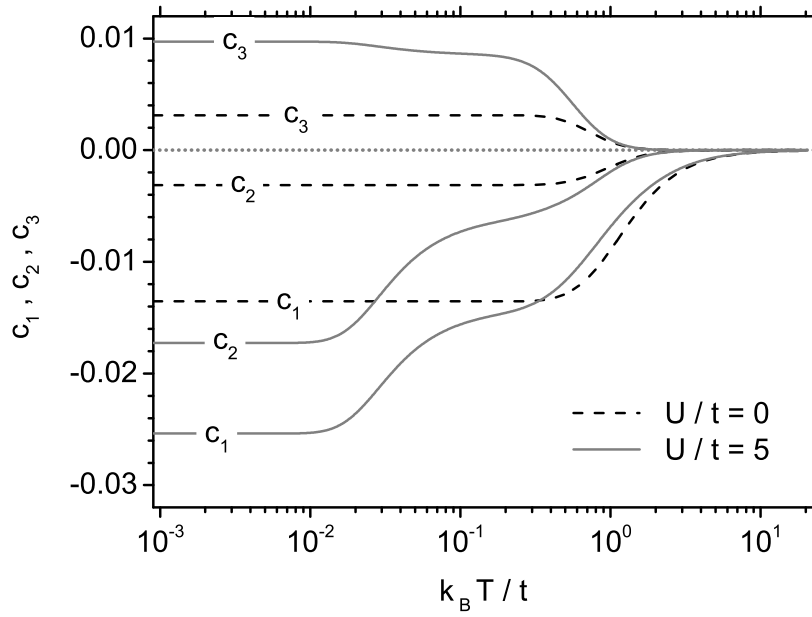


Fig. 6: The dependence of the spin-spin correlations for first, second and third neighbours (see Fig. 1) on the normalized temperature for two representative values of normalized Coulombic interactions energy.

the system of interest remains paramagnetic in the studied range of  $U/t$ . It can be noted that the similar plots in the Ref. [19] concerning specific heat for the case of 7 electrons show the effect of transition to the state with nonzero total spin over certain critical Coulombic interactions energy (which effect is absent in our case in the studied range).

In order to complete the characterization of the magnetic properties of the cubic cluster in the paramagnetic range, we illustrate the temperature dependence of the spin-spin correlations in Fig. 6. In this plot two cases are presented – the absence of Coulombic interactions ( $U/t = 0$ ) and the presence of them, for a moderate value of  $U/t = 5$ . As it can be noticed, the correlations between nearest-neighbour and second-neighbour spins are antiferromagnetic in character in both cases shown. On the contrary, the correlations between spins being third neighbours possess ferromagnetic character. In the absence of Coulombic interactions, the correlations exhibit almost flat temperature dependences unless the temperature is high, without any low-temperature features. Introducing the Coulombic interactions enhances very significantly the magnitude of correlations preserving their signs. Moreover, it leads to the appearance of low-temperature features, as the magnitude of correlations becomes more temperature dependent in some low-temperature range. This

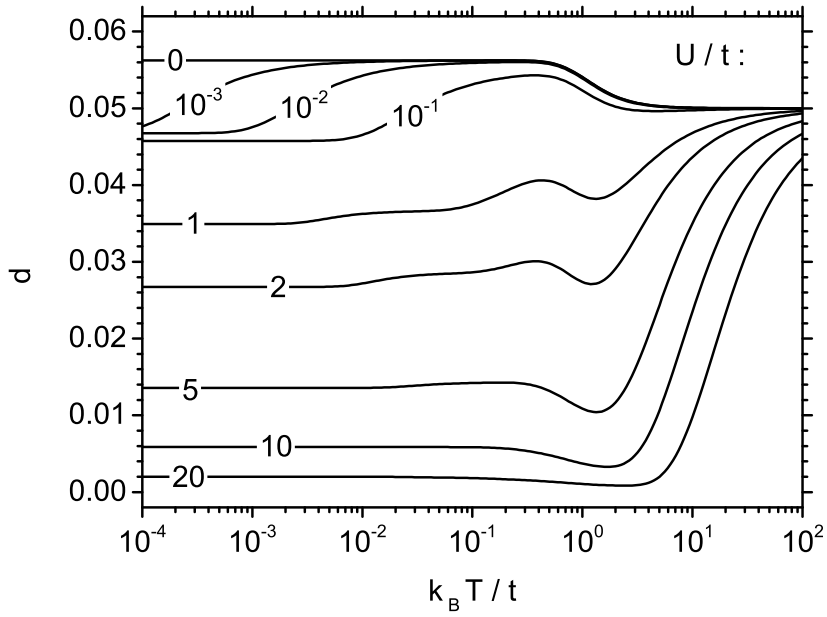


Fig. 7: The dependence of the average double occupancy per site on the normalized temperature for various values of normalized Coulombic interactions energy.

behaviour is much more pronounced for antiferromagnetic correlations, i.e. those between nearest-neighbours and second neighbours, whereas the ferromagnetic correlations between third neighbours remain less sensitive.

Last, but not least, we present the results of calculations of average double occupancy per site. The dependence of  $d$  on the temperature for various values of Coulombic interactions energy is shown in Fig. 7. It is remarkable that the low-temperature values of double occupancy strongly decrease when  $U/t$  increases. Such a tendency of lowering the double occupancy with the increase of the Coulombic (repulsive) interactions energy is also visible for example in the results of Ref. [22] for two-dimensional Hubbard model. On the contrary, at high temperature the double occupancy increases (and tends to a common limit of  $d = 0.05$  at  $T \rightarrow \infty$ ). Since the double occupancy of a site implies that a pair of electrons is in singlet state, with opposite spins, the increase in double occupancy is connected with a decrease in average squared magnetization per site (note that in the studied range the system is paramagnetic and the magnetizations themselves are equal to zero). Therefore, the temperature reduces the tendency to form magnetic moments (but increasing Coulombic interactions acts in an opposite direction). Ground-state value of double occupancy for  $U/t = 0$  is equal to  $d = 9/160 = 0.05625$ , but the limiting value for  $U/t \rightarrow 0$  is  $d \simeq 0.04575$ .

#### 4. Final remarks

In the paper we discussed the thermodynamic properties of a cubic cluster described by Hubbard model at quarter-filling. The exact numerical diagonalization enabled obtaining the artefact-free solution. The studied cluster indicated paramagnetic properties with no magnetization in the investigated range of Coulombic interaction energies. The double-peak structure of specific heat was found, with a low-temperature maximum well described by a Schottky anomaly model, involving only the ground state and the first excited state. The same model was applied to explain the origin of a single maximum in magnetic susceptibility. Also the behaviour of spin-spin correlations and double occupancy was analysed. The obtained exact numerical results may encourage further studies of clusters with other geometries and numbers of electrons; moreover, also the influence of other factors, such as external fields, can be worthy of investigation.

#### Acknowledgments

This work has been supported by Polish Ministry of Science and Higher Education on a special purpose grant to fund the research and development activities and tasks associated with them, serving the development of young scientists and doctoral students.

#### References

- [1] M. Žukovič and A. Bobák, *Phys. Lett. A* **378** (2014), 1773–1779.
- [2] J. Strečka and J. Čiřárová, *Acta Phys. Polon. A* **126** (2014), 26–27.
- [3] M. Žukovič, *J. Magn. Magn. Mater.* **374** (2015), 22–35.
- [4] J. Strečka, K. Karlová, and T. Madaras, *Physica B* **466–467** (2015), 76–85.
- [5] J. Hubbard, *Proc. Roy. Soc. A* **276** (1963), 238–257.
- [6] H. Tasaki, *J. Phys.: Condens. Matter* **10** (1998), 4353–4378.
- [7] J. Spałek, *Philosophical Magazine* **95** (2015), 661–681.
- [8] S. Szczeniowski and L. Wojtczak, *J. Phys. Colloques* **32** (1971), C1-1174–C1-1176.
- [9] A. Sukiennicki and L. Wojtczak, *Phys. Lett. A* **41** (1972), 37–38.
- [10] S. Szczeniowski, L. Wojtczak, and A. Sukiennicki, *J. Vac. Sci. Technol.* **10** (1973), 693–696.
- [11] A. Weiße and H. Fehske, *Exact Diagonalization Techniques*, in: *Computational Many-Particle Physics*, ed. H. Fehske, R. Schneider, and A. Weiße, *Lecture Notes in Physics* **739**, Springer Berlin-Heidelberg 2008, pp. 529–544.
- [12] J. Callaway, D. P. Chen, and Y. Zhang, *Z. Phys. D: Atom Mol. Cl.* **3** (1986), 91–96.
- [13] J. Callaway, D. P. Chen, and Y. Zhang, *Phys. Rev. B* **36** (1987), 2084–2091.
- [14] J. Callaway, *Physica B+C* **149** (1988), 17–21.
- [15] A. Parola, S. Sorella, S. Baroni, M. Parrinello, and E. Tosatti, *Int. J. Mod. Phys. B* **3** (1989), 1865–1873.

- [16] L. Tan, Q. Li, and J. Callaway, Phys. Rev. B **44** (1991), 341–350.
- [17] A. M. S. Macêdo and M. D. Coutinho-Filho, Revista Brasileira de Física **21** (1991), 121–135.
- [18] F. López-Urías and G. M. Pastor, Eur. Phys. J. D **52** (2009), 159–162.
- [19] D. Zwicker, *Gleichgewichtsthermodynamik des Hubbard-Modells für einen kubischen Cluster*, Diploma Thesis, Technische Universität Dresden (2009).
- [20] R. Schumann and D. Zwicker, Ann. der Phys. (Berlin) **522** (2010), 419–439.
- [21] Wolfram Research, Inc., Mathematica, Version 8.04, Champaign, IL (2010).
- [22] S. R. White, D. J. Scalapino, R. L. Sugar, E. Y. Loh, J. E. Gubernatis, and R. Scalettar, Phys. Rev. B **40** (1989), 506–516.

Department of Solid State Physics  
 Faculty of Physics and Applied Informatics  
 University of Łódź  
 Pomorska 149/153, 90-236 Łódź  
 Poland  
 e-mail: kszalowski@uni.lodz.pl  
 t\_balcerzak@uni.lodz.pl

Department of Theoretical Physics  
 and Astrophysics  
 Faculty of Science  
 P. J. Šáfárik University  
 Park Angelinum 9, 041 54 Košice  
 Slovak Republic

Presented by Ilona Zasada at the Session of the Mathematical-Physical Commission of the Łódź Society of Sciences and Arts on September 10, 2015

## BADANIA WŁAŚCIWOŚCI TERMODYNAMICZNYCH MODELU HUBBARDA DLA KLASTERA O KSZTAŁCIE SZEŚCIANU – DOKŁADNA DIAGONALIZACJA DLA WYPEŁNIENIA 1/4

### Streszczenie

Przedmiotem badań jest termodynamika zerowymiarowego klastera o kształcie sześcianu, opisywanego przez Hamiltonian Hubbarda, w tym zwłaszcza właściwości magnetyczne. Rozważany jest zakres, w którym badany klaster wykazuje paramagnetyzm. Wyniki otrzymano w ramach metody dokładnej diagonalizacji numerycznej. Przedyskutowano takie właściwości termodynamiczne, jak entropia, ciepło właściwe, podatność magnetyczna, korelacje spinowe i prawdopodobieństwo podwójnego obsadzenia węzła sieci. Szczególny nacisk położono na zbadanie położenia maksimów lokalnych ciepła właściwego i podatności, analizując je w ramach modelu Schottky’ego.

*Słowa kluczowe:* model Hubbarda, entropia, ciepło właściwe, podatność magnetyczna, paramagnetyzm, dokładna diagonalizacja, anomalia Schottky’ego

## B U L L E T I N

DE LA SOCIÉTÉ DES SCIENCES ET DES LETTRES DE ŁÓDŹ

2016

Vol. LXVI

Recherches sur les déformations

no. 1

pp. 29–35

*Contribution to the jubilee volume, dedicated  
to Professors J. Lawrynowicz and L. Wojtczak*

*Teresa Ramírez Rodríguez and Fray de Landa Castillo Alvarado*

**ANALYSIS OF THE KINETICS OF DECOMPOSITION  
OF CALCIUM CARBONATE FOR DESIGNING A HYDROGEN  
STORAGE MATERIAL**

**Summary**

This paper is a theoretical study based on the structure of  $\text{CaCO}_3$ , routed the challenge of developing a material capable of storing hydrogen. Therefore, a theoretical analysis of the kinetics of decomposition of calcium carbonate taking into account its physical-chemical properties is given. One of the reactions proposed in the decomposition produce calcium hydroxide and carbon dioxide in gaseous phase, these states have a material in solid state intended to hydrogen storage based on the calcium carbonate as a raw material.

*Keywords and phrases:* calcite, kinetic, decomposition mechanism, hydrogen

**1. Introduction**

Gasification of wet biomass accompanied by  $\text{CO}_2$  absorption is a potential method for hydrogen rich fuel gas production [1]. The drying of wet biomass generates a steam-rich atmosphere, in which the reforming of tar and hydrocarbon, the water gas shift reaction, and the  $\text{CO}_2$  absorbing by  $\text{CaO}$  take place [2, 3]. The presence of the sorbent greatly promotes both hydrogen production from biomass gasification and  $\text{CO}_2$  capture. In this process,  $\text{CaO}$  plays the dual role of catalyst and sorbent. It is noteworthy that the sorbent reveals a stronger effect on the water gas shift reaction than on the steam reforming of methane.

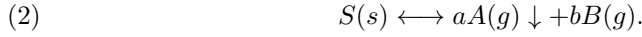
The objective of this research is study of calcium carbonate as a raw material for hydrogen storage. Calcite, a derivative of calcium carbonate is widely deposited as bio-mineral because of its high thermodynamic stability at room temperature [4]. it has a trigonal-rhombohedral crystal structure, ions comprising  $\text{Ca}^{+2}$  and planar groups  $\text{CO}_3^{-2}$ , which are in alternating layers oriented perpendicularly to the  $c$  axis. Each ion  $\text{Ca}^{+2}$  has six immediate  $\text{CO}_3^{-2}$  neighbors, oriented in such order that an oxygen atom is calcium immediate neighbor. Calcite belongs to the space group  $R\bar{3}2c$  whose crystal symmetry is trigonal  $\bar{3}2m$ . Ions  $\text{Ca}^{+2}$  and  $\text{CO}_3^{-2}$  in calcite are held together by ionic bonds. The dissociation of calcium carbonate is represented by the reaction [5, 6]:



Two modes of dissociative evaporation (equimolar and isobaric) were revealed and identified by B.V.L’Vov *et al.* [7], and Arrhenius parameters corresponding to ( $E$  and  $A$ ) were interpreted. That main concept in traditional approach is that the deviation from equilibrium is related with the existence of theoretically predicted energy barrier (activation energy) as a reaction. On the other hand, the main concept of the physical approach is that the decomposition of the primary reactive gas phase proceeds under equilibrium conditions, but the origin and composition of these commodities may differ from those in balance. For calcite, this difference involves decomposition of  $\text{CaCO}_3$  to  $\text{CO}_2$  molecules and gas molecules of low volatility of  $\text{CaO}$  which are subsequently condensed with the formation of solid  $\text{CaO}$ . The advantage of the physical approach on the chemical approach is to describe the decomposition process quantitatively using the laws of thermodynamics.

## 2. Theoretical analysis

The thermo-chemical approach in determining the activation energy of the dissociation reaction of calcium carbonate was introduced by L’Vov and is based on the assumption that an initial step involves evaporation of the reactant followed by the condensation of product of low volatile calcium oxide. Since primary thermo-chemical calculations show that in all cases forming solid product in the process of dissociative consistent vaporization of reactants, the equilibrium partial pressure of the main product is much higher than its saturation vapor pressure and therefore causes appearance of super-saturation vapor. Super-saturation is responsible for transferring the condensation energy reactant. Because this energy transfer directly affects the reactant changing the molar enthalpy of the dissociation reaction, if the theory is correct, the equilibrium temperature of the reaction is increasingly difficult to determine using standard thermal analysis because energy transfer condensation is extremely challenging to determine. To calculate the theoretical values of the parameter  $E$ , in the case of the solid compound  $S$  decomposed into gaseous products  $A$  and  $B$  with simultaneous condensation of low volatility of species  $A$  is given by:



The reaction parameter  $E$  (2) should be in different modes of decomposition gas, equimolar (in the absence of gaseous product  $B$  in the reactor atmosphere) and isobaric (in presence of excess of product  $B$ ). For equimolar mode and isobaric mode, equations (3) and (4), respectively apply:

$$(3) \quad E^e = \frac{\Delta_r H_T^0}{\nu} = \frac{\Delta_r H_T^0}{a+b},$$

$$(4) \quad E^i = \frac{(\Delta_r H_T^0)}{\nu-b} = \frac{\Delta_r H_T^0}{a},$$

where  $\nu$  is the total number of moles of gaseous products,  $(a+b)$ ,  ${}_r H_T^0$  its the enthalpy change in the reaction (2). In both cases, the parameter  $E$  corresponds to the specific enthalpy, i.e.: the enthalpy of the decomposition reaction reduced to one mole of primary products excluding component in excess. In calcite decomposition reaction is obtained:

$$(5) \quad \Delta_r H_T^0 = a\Delta_f H_T^0(\text{CaO}) + \Delta_f H_T^0(\text{CO}_2) - \Delta_f H_T^0(\text{CaCO}_3) + \tau\Delta_C H_T^0(\text{CaO}).$$

The term  $\tau\Delta_C H_T^0(A)$ , where the coefficient  $\tau$  corresponds to the fraction of energy transferred to condensation reactant. For the decomposition of calcite, temperatures equal to solid phases (product and reactant) can be expected by power equalization between the two phases; that is to say,  $\tau = 0.5$ .

The magnitudes of the thermodynamic functions (enthalpy and entropy) for the components of the decomposition reaction and the reaction for calcite as a whole at 800, 900 and 1000 K are indicated in Table 1.

Tab. 1: Thermodynamic functions.

Function	Temp. 800 K	Temp. 900 K	Temp. 1000 K
$\Delta_f H_T^0(\text{CaO})(g)$ [kJmol <sup>-1</sup> ]	407.7	74.4	78.1
$\Delta_f H_T^0(\text{CaO})(s)$ [kJmol <sup>-1</sup> ]	-600.3	-595.0	-589.7
$\Delta_f H_T^0(\text{CO}_2)(g)$ [kJmol <sup>-1</sup> ]	-361.0	-355.7	-350.4
$\Delta_f H_T^0(\text{CaCO}_3)(s)$ [kJmol <sup>-1</sup> ]	-1166.9	-1121.9	-1109.6
$\Delta_C H_T^0(\text{CaO})$ [kJmol <sup>-1</sup> ]	-671.0	-669.5	-667.9
$\Delta_r H_T^0$ [kJmol <sup>-1</sup> ]	<b>508.1</b>	<b>505.9</b>	<b>503.5</b>
$S_T^0(\text{CaO})(g)$ [Jmol <sup>-1</sup> K <sup>-1</sup> ]	254.0	258.4	262.3
$S_T^0(\text{CO}_2)(g)$ [Jmol <sup>-1</sup> K <sup>-1</sup> ]	257.4	263.5	269.2
$S_T^0(\text{CaCO}_3)(s)$ [Jmol <sup>-1</sup> K <sup>-1</sup> ]	193.2	207.3	220.2
$\Delta_r S_T^0$ [Jmol <sup>-1</sup> K <sup>-1</sup> ]	<b>318.2</b>	<b>314.6</b>	<b>313.3</b>

### 2.1. Thermal decomposition mechanism

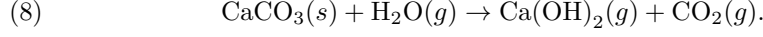
Condensation decomposition of calcium carbonate [8]:



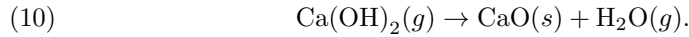
Dissociative evaporation decomposition of calcium carbonate is set to reaction (7):



and intermediate hydroxide formation:



The mechanism of decomposition reactions (7) and (8) corresponds to the first state in the two schemes of gasification mechanism. The subsequent steps of the process are described by the reactions (9) and (10):



The partial pressure of  $\text{CO}_2$  is expressed for each of reactions (6)–(8), through the reaction equilibrium constant  $K_p$  of corresponding:

$$(11) \quad P_{\text{CO}_2} = K_p(6),$$

$$(12) \quad P_{\text{CO}_2} = [K_p(7)]^{\frac{1}{2}},$$

$$(13) \quad P_{\text{CO}_2} = [K_p(8)xP_{\text{H}_2\text{O}}]^{\frac{1}{2}}.$$

### 2.2. Activation energies

From equation of the third law of thermodynamics:

$$(14) \quad K_p = \exp \frac{\Delta S_T^0}{R} = \exp \frac{-\Delta H_T^0}{RT},$$

where  $\Delta H_T^0$  and  $\Delta S_T^0$  are the changes in enthalpy and entropy in reactions (7) to (9), respectively, the ratio can be compared with the Arrhenius equation;

$$(15) \quad E_a = \Delta H_T^0$$

to equation (7); and

$$(16) \quad E_a = \frac{\Delta H_T^0}{2}$$

to equation (8). As  $P_{\text{H}_2\text{O}}$  is constant, then the equation (10) also applies to equation (16).

### 2.3. Kinetic analysis

Taking into account the physical-chemical properties of calcium carbonate:

$$\rho = 2710 \text{ kg m}^{-3}, \quad M = 0.100 \text{ kg mol}^{-1}, \quad \text{and} \quad \overline{M} = 0.050 \text{ kg mol}^{-1}$$

where  $\rho$  is the bulk density,  $M$  is the molar mass and  $\overline{M}$  is the geometric mean of the molar masses of all gaseous particles. The three kinetic parameters characterizing the



decomposition ( $P$ ,  $J$  and  $k$ ) are interrelated. The parameters  $P$  and  $J$  are calculated using equations (17)–(21). Where the flow of gaseous products  $J$ , is connected to the rate constant  $k$ . For spherical particles, the fraction decomposed featured by the trading volume model is described by equation (20), and according to the relationship

$$\alpha = 1 - \frac{m}{m_0}, \quad m = \left(\frac{4}{3}\right) r^3 \rho, \quad J = - \left(\frac{dm}{dt}\right) (4r^2)^{-1},$$

where  $m$ ,  $r$  and  $\rho$  are the mass, radius and density, respectively, of reactant spherical particle (s), the equation (20) and equation (21) are obtained:

$$(17) \quad J_A = \frac{MP_A}{(2\pi\overline{M}RT)^{\frac{1}{2}}},$$

$$(18) \quad \overline{M} = M_A^{\frac{a}{\nu}} x M_B^{\frac{b}{\nu}},$$

$$(19) \quad \nu = a + b,$$

$$(20) \quad \frac{d\alpha}{dt} = 3(1 - \alpha)^{\frac{2}{3}} k,$$

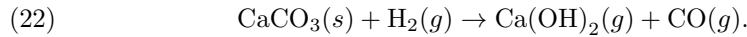
$$(21) \quad J = \rho r_0 k.$$

The thermodynamic functions used in the calculations are shown in Table 2.

Tab. 2: Thermodynamic functions used in the calculations [9].

Chemical compounds	State of aggregation	$\Delta_f H_{900}^0$ [kJmol <sup>-1</sup> ]	$S_{900}^0$ [Jmol <sup>-1</sup> K <sup>-1</sup> ]
CO <sub>2</sub>	gas	355.7 ± 0.1	263.5
CaO	gas	74.4 ± 15	258.4
CaO	solid	-595.0 ± 0.9	92.2
Ca(OH) <sub>2</sub>	gas	530.1 ± 20	392.1
CaCO <sub>3</sub>	solid	1121.9 ± 1.0	207.3

$P_{\text{CO}_2}$  values are determined by Eqs. (11)–(13) and the activation energies by Eqs. (15) and (16). For calculations of reaction (8), the water vapor partial pressure is assumed constant and equal to  $10^{-7}$  atm, taking into account that in the decomposition stage the total pressure in the system increased from  $10^{-8}$  atm to  $10^{-7}$  atm. Calculated kinetic parameters for the decomposition of calcium carbonate in accordance with reactions (6) to (8) are reported in Table 3. The effect of the partial pressure of hydrogen in the calcium carbonate given in reaction (22), under conditions  $P_{\text{H}_2} = 10^{-7}$  atm, is consistent with the results obtained in reaction (8):



The calculated kinetic parameters for the decomposition of calcium carbonate in accordance with reaction (22) are indicated in Table 4, with  $P_{\text{H}_2} = 10^{-7}$  atm [1] and  $P_{\text{H}_2} = 10^{-3}$  atm [2].

Tab. 3: Kinetic parameters for the decomposition of calcium carbonate in accordance with reactions (6)–(8).

Reaction	$\bar{T}$ [K]	$\Delta H_{900}^0$ [kJmol <sup>-1</sup> ]	$\Delta S_{900}^0$ [Jmol <sup>-1</sup> K <sup>-1</sup> ]	$E_a$ [kJmol <sup>-1</sup> ]	$P_{CO_2}$ [atm]
(6)	974	171.2	148.4	167	$4 \times 10^{-2}$
(7)	974	840.4	314.6	416	$5 \times 10^{-15}$
(8)	974	443.1	219.9	218	$2 \times 10^{-10}$

Tab. 4: Kinetic parameters for the decomposition of calcium carbonate.

$\bar{T}$ [K]	$\Delta H_{900}^0$ [kJmol <sup>-1</sup> ]	$\Delta S_{900}^0$ [Jmol <sup>-1</sup> K <sup>-1</sup> ]	$E_a$ [kJmol <sup>-1</sup> ]	$P_{CO_2}$ [atm] <sup>[1]</sup>	$P_{CO_2}$ [atm] <sup>[2]</sup>
974	479.0	252.9	228	$2 \times 10^{-10}$	$2 \times 10^{-8}$

### 3. Conclusions

In this paper there have been raised three decomposition processes according to the reactions (6) to (8). In equations (7) and (8) there are considered sources of water vapor, such as water contained in the samples of calcium carbonate, so there would be a dissociative evaporation and decomposition of an intermediate result of hydroxide formation. An increase in  $P_{H_2}$  up to  $10^{-3}$  atm results in a hundredfold increase in the decomposition rate. This growth does not induce a significant change in the rate of decomposition. As  $P_{CO}$  rise in proportion to an average of  $(P_{H_2})^{\frac{1}{2}}$  is compensated by an increase in flow diffusion limitation of CO in H<sub>2</sub>. As a hundred-fold increase in the decomposition rate corresponds to a reduction in the decomposition temperature of 150 to 160 K. Hence, the enhancement of the carbonate decomposition rate in a hydrogen atmosphere is further proof of the intermediate hydroxide formation mechanism. On the other hand, water and hydrogen act as a catalyst in the interaction with calcium carbonate. It is likely, that the decomposition temperature of calcium carbonate can have a reduction, which entails that the reaction proposed in the decomposition of calcium carbonate, wherein calcium hydroxide and carbon dioxide are obtained in the gaseous phase, gives indications how to obtain a material in solid state to hydrogen storage, and starting calcium carbonate as raw material.

### References

- [1] H. Guoxin and H. Hao, Biomass and Bionergy **33** (2009), 899–906.
- [2] V. Nikulshina, D. Hirsch, M. Mazzotti, and A. Steinfeld, Energy **31** (2006), 1379–1389.
- [3] A. Escardino, J. Garca-Ten, C. Feliu, A. Saburit, and V. Cantavella, Journal of Industrial and Engineering Chemistry **19** (2013), 886–897.
- [4] A. J. Skinner, J. P. LaFemina, American Mineralogist **79** (1994), 205–214.

- [5] D. T. Beruto, A. W. Searcy, M. G. Kim, *Thermochimica Acta* **424** (2004), 99–109.
- [6] B. V. Lvov, *Thermochimica Acta* **386** (2002), 1–16.
- [7] B. V. Lvov, *Spectrochimica Acta Part B* **66** (2011), 557–564.
- [8] A. Escardino, J. Garcia-Ten, and C. Feliu. *Journal of the European Ceramic Society* **28** (2008), 3011–3020.
- [9] B. V. Lvov and V. L. Ugolkov, *Thermochimica Acta* **410** (2004), 47–55.

Instituto Politécnico Nacional  
Unidad Prof. ALM  
Mexico, D.F., 07738  
Mexico  
e-mail: fray@esfm.ipn.mx

Presented by Ilona Zasada at the Session of the Mathematical-Physical Commission of the Łódź Society of Sciences and Arts on November 30, 2015

## **ANALIZA KINETYKI ROZKŁADU WĘGLANU WAPNIA DLA UTWORZENIA SUBSTANCJI ZATRZYMUJĄCEJ WODÓR**

### **S t r e s z c z e n i e**

Praca jest teoretycznym studium bazującym na  $\text{CaCO}_3$ , prowadzącym do wyzwania by zbadać substancję odpowiedzialną za związanie wodoru. W związku z tym podana jest teoretyczna analiza kinetyki rozkładu węglanu wapnia, uwzględniająca jego własności fizyczno-chemiczne. Jedną z zaproponowanych reakcji rozkładu jest powstawanie wodorotlenku wapnia i dwutlenku węgla w fazie gazowej, które to stany mają w substancji ciała stałego zamierzone związanie wodoru w oparciu o węglan wapnia jako surowiec.

*Słowa kluczowe:* kalcyt, kinetyczny, mechanizm rozkładu, wodór



## B U L L E T I N

DE LA SOCIÉTÉ DES SCIENCES ET DES LETTRES DE ŁÓDŹ

2016

Vol. LXVI

Recherches sur les déformations

no. 1

pp. 37–42

*Contribution to the jubilee volume, dedicated  
to Professors J. Lawrynowicz and L. Wojtczak*

Yuri B. Zelinskii

## THE PROBLEM OF THE SHADOWS

**Summary**

We consider the review of results on building generalized convex hull for family consisting of convex sets in Euclidean space. The solution of similar problems in (hyper)complex Euclidean space is obtained. The unsolved questions related to those problems are discussed.

*Keywords and phrases:* sphere, ball, convex set, (hyper)complex line,  $n$ -dimensional (hyper)complex Euclidean space

**1. Introduction**

We consider solution of the shadows problem and some adjacent questions.

*Definition 1.* We say that a set  $E \subset \mathbb{R}^n$  in Euclidean space is  $m$ -convex with respect to the point  $x \in \mathbb{R}^n \setminus E$ , if it exists a  $m$ -dimensional plane  $L$  such that  $x \in L$  and  $L \cap E = \emptyset$ .

*Definition 2.* We say that the set  $E \subset \mathbb{R}^n$  is  $m$ -convex if it is  $m$ -convex with respect to each point  $x \in \mathbb{R}^n \setminus E$ .

Both definitions satisfy the axiom of convexity: the intersection of any non-empty subfamily of these sets satisfies the definition also. For every set  $E \subset \mathbb{R}^n$  we can consider the minimal  $m$ -convex set containing  $E$  and call it  $m$ -hull of the set  $E$ .

As a special case of 1-hull of a set of balls we present the following problem of shadows posed by G. Hudayberganov [1–3].

**The problem of a shade.** What is the minimum number of disjoint closed balls with centres on the given sphere whose radii are smaller than the radius of the sphere under the condition, that any line passing through the centre of the sphere intersects at least one of these balls?

In other words, this problem can be reformulated in the following way. How many closed balls of radii which are smaller than the radius of the given sphere and with centres on the sphere will provide that the centre of the sphere belongs to the 1-hull of family of these balls?

## 2. Real case

We are considering results for convex sets in the real Euclidean space which have been obtained in our recent papers.

**Theorem 1.** [4] *There exist two closed (open) balls with centres on the unit circle and radii smaller than one, which provide that the centre of the circle belongs to the 1-hull of these balls.*

**Theorem 2.** [4] *In order that the centre of the fixed  $(n - 1)$ -sphere in the  $n$ -dimensional Euclidean space,  $n > 2$ , belongs to the 1-hull of a family of open (closed) balls with radii and that no more than (less than) the radius of the sphere, with centres on that sphere, it is necessary and sufficient to take  $(n + 1)$  balls.*

Now we shall consider the change of the statement if the centres of the balls do not belong to the sphere, or the family of sets in question differs from balls.

**Theorem 3.** [5] *For a point in the  $n$ -dimensional Euclidean space,  $n \geq 2$ , belonging to the 1-hull of family of disjoint open (closed) balls, which do not contain the given point, it is necessary and sufficient to take  $n$  balls.*

**Theorem 4.** [5] *For a point in the  $n$ -dimensional Euclidean space,  $n \geq 2$ , belonging to the 1-hull of family of disjoint closed sets, obtained from the given convex set with non-empty interior with the help of a group of transformations consisting of homotheties and motions, it is necessary and sufficient  $n$  elements of such family.*

Let consider more general objects according to the previous definitions.

**Definition 3.** We say that the set  $E \subset \mathbb{R}^n$  is  $m$ -semiconvex with respect to the point  $x \in \mathbb{R}^n \setminus E$  if it exists a  $m$ -dimensional half-plane  $P$  such that  $x \in P$  and  $P \cap E = \emptyset$ .

**Definition 4.** We say that the set  $E \subset \mathbb{R}^n$  is  $m$ -semiconvex if it is  $m$ -semiconvex with respect to each point  $x \in \mathbb{R}^n \setminus E$ .

It is easy to verify that these definitions satisfy the axiom of convexity, and we also can build the  $m$ -semiconvex hull of a set according to these definitions.

Now we consider an analogue of the problem of shadow for semiconvex case. What is the minimum number of disjoint closed (open) balls with centres on the sphere and whose radii are smaller (no more) than the radius of the given sphere, sufficient that any ray with the centre of the sphere intersects at least one of these balls? In [4, 5] we have got the partial answer to this question.

**Theorem 5.** [4] *For the centre of the two-dimensional sphere in three-dimensional Euclidean space belonging to the 1-semiconvex hull of family of open (closed) balls with radii not exceeding (smaller) than the radius of the sphere and with the centre on this sphere it is enough to take ten balls of this family.*

**Theorem 6.** *For a point in  $n$ -dimensional Euclidean space belonging to the 1-semiconvex hull of a family of disjoint closed sets, obtained from the given convex set having a non-empty interior with the help of the transformation group consisting of movements and homotheties, it is necessary and sufficient  $n + 1$  elements of the family.*

*Remark 1.* If we exclude rotations from the group of the motion, it follows that the number of necessary elements is increasing. For instance, if a convex body is a square-wave parallelepiped in  $\mathbb{R}^n$ , than the number of necessary elements of a set for building a 1-semiconvex hull will go up to  $2n$ .

### 3. (Hyper)complex case

We shall study how to change the situation with the previous problem if we replace the real Euclidean space by a (hyper)complex Euclidean space  $\mathbb{C}^n(\mathbb{H}^n)$ .

*Definition 5.* We say that the set of  $E \subset \mathbb{C}^n(\mathbb{H}^n)$  is  $m$ -(hyper)complex convex with respect to the point  $z \in \mathbb{C}^n \setminus E$  ( $\mathbb{H}^n \setminus E$ ) if there is a  $m$ -dimensional (hyper)complex plane  $L$  such that  $z \in L$  and  $L \cap E = \emptyset$ . We say that a set  $E \subset \mathbb{C}^n(\mathbb{H}^n)$  is  $m$ -(hyper)complex if it is  $m$ -(hyper)complex with respect to each point  $z \in \mathbb{C}^n(\mathbb{H}^n)$ .

**The problem of shade.** What is the minimum number of disjoint closed balls with centres on the sphere  $S^{2n-1} \subset \mathbb{C}^n$  ( $S^{4n-1} \subset \mathbb{H}^n$ ) and a radii which are smaller than the radius of the given sphere, sufficient that any (hyper)complex line passing through the centre of the sphere intersects at least one of these balls?

Similarly to the real case for an arbitrary set we consider the least  $m$ -(hyper)-complex set containing  $E$  and call it a  $m$ -(hyper)complex hull of  $E$ .

**Theorem 7.** *For a point in two-dimensional (hyper)complex Euclidean space belonging to the 1-(hyper)complex hull of a family of disjoint open (closed) balls that do not contain the given point it is necessary and sufficient two balls of this family with centres on the sphere centred at the origin.*

*Proof.* We give a proof for the complex space  $\mathbb{C}^n$ . In hypercomplex case  $\mathbb{H}^n$  the proof is similar. Let  $z = (z_1, z_2) \in \mathbb{C}^2$  be an arbitrary point in the space. Select one open ball  $B_1$  with radius equal to one. Put its centre at the point  $(1, 0) \in \mathbb{C}^2$ . The tangent real three-dimensional plane at the origin of this ball is given by equation  $\operatorname{Re} z_1 = 0$ . The line  $z_1 = 0$  is the unique complex line lying in this plane and passing through the origin. Therefore it is sufficient to select the second ball  $B_2$  (its radius can be as small as desired) so that it has a point of intersection with the line. In particular, it is possible to select its centre at the point  $(0, 1)$ . This proves our statement for open balls. Slightly reducing the radii of these balls, and using a continuous change of the tangent planes to the ball, we get the theorem in the case of closed balls.  $\square$

The following result (see [5]) gives an answer to the question 1.

**Theorem 8.** *For a point in the  $n$ -dimensional (hyper)complex Euclidean space  $\mathbb{C}^n(\mathbb{H}^n)$  belonging to the 1-(hyper)complex hull of a family of disjoint open (closed) balls that do not contain the given point, it is necessary and sufficient  $n$  balls of this family.*

*Proof.* Now we use the structure of the previous theorem. We define a system of balls in the three-dimensional complex space  $\mathbb{C}^3$ . We assume that the space  $\mathbb{C}^2$  is embedded in the space  $\mathbb{C}^3$  as the hyperplane  $L = (z_1, z_2, 0)$  built in its balls  $B_1$  and  $B_2$ . First we prolong these two dimensional balls up to the balls in  $\mathbb{C}^3$ , keeping the original centres of balls and their designations. Now, increase the ball  $B_2$  to the ball of radius  $1 - \sqrt{2}$ , which now touches the ball  $B_1$ . We reduce the ball  $B_1$  preserving its centre  $(1, 0, 0)$ , but so that in the complex hyperplane  $L$  it was impossible to carry out a complex line through the origin which does not meet any one of the selected two balls. By the property of continuity, each complex line that is close to any line from the plane  $L$ , intersects one of these balls as well. Now it is enough to select the ball  $B_3$  centred on the axis  $(0, 0, z_3)$  sufficiently close to the origin, but with radius less than the distance from its centre to the origin so that each complex line through the origin crosses one of the chosen three balls. Repeating analogously the transition from space  $\mathbb{C}^{n-1}$  to space  $\mathbb{C}^n$ , we obtain the proof of the theorem. In hypercomplex case the proof is similar.  $\square$

*Remark 2.* The arguments similar to those given in [5] and based on [6, 7] allow us to show that Theorem 8 remains valid if the balls are replaced by convex sets with non-empty interior, obtained from one set with action of transformation group.

## 4. Open problems

Unfortunately, Theorems 5 and 6 give no answer about the minimal number of balls which are sufficient for the centre on the sphere to be in 1-semiconvex hull. There remain open questions on constructing of the (hyper)complex hulls as well.



*Question 1.* What is the minimum number of closed (open) balls in the  $n$ -dimensional real Euclidean space with centres on the sphere and radii which are smaller (no more) than the radius of the sphere for  $n \geq 3$ , allowing to the origin of the sphere to be in their 1-semiconvex hull? Is this number finite for  $n > 3$ ?

*Question 2.* What is the minimum number of closed (open) balls in the  $n$ -dimensional (hyper)complex Euclidean space with centres on the sphere and the radii which are smaller (no more) than the radius of the sphere for  $n \geq 3$ , allowing the origin of the sphere to belong to their 1-(hyper)complex hull?

*Question 3.* To define a (hyper)complex semiconvex hull and give an estimation for a family of sets with a property of belonging the point to its generalized hull.

### Acknowledgment

The author acknowledges the Polish-Ukrainian grant no.39/2014 *Topological-analytical methods in complex and hypercomplex analysis* of the Polish Academy of Sciences and National Academy of Sciences of Ukraine.

### References

- [1] Yu. B. Zelinskii, *Multivalued mappings in the analysis*, Naukova Dumka, Kyiv 1993, 264 pp. (in Russian).
- [2] Yu. B. Zelinskii, *Convexity*, Selected chapters, Institute of Mathematics NAS of Ukraine, Kyiv 2012, 92, 280 pp. (in Russian).
- [3] G. Khudaiberganov, *On uniformly polynomially convex hull of the union of balls*, Manuscript Dep. in VINITI 21.02.1982, no 1772 - 85 Dep. (in Russian).
- [4] Yu. B. Zelinskii, I. Yu. Vygovska, and M. V. Stefanchuk, *Generalized convex sets and shadows problem*, arXiv preprint / arXiv:1501.06747 [math.MG] / (2015), 15 p. (in Russian).
- [5] Yu. B. Zelinskii, *The problem of the shadows for a family of sets*, Proc. Inst. Math. NAS Ukraine 12, Kyiv 2015 - to appear (in Russian).
- [6] R. D. Anderson and V. L. Klee, *Convex functions and upper-semi-continuous collections*, Duke Math. J. **19** (1952), 349–357.
- [7] K. Leichtweiss, *Konvexe Mengen*, Springer-Verlag, Berlin-New York 1980.

Institute of Mathematics  
National Academy of Sciences of Ukraine  
Tereshchenkivska str. 3, UA-01601 Kyiv  
Ukraine  
e-mail: zel@imath.kiev.ua

Presented by Julian Ławrynowicz at the Session of the Mathematical-Physical Commission of the Łódź Society of Sciences and Arts on November 30, 2015

**PROBLEM CIENI****S t r e s z c z e n i e**

Dokonujemy przeglądu wyników o konstrukcji uogólnionej otoczki wypukłej złożonej ze zbiorów wypukłych w przestrzeni euklidesowej. Rozwiązanie analogicznych zagadnień jest obecnie uzyskane dla (hiper)zespolonej przestrzeni euklidesowej. Omawiamy też nierozwiązane problemy związane z tymi zagadnieniami.

*Słowa kluczowe:* sfera, kula, zbiór wypukły, linia (hiper)zespolona,  $n$ -wymiarowa (hiper)zespolona przestrzeń

## B U L L E T I N

DE LA SOCIÉTÉ DES SCIENCES ET DES LETTRES DE ŁÓDŹ

2016

Vol. LXVI

Recherches sur les déformations

no. 1

pp. 43–75

*Contribution to the jubilee volume, dedicated  
to Professors J. Ławrynowicz and L. Wojtczak*

*Kehelwala Dewag Gayan Maduranga and Rafał Ablamowicz*

## REPRESENTATIONS AND CHARACTERS OF SALINGAROS' vee GROUPS OF LOW ORDER

### Summary

We study irreducible representations and characters of Salingaros' vee groups of orders 4, 8, and 16 as 2-groups of exponent 4. In particular, we construct complex irreducible group modules and explicit representations of these groups. We prove a theorem regarding the number of conjugacy classes and the number of inequivalent irreducible representations of degree one and two. We show how to decompose a complex group algebra into irreducible submodules in accordance with Maschke's Theorem. We formulate two algorithms for finding bases for these submodules which rely on the Groebner basis methods. In the end, we provide the character tables of these groups.

*Keywords and phrases:* Clifford algebra, center, character table, conjugacy classes, derived subgroup, group representation, Groebner basis, Maschke's Theorem, 2-group

### 1. Introduction

In a series of papers, Salingaros [18–20] studied a connection between finite groups and Clifford algebras [14]. He described five types of finite groups that are related to real Clifford algebras  $Cl_{p,q}$  and spinors. He called these groups 'vee groups' and the five classes he labelled as  $N_{\text{odd}}$ ,  $N_{\text{even}}$ ,  $\Omega_{\text{odd}}$ ,  $\Omega_{\text{even}}$ , and  $S_k$ . In 1988 Shaw [21] studied a group of order 128 which he associated with the Clifford algebra  $Cl_{0,7}$ , while O'Brien and Slattery [15] investigated the structure of finite groups associated with Clifford algebras of signature  $(0, d)$ ,  $d \equiv 3 \pmod{4}$ . Later, Albuquerque and

Majid [5] viewed Clifford algebras as group algebras of  $\mathbb{Z}_2^n$  twisted by a cocycle. They obtained periodicity properties of the Clifford algebras and presented a new approach to their spinor representations through the twisted group algebra. Matrix representations of generalized Clifford algebras viewed as twisted group rings  $\mathbb{Z}_2^n$  were also studied by Caenepeel and Van Oystaeyen [7]. More recently, the ‘vee groups’ appeared in [2–4] where (while denoted as  $G_{p,q}$ ) their transitive action on complete sets of mutually annihilating primitive idempotents was studied. Using the normal stabilizer subgroup  $G_{p,q}(f)$  of a primitive idempotent  $f$ , left transversals, spinor bases, and maps between spinor spaces for different orthogonal idempotents  $f_i$  summing up to 1 were described while the finite stabilizer groups according to the signature in simple and semisimple cases were classified. Most recently, Salingaros’ ‘vee groups’ have appeared in Varlamov [22] in his study of *CPT* groups for spinor fields in de Sitter and anti-de Sitter spaces.

In this paper we apply methods of representation theory of finite groups and their characters [12, 16, 17] to construct irreducible representations of Salingaros’ ‘vee groups’ of orders 4, 8, and 16. As a byproduct we obtain their character tables. Throughout,  $G$  always denotes a finite group and any action of  $G$  on a  $G$ -module is a left action.

To establish notation and the background for later computations, we recall basic results of the theory of representations and characters of finite groups [12].

**Theorem 1. (Maschke)** *Let  $G$  be a finite group and let  $V$  be a nonzero  $G$ -module. Then  $V = W^{(1)} \oplus W^{(2)} \oplus \dots \oplus W^{(k)}$ , where each  $W^{(i)}$  is an irreducible  $G$ -submodule of  $V$ .*

As a result of Maschke’s theorem, matrices of any representation can be written in the block-diagonal form once a suitable basis in the representation module is chosen. Thus, a representation is irreducible or it is *completely reducible* meaning that it can be written as a direct sum of irreducible representations.

**Corollary 1.** *Let  $G$  be a finite group and let  $X$  be a matrix representation of  $G$  of dimension  $d > 0$ . Then there is a fixed matrix  $T$  such that every matrix  $X(g)$ ,  $g \in G$ , has the diagonal form*

$$(1) \quad TX(g)T^{-1} = \text{diag} \left( X^{(1)}(g), X^{(2)}(g), \dots, X^{(k)}(g) \right).$$

Given a reducible representation, it is interesting to derive a procedure to find a basis in the module to completely reduce it per Maschke’s Theorem. Since later we will work exclusively with group algebras, we recall the following result.

Let  $V$  be a complex vector space with an inner product  $\langle \cdot, \cdot \rangle$  and let  $W^\perp$  denote the orthogonal complement of a subspace  $W$  of  $V$ . It is always true that  $V = W \oplus W^\perp$  and that this decomposition is  $G$ -invariant as long as the inner product is  $G$ -invariant, that is,  $\langle g\mathbf{u}, g\mathbf{v} \rangle = \langle \mathbf{u}, \mathbf{v} \rangle$  for any  $g \in G$  and  $\mathbf{u}, \mathbf{v} \in V$ . This leads to the following known result [17].

**Proposition 1.** *Let  $V$  be a  $G$ -module,  $W$  a submodule, and  $\langle \cdot, \cdot \rangle$  an inner product invariant under the action of  $G$ . Then  $W^\perp$  is also a  $G$ -submodule.*

Using the  $G$ -invariance of the orthogonal complement allows one to find a decomposition of any representation module into irreducibles. Following [3, 4], we denote Salingaros' 'vee group' related to the universal Clifford algebra  $\mathcal{Cl}_{p,q}$  as  $G_{p,q}$ . Let  $\mathcal{Cl}_{p,q}$  be a real universal Clifford algebra with Grassmann basis  $\mathcal{B}$  sorted by the admissible order **InvLex** [2]. We begin by recalling an informal definition of Salingaros' vee group [20].

**Definition 1.** *A vee group  $G_{p,q}$  is defined as the set  $G_{p,q} = \{\pm m \mid m \in \mathcal{B}\}$  in  $\mathcal{Cl}_{p,q}$  together with the Clifford product as the group binary operation.*

This finite group is of order  $|G_{p,q}| = 2^{1+p+q}$  and its commutator subgroup  $G'_{p,q} = \{\pm 1\}$ . The following result is well known [12, 17].

**Theorem 2.** *Let  $G$  be a finite group. The number of degree 1 representations of  $G$  is  $[G : G']$  where  $G'$  is the commutator subgroup of  $G$ .*

**Example 1.** *Let  $G_{p,q}$  be the Salingaros' vee group of the Clifford algebra  $\mathcal{Cl}_{p,q}$  [18–20]. The commutator subgroup  $G'_{p,q}$  is  $\{1\}$  when  $p + q = 1$  and it is  $\{1, -1\}$  when  $p + q \geq 2$ . Thus,  $G_{p,q}/G'_{p,q} \cong (\mathbb{Z}_2)^n$  where  $n = p + q \geq 2$ . In the special case  $n = p + q = 1$  and the signature  $(1, 0)$ , the group  $G_{1,0}/G'_{1,0} \cong G_{1,0} \cong \mathbb{Z}_2 \times \mathbb{Z}_2$ , whereas in the signature  $(0, 1)$ , the group  $G_{0,1}/G'_{0,1} \cong G_{0,1} \cong \mathbb{Z}_4$ .*

For the remainder of the current section, we recall basic results from the theory of representations and characters that will be needed in the later sections.

Let  $x, y \in G$ . Then,  $x$  is *conjugate* to  $y$  in  $G$  if  $y = g^{-1}xg$  for some  $g \in G$ . The set of all elements conjugate to  $x \in G$  is called the *conjugacy class* of  $x$  in  $G$  and it is denoted by  $x^G$ . Thus,  $x^G = \{g^{-1}xg : g \in G\}$ . Recall that conjugacy is an equivalence relation, and that the conjugacy classes are the equivalence classes. Thus, every group can be represented as a disjoint union (a partition) of conjugacy classes.

The size of each class is the index of the centralizer of any representative of the conjugacy class in  $G$ . The *centralizer* of  $x \in G$ , written  $C_G(x)$ , is the set of elements of  $G$  which commute with  $x$ , i.e.,  $C_G(x) = \{g \in G : xg = gx\}$ .

**Theorem 3.** *Let  $x \in G$ . Then the size of the conjugacy class  $x^G$  is given by*

$$(2) \quad |x^G| = [G : C_G(x)] = |G|/|C_G(x)|.$$

*In particular, the number of elements of a conjugacy class is a divisor of the order of the group.*

A proof of the theorem is straightforward [12]. To illustrate the theorem, we recall the conjugacy classes of the dihedral group  $D_{2n}$  [12].

**Example 2.** Consider the dihedral group

$$D_{2n} = \langle r, p : r^n = p^2 = (rp)^2 = e \rangle$$

of order  $2n$ . When  $n$  is odd,  $D_{2n}$  has  $\frac{1}{2}(n+3)$  conjugacy classes. Namely,

$$(3) \quad \{e\}, \{r, r^{-1}\}, \dots, \{r^{(n-1)/2}, r^{-(n-1)/2}\}, \{p, rp, \dots, r^{n-1}p\}.$$

When  $n$  is even and  $n = 2m$  for some positive integer  $m$  then  $D_{2n}$  has  $m+3$  conjugacy classes:

$$(4) \quad \{e\}, \{r^m\}, \{r, r^{-1}\}, \dots, \{r^{m-1}, r^{-(m-1)}\}, \\ \{r^{2j}p : 0 \leq j \leq m-1\}, \{r^{2j+1}p : 0 \leq j \leq m-1\}.$$

An important relation between characters, conjugacy classes, and equivalent representations is the following standard result [12, 17].

**Proposition 2.** Let  $X$  be a matrix representation of a group  $G$  of degree  $d$  with character  $\chi$ .

- (i)  $\chi(1) = d$ .
- (ii) If  $g, h$  belong to a conjugacy class  $K$  in  $G$ , then  $\chi(g) = \chi(h)$ .
- (iii) If  $Y$  is a representation of  $G$  with character  $\psi$ , and if  $X \cong Y$  then  $\chi(g) = \psi(g)$  for all  $g \in G$ .

A proof of this proposition can be easily given, see [17].

Let  $X(g)$ ,  $g \in G$ , be a matrix representation, that is, a homomorphism  $G \rightarrow \text{GL}(n, \mathbb{C})$  (in this paper we always consider representations over the complex field). Then the character  $\chi$  of  $X$  is the map  $G \xrightarrow{\text{tr } X} \mathbb{C}$  such that  $\chi(g) = \text{tr } X(g)$  where  $\text{tr}$  denotes the trace of a matrix. If  $V$  is a  $G$ -module, then its character is the character of a matrix representation  $X$  on  $V$ .

Consider a character  $\chi$  of a group  $G$  as a row vector with complex entries

$$(5) \quad \chi = (\chi(g_1), \chi(g_2), \dots, \chi(g_n)),$$

where  $G = \{g_1, g_2, \dots, g_n\}$ . Inner product of characters can be defined as follows.

**Definition 2.** Let  $\chi$  and  $\psi$  be two characters of a group  $G$ . The inner product of  $\chi$  and  $\psi$  is defined as the following sum over  $G$ :

$$(6) \quad \langle \chi, \psi \rangle = \frac{1}{|G|} \sum_{g \in G} \chi(g) \overline{\psi(g)}.$$

Based on the above definition, it may be impossible to find the inner product for an arbitrary field because it may lack the conjugation operation. So, the following proposition gives an equivalent form of the inner product which can be used for any field. Also, since all elements in the same conjugacy class have the same character, the formula for the inner product can be further simplified.

**Proposition 3.** Let  $G$  have  $k$  conjugacy classes with representatives  $g_1, g_2, \dots, g_k$ . Also, let  $\chi$  and  $\psi$  be some characters of  $G$ . Then,  $\langle \chi, \psi \rangle = \langle \psi, \chi \rangle$ , and

$$(7) \quad \langle \chi, \psi \rangle = \frac{1}{|G|} \sum_{g \in G} \chi(g) \psi(g^{-1}) = \sum_{i=1}^k \frac{\chi(g_i) \overline{\psi(g_i)}}{|C_G(g_i)|}.$$

**Theorem 4.** Let  $\chi$  and  $\phi$  be irreducible characters of a group  $G$ . The characters are orthonormal with respect to the inner product, i.e.,  $\langle \chi, \psi \rangle = \delta_{\chi, \psi}$ .

As a consequence of the above theorem, several results can be stated in relation to representations, irreducibility, etc. The following theorem will be used extensively in finding irreducible characters of certain groups in Section 2.

**Theorem 5.** Let  $X$  be a representation of  $G$  with character  $\chi$ , and

$$X \cong m_1 X^{(1)} \oplus m_2 X^{(2)} \oplus \dots \oplus m_k X^{(k)},$$

where the  $X^{(i)}$  are pairwise inequivalent irreducibles with characters  $\chi^{(i)}$  and multiplicities  $m_i$ .

1.  $\chi = m_1 \chi^{(1)} \oplus m_2 \chi^{(2)} \oplus \dots \oplus m_k \chi^{(k)}$ .
2.  $\langle \chi, \chi^{(i)} \rangle = m_i$  for all  $i$ .
3.  $\langle \chi, \chi \rangle = m_1^2 + m_2^2 + \dots + m_k^2$ .
4.  $\chi$  is irreducible if and only if  $\langle \chi, \chi \rangle = 1$ .
5. Let  $Y$  be another representation of  $G$  with character  $\psi$ . Then  $X \cong Y$  if and only if  $\chi(g) = \psi(g)$  for all  $g \in G$ .

Observe that pairwise inequivalent irreducible  $G$ -modules give pairwise inequivalent irreducible representations. Then, Maschke's theorem implies that the group algebra  $\mathbb{C}[G]$  can be written as  $\mathbb{C}[G] = \oplus_i m_i V^{(i)}$  where  $m_i$  is the multiplicity of  $V^{(i)}$  stating how many times  $V^{(i)}$  appears in the decomposition.

**Proposition 4.** Let  $G$  be a finite group and consider a decomposition of its group algebra  $\mathbb{C}[G] = \oplus_i m_i V^{(i)}$  where the  $V^{(i)}$  form a complete list of pairwise inequivalent irreducible  $G$ -modules. Then,

1.  $m_i = \dim V^{(i)}$ ,
2.  $\sum_i (\dim V^{(i)})^2 = |G|$ , and
3. The number of  $V^{(i)}$  equals the number of conjugacy classes of  $G$ .

**Example 3.** Let  $G = S_n$ . Of course it is well known that the number of conjugacy classes for any  $S_n$  equals the number of partitions of  $n$ . Furthermore, each class consists of permutations having the same cycle structure because the action of conjugation preserves the cycle structure.

**Example 4.** Let  $G = D_{2n}$ . The number of conjugacy classes for the dihedral group was discussed in Example 2. For example,  $D_6$  and  $D_8$  have three and five conjugacy classes, respectively. Thus,

- (8) Conjugacy classes of  $D_6$  :  $\{e\}, \{r, r^2\}, \{p, rp, r^2p\},$   
 (9) Conjugacy classes of  $D_8$  :  $\{e\}, \{r^2\}, \{r, r^3\}, \{p, r^2p\}, \{rp, r^3p\}.$

**Example 5.** Conjugacy classes of the quaternionic (or, dicyclic) group  $Q_{2n}$  which appears, along with the dihedral group  $D_{2n}$ , among the Salingaros' vee groups [18–20], can be found by hand (for low orders) or by using a computer software such as the Maple package [1]. For example, the group

$$Q_8 = \{\pm 1, \pm i, \pm j, \pm k\} \quad \text{where} \quad i^2 = j^2 = k^2 = ijk = -1,$$

has the following five conjugacy classes:

- (10)  $\{1\}, \{-1\}, \{i, -i\}, \{j, -j\}, \{k, -k\}.$

The orthogonality relations of the first kind stated in Theorem 4 are complemented by the so called *orthogonality relations of the second kind*. While the relations of the first kind refer to the rows of the character table, the relations of the second kind refer to the columns.

**Theorem 6.** Let  $K, L$  be conjugacy classes of  $G$ . Then

$$\sum_{\chi} \chi_K \bar{\chi}_L = \frac{|G|}{|K|} \delta_{K,L},$$

where the sum is over all irreducible characters of  $G$ .

In Section 2, we will compute all irreducible representations and characters of all Salingaros' vee groups of orders 4, 8 and 16, and verify Theorems 4 and 6.

## 2. Salingaros' vee groups

In this section, we state the definition of Salingaros' vee groups and discuss some of their properties. Then, Salingaros' classification of these groups will be reviewed. Furthermore, irreducible representations and their character tables will be presented for a few sample groups.

### 2.1. General definitions and properties

The vee groups were introduced by Salingaros in [18–20]. They were more recently studied in [2–4, 22] where they were denoted as  $G_{p,q}$ . In particular, these groups are central extensions of extra-special 2-groups. [6, 9–11, 13, 22]



**Definition 3.** Let  $Cl_{p,q}$  be the real Clifford algebra of a non-degenerate quadratic form with signature  $(p, q)$  and let  $\mathcal{B} = \{e_{\underline{i}} \mid 0 \leq |\underline{i}| \leq n\}$  be a basis for  $Cl_{p,q}$  consisting of basis monomials  $e_{\underline{i}} = e_{i_1}e_{i_2} \cdots e_{i_k}$ ,  $i_1 < i_2 < \cdots < i_k$ , for  $0 \leq k \leq n$  where  $n = p+q$ . The 1-vector generators  $e_i$ ,  $1 \leq i \leq n$ , satisfy the following relations:

$$e_i^2 = \begin{cases} 1 & \text{if } 1 \leq i \leq p, \\ -1 & \text{if } p+1 \leq i \leq n, \end{cases} \quad \text{and} \quad e_i e_j = -e_j e_i \text{ for } i \neq j.$$

The Salingaros' vee group  $G_{p,q} \subset Cl_{p,q}$  is the set  $G_{p,q} = \{\pm e_{\underline{i}} \mid e_{\underline{i}} \in \mathcal{B}\}$  with the Clifford algebra multiplication as the group binary operation. Thus,  $|G_{p,q}| = 2 \cdot 2^{p+q} = 2^{n+1}$ .

Notice that  $G_{p,q}$  may be presented as follows:

$$(11) \quad G_{p,q} = \langle -1, e_1, \dots, e_n \mid e_i e_j = -e_j e_i \text{ for } i \neq j \text{ and } e_i^2 = \pm 1 \rangle,$$

where  $e_i^2 = 1$  for  $1 \leq i \leq p$  and  $e_i^2 = -1$  for  $p+1 \leq i \leq n = p+q$ . In the following, the elements  $e_i = e_{i_1}e_{i_2} \cdots e_{i_k}$  will be denoted for short as  $e_{i_1 i_2 \dots i_k}$  for  $k \geq 1$  while  $e_{\emptyset}$  will be denoted as 1, the identity element of  $G_{p,q}$  (and  $Cl_{p,q}$ ).

For the properties of the prime power groups we refer to [10, 13, 16].

**Theorem 7. (Cauchy)** *If  $G$  is a finite group whose order is divisible by a prime  $p$  then  $G$  contains an element of order  $p$ .*

Since all Salingaros' vee groups are of order  $2^n$  for some positive integer  $n$ , there are elements of order 2 in  $G_{p,q}$ . In fact, as it will be seen later, any element in  $G_{p,q}$  is of order 1, 2, or 4 only.

Let  $G = G_{p,q}$ . Since each  $C_{G_{p,q}}(x_i)$  is a proper subgroup of  $G_{p,q}$  for  $x_i \notin Z(G_{p,q})$  and  $G_{p,q}$  is a 2-group, Lagrange's theorem gives that  $[G_{p,q} : C_{G_{p,q}}(x_i)]$  is a divisor of  $|G_{p,q}|$ , hence it is a power of 2. This implies that  $2 \mid |Z(G_{p,q})|$ . Thus,  $Z(G_{p,q}) \neq \{1\}$ , which gives the following result.

**Lemma 1.** *The center of any Salingaros' vee group is non trivial and it is of order  $2^n$  for some  $n \geq 1$ .*

In fact, from the structure theorem of Clifford algebras (see [2, 3] and references therein) one can learn that

$$(12) \quad Z(Cl_{p,q}) = \begin{cases} \{1\} & \text{if } p+q \text{ is even;} \\ \{1, \beta\} & \text{if } p+q \text{ is odd,} \end{cases}$$

where  $\beta = e_1 e_2 \cdots e_n$ ,  $n = p+q$ , is the unit pseudoscalar in  $Cl_{p,q}$ . This leads to the following conclusion (see also [22]).

**Theorem 8.** *Let  $G_{p,q} \subset \mathcal{C}\ell_{p,q}$ . Then,*

$$(13) \quad Z(G_{p,q}) = \begin{cases} \{\pm 1\} \cong \mathbb{Z}_2 & \text{if } p - q \equiv 0, 2, 4, 6 \pmod{8}; \\ \{\pm 1, \pm \beta\} \cong \mathbb{Z}_2 \times \mathbb{Z}_2 & \text{if } p - q \equiv 1, 5 \pmod{8}; \\ \{\pm 1, \pm \beta\} \cong \mathbb{Z}_4 & \text{if } p - q \equiv 3, 7 \pmod{8}. \end{cases}$$

The following result implies that the vee groups of order  $2^2$  are abelian. For the proof of this proposition, see [16].

**Proposition 5.** *If  $p$  is a prime, then every group  $G$  of order  $p^2$  is abelian.*

It is worth to know the order relation of the normal subgroups of the Salingaros' vee groups.

**Proposition 6.** *If a group  $G$  is of order  $|G| = p^n$ , then  $G$  has a normal subgroup of order  $p^m$  for every  $m \leq n$ .*

So, this result tells that  $G_{p,q}$  of order  $2^{p+q+1}$  has a normal subgroup of order  $2^m$  for any  $m \leq p + q + 1$ , which implies that  $G_{p,q}$  are not simple groups.

## 2.2. Conjugacy classes

In this section we discuss the conjugacy classes of  $G_{p,q}$  using Theorem 8. It is convenient to separately address the two cases when  $n = p + q$  is odd or even.

Suppose that  $n$  is even. Then,  $Z(G_{p,q}) = \{\pm 1\}$  (see Theorem 8) and so  $\{1\}$  and  $\{-1\}$  are the only conjugacy classes in  $G_{p,q}$  with a single element. This is because the unit pseudoscalar  $\beta$  is not in the center. All other classes always have two elements  $\{g, -g\}$  for any non central group element  $g$ . Thus, the number of conjugacy classes is  $N = 1 + 2^{p+q}$  and the classes are:

$$(14) \quad \{1\}, \{-1\}, \{e_1, -e_1\}, \dots, \{\beta, -\beta\}.$$

Now consider the second case when  $n$  is odd. The center  $Z(G_{p,q})$  has four elements  $\{\pm 1, \pm \beta\}$ . Hence,  $\{1\}, \{-1\}, \{\beta\}$ , and  $\{-\beta\}$  are the only classes with a single element whereas all other classes have two elements  $\{g, -g\}$  for any non central element  $g$ . Thus, the number of conjugacy classes is  $N = 2 + 2^{p+q}$  and the classes are:

$$(15) \quad \{1\}, \{-1\}, \{\beta\}, \{-\beta\}, \{e_1, -e_1\}, \dots, \{e_{12\dots(n-1)}, -e_{12\dots(n-1)}\}.$$

The above results can be given as the following theorem.

**Theorem 9.** *Let  $N$  be the number of conjugacy classes in  $G_{p,q}$ . Then,*

$$(16) \quad N = \begin{cases} 1 + 2^{p+q} & \text{if } p + q \text{ is even;} \\ 2 + 2^{p+q} & \text{if } p + q \text{ is odd.} \end{cases}$$

*Proof.* Note that any two elements  $\tau, g \in G_{p,q}$  are basis monomials from  $\mathcal{C}\ell_{p,q}$  which either commute  $\tau g = g\tau$  or anticommute  $\tau g = -g\tau$ . If  $\tau \in Z(G_{p,q})$  then  $g\tau g^{-1} = \tau$  for all  $g \in G_{p,q}$ . So  $\tau^{G_{p,q}} = \{\tau\}$  for all  $\tau \in Z(G_{p,q})$ . If  $\tau \notin Z(G_{p,q})$ , then there exists  $g \in G_{p,q}$  such that  $\tau g = -g\tau$ , i.e.,  $g\tau g^{-1} = -\tau$ . Hence,  $\tau^{G_{p,q}} = \{\tau, -\tau\}$  for all  $\tau \notin Z(G_{p,q})$ . From Lemma 8, the number of elements in  $Z(G_{p,q})$  for even and odd cases are known. Then, the formulas for  $N$  follow immediately. ■

Salingaros lists five classes of vee groups in [18] and references therein. He denotes these groups as:  $N_{2k-1}$ ,  $N_{2k}$ ,  $\Omega_{2k-1}$ ,  $\Omega_{2k}$ ,  $S_k$ . The groups  $N_{2k-1}$  and  $N_{2k}$  are included in the Clifford algebras  $\mathcal{C}\ell_{p,q}$  when  $p+q$  is even, whereas  $\Omega_{2k-1}$ ,  $\Omega_{2k}$ , and  $S_k$  are included in the Clifford algebras  $\mathcal{C}\ell_{p,q}$  when  $p+q$  is odd. In particular, the groups  $S_k$  are included in those Clifford algebras in which the unit pseudoscalar  $\beta$  squares to  $-1$  whereas  $\Omega_{2k-1}$  and  $\Omega_{2k}$  are included in those semisimple algebras in which  $\beta$  squares to 1. The basic information about these groups is summarized in Table 1.

One other distinguishing feature of these groups is their order structure which is different from one class to another. Knowing the order structure of  $G_{p,q}$  allows one to determine its class. For example, the first few vee groups corresponding to the Clifford algebras in dimensions one, two and three, are:

Groups of order 4:  $G_{1,0} = D_4$ ,  $G_{0,1} = \mathbb{Z}_4$ ,

Groups of order 8:  $G_{2,0} = D_8 = N_1$ ,  $G_{1,1} = D_4 = N_1$ ,  $G_{0,2} = Q_8 = N_2$ ,

Groups of order 16:  $G_{3,0} = S_1$ ,  $G_{2,1} = \Omega_1$ ,  $G_{1,2} = S_1$ ,  $G_{0,3} = \Omega_2$ ,

where  $D_8$  is the dihedral group of a square from Example 4 whereas  $Q_8$  is the quaternionic group from Example 10.

Tab. 1: Vee groups  $G_{p,q}$  in Clifford algebras  $\mathcal{C}\ell_{p,q}$ .

Group	Center	Group order	$\dim_{\mathbb{R}} \mathcal{C}\ell_{p,q}$
$N_{2k-1}$	$\mathbb{Z}_2$	$2^{2k+1}$	$2^{2k}$
$N_{2k}$	$\mathbb{Z}_2$	$2^{2k+1}$	$2^{2k}$
$\Omega_{2k-1}$	$\mathbb{Z}_2 \times \mathbb{Z}_2$	$2^{2k+2}$	$2^{2k+1}$
$\Omega_{2k}$	$\mathbb{Z}_2 \times \mathbb{Z}_2$	$2^{2k+2}$	$2^{2k+1}$
$S_k$	$\mathbb{Z}_4$	$2^{2k+2}$	$2^{2k+1}$

**Definition 4.** The order structure of  $G_{p,q}$  is a 3-tuple  $(n_1, n_2, n_3)$  of nonnegative integers where  $n_1$ ,  $n_2$  and  $n_3$  give the number of elements in  $G_{p,q}$  of order one, two and four, respectively.

The following theorem gives the number of inequivalent representations of degree one of the group  $G_{p,q}$ .

**Theorem 10.** Let  $M$  be the number of inequivalent representations of degree one of  $G_{p,q}$ . Then,

$$(17) \quad M = \begin{cases} 2 \cdot 2^{p+q} = 4 & \text{if } p + q = 1; \\ 2^{p+q} & \text{if } p + q \geq 2. \end{cases}$$

*Proof.* From Theorem 2, the number of degree one representations of  $G_{p,q}$  is the index of its commutator subgroup  $[G_{p,q} : G'_{p,q}]$ . When  $p + q = 1$ , the commutator subgroup  $G'_{p,q} = \{1\}$  and so

$$M = [G_{p,q} : G'_{p,q}] = (2 \cdot 2^1)/1 = 4.$$

For  $p + q \geq 2$ ,  $G'_{p,q} = \{1, -1\}$ , so

$$M = [G_{p,q} : G'_{p,q}] = (2 \cdot 2^{p+q})/2 = 2^{p+q},$$

as desired. ■

Note that Maschke's Theorem 1 gives the decomposition  $\mathbb{C}[G_{p,q}] = \oplus_i^N m_i V^{(i)}$  and from Proposition 4, one gets  $|\mathbb{C}[G_{p,q}]| = \sum_{i=1}^N m_i^2$ . From the above theorem, provided that  $M$  is the number of degree one representations of the group, the dimension of the group algebra  $\mathbb{C}[G_{p,q}]$  can be rewritten as

$$(18) \quad |\mathbb{C}[G_{p,q}]| = M + \sum_{i=M+1}^N m_i^2.$$

Thus, the difference  $N - M$  is the number of inequivalent irreducible representations of  $G_{p,q}$  with degree two or more. This can be formally stated as the following result.

**Theorem 11.** *Let  $L$  be the number of inequivalent irreducible representations with degree two or more of  $G_{p,q}$ . (i) Let  $p + q \geq 2$ . If  $p + q$  is even, then  $L = 1$  otherwise  $L = 2$ . (ii) When  $p + q = 1$ , then  $L = 0$ .*

*Proof.* The proof follows immediately from Theorems 9 and 10. ■

In the remainder of this section, we give the order structure and conjugacy classes of Salingaros' vee groups of orders 4, 8, and 16.

**Example 6.** *Consider the abelian groups  $G_{1,0}$  and  $G_{0,1}$ . The number of conjugacy classes is  $N = 2 + 2^1 = 4$  as predicted by Theorem 9, and the conjugacy classes are:*

$$(19) \quad K_1 = \{1\}, \quad K_2 = \{-1\}, \quad K_3 = \{e_1\}, \quad K_4 = \{-e_1\}.$$

*Since the groups  $G_{1,0}$  and  $G_{0,1}$  have the same conjugacy classes, what distinguishes them is their order structure. The order structure of these groups is summarized in Table 2 where C.O.S. and G.O.S. give the center order structure and the group order structure, respectively, of each group. Also,  ${}^2\text{Mat}(1, \mathbb{R})$  denotes  $\text{Mat}(1, \mathbb{R}) \oplus \text{Mat}(1, \mathbb{R})$ .*

Tab. 2: Vee groups  $G_{p,q}$  of order 4 for  $p + q = 1$ .

(p,q)	Group	$\mathcal{C}\ell_{p,q}$	Center	$\beta^2$	C.O.S.	G.O.S.	$L$	$M$	$N$
(1,0)	$G_{1,0} = D_4$	${}^2\text{Mat}(1, \mathbb{R})$	$\mathbb{Z}_2 \times \mathbb{Z}_2$	+1	(1, 3, 0)	(1, 3, 0)	0	4	4
(0,1)	$G_{0,1} = \mathbb{Z}_4$	$\text{Mat}(1, \mathbb{C})$	$\mathbb{Z}_4$	-1	(1, 1, 2)	(1, 1, 2)	0	4	4

**Example 7.** Consider the non-abelian groups  $G_{2,0}$ ,  $G_{1,1}$ , and  $G_{0,2}$ . It is easy to check that the conjugacy classes for these groups are:

$$(20) \quad K_1 = \{1\}, K_2 = \{-1\}, K_3 = \{e_1, -e_1\}, K_4 = \{e_2, -e_2\}, K_5 = \{e_{12}, -e_{12}\}$$

which matches the formula  $N = 1 + 2^2 = 5$ . The order structure of these groups is summarized in Table 3.

**Example 8.** Consider the non-abelian groups  $G_{3,0}$ ,  $G_{2,1}$ ,  $G_{1,2}$ , and  $G_{0,3}$ . The number of conjugacy classes is  $N = 2 + 2^3 = 10$  as predicted earlier by Theorem 9. Thus, the conjugacy classes for each of these groups are:

$$(21) \quad \begin{aligned} K_1 &= \{1\}, K_2 = \{-1\}, K_3 = \{e_{123}\}, K_4 = \{-e_{123}\}, K_5 = \{e_1, -e_1\}, \\ K_6 &= \{e_2, -e_2\}, K_7 = \{e_3, -e_3\}, K_8 = \{e_{12}, -e_{12}\}, \\ K_9 &= \{e_{13}, -e_{13}\}, K_{10} = \{e_{23}, -e_{23}\}. \end{aligned}$$

The order structure for each group is given in Table 4.

In the next section, we will present all irreducible representations of all distinct classes of Salingaros' vee groups of orders 4, 8, and 16.

Tab. 3: Vee groups  $G_{p,q}$  of order 8 for  $p + q = 2$ .

(p,q)	Group	Class	$\mathcal{C}\ell_{p,q}$	Center	$\beta^2$	C.O.S.	G.O.S.	$L$	$M$	$N$
(2,0)	$G_{2,0}=D_8$	$N_1$	$\text{Mat}(2, \mathbb{R})$	$\mathbb{Z}_2$	-1	(1, 1, 0)	(1, 5, 2)	1	4	5
(1,1)	$G_{1,1}=D_8$	$N_1$	$\text{Mat}(2, \mathbb{R})$	$\mathbb{Z}_2$	+1	(1, 1, 0)	(1, 5, 2)	1	4	5
(0,2)	$G_{0,2}=Q_8$	$N_2$	$\text{Mat}(1, \mathbb{H})$	$\mathbb{Z}_2$	-1	(1, 1, 0)	(1, 1, 6)	1	4	5

Tab. 4: Vee groups  $G_{p,q}$  of order 16 for  $p + q = 3$ .

(p,q)	Group	Class	$\mathcal{C}\ell_{p,q}$	Center	$\beta^2$	C.O.S.	G.O.S.	$L$	$M$	$N$
(3,0)	$G_{3,0}$	$S_1$	$\text{Mat}(2, \mathbb{C})$	$\mathbb{Z}_4$	-1	(1, 1, 2)	(1, 7, 8)	2	8	10
(2,1)	$G_{2,1}$	$\Omega_1$	${}^2\text{Mat}(2, \mathbb{R})$	$\mathbb{Z}_2 \times \mathbb{Z}_2$	+1	(1, 3, 0)	(1, 11, 4)	2	8	10
(1,2)	$G_{1,2}$	$S_1$	$\text{Mat}(2, \mathbb{C})$	$\mathbb{Z}_4$	-1	(1, 1, 2)	(1, 7, 8)	2	8	10
(0,3)	$G_{0,3}$	$\Omega_2$	${}^2\text{Mat}(1, \mathbb{H})$	$\mathbb{Z}_2 \times \mathbb{Z}_2$	+1	(1, 3, 0)	(1, 3, 12)	2	8	10

### 3. Irreducible representations of vee groups of order 4, 8, and 16

In this section we compute all irreducible representations and their characters of Salingaros vee groups of orders 4, 8 and 16.

It is convenient and relatively easy to find decompositions and  $G$ -invariant submodules in the group algebras of the symmetric group and of its subgroups by using **SymGroupAlgebra**, a package for Maple [1]. Therefore, in order to decompose the group algebra  $\mathbb{C}[G_{p,q}]$  into irreducible submodules, for each vee group of interest, one first finds a subgroup  $S$  of the symmetric group  $S_n$ ,  $n = 2^{1+p+q}$ , isomorphic to  $G_{p,q}$ . For each vee group, its isomorphic copy  $S$  can be found from the Cayley's multiplication table of  $G_{p,q}$ . In fact, it is enough to find images of the generators of  $G_{p,q}$  under the group isomorphism  $G_{p,q} \xrightarrow{F} S < S_n$ . This isomorphism extends uniquely to a linear isomorphism, also denoted by  $F$ , of the corresponding group algebras  $\mathbb{C}[G_{p,q}] \xrightarrow{F} \mathbb{C}[S] < \mathbb{C}[S_n]$ . Thus, all computations have been performed in  $\mathbb{C}[S_n]$  and the results have been brought back to  $\mathbb{C}[G_{p,q}]$  by  $F^{-1}$ .

In the following, we consider the irreducible representations and their characters of  $G_{p,q}$  for  $p + q = 1, 2, 3$ . While the character tables of all groups of order less than 32 can be found in the literature, for example in [12], the path followed here is to, first, explicitly decompose the group algebras  $\mathbb{C}[G_{p,q}]$  into irreducible  $G_{p,q}$ -submodules by finding bases for these submodules, and, second, compute the irreducible representations for  $G_{p,q}$  and their character tables using the elements of the representation theory presented earlier. In the process, one discovers a useful application for the Groebner basis technique [8] when searching for the bases in the  $G_{p,q}$ -invariant submodules.

#### 3.1. Groups of order 4

Since the vee groups  $G_{1,0}$  and  $G_{0,1}$  of order 4 are isomorphic to  $D_4 \cong \mathbb{Z}_2 \times \mathbb{Z}_2$  and  $\mathbb{Z}_4$ , respectively, their character tables are easy to compute by hand and are well-known. For completeness and in preparation for handling groups of higher orders, it is worth to describe an algorithm for finding irreducible representations, and their characters, of these groups. Since both groups are abelian, their conjugacy classes are one-element classes.

##### 3.1.1. The group $G_{1,0} = D_4$

The group  $G_{1,0}$  is generated by  $-1$  and  $e_1$  with  $e_1^2 = 1$  while the group  $S \subset S_4$  isomorphic to it is generated by the permutations  $(1, 2)(3, 4)$  and  $(1, 3)(2, 4)$  (see Table 5). That is,  $-1 \mapsto (1, 2)(3, 4)$  and  $e_1 \mapsto (1, 3)(2, 4)$  under the isomorphism  $F$  mentioned above. For completeness,  $-e_1 \mapsto (1, 4)(2, 3)$  and  $1 \mapsto (1)$ .

One needs to find four vectors  $\mathbf{u}_1$ ,  $\mathbf{u}_2$ ,  $\mathbf{u}_3$ , and  $\mathbf{u}_4$  which span 1-dimensional  $G_{1,0}$ -invariant subspaces  $V^{(1)}$ ,  $V^{(2)}$ ,  $V^{(3)}$ , and  $V^{(4)}$  such that

$$(22) \quad \mathbb{C}[G_{1,0}] = V^{(1)} \oplus V^{(2)} \oplus V^{(3)} \oplus V^{(4)}$$

and  $V^{(i)} = \text{span}\{\mathbf{u}_i\}$ ,  $i = 1, \dots, 4$ . Notice that all  $V^{(i)}$  are of dimension 1 since the group is abelian and all irreducible modules are one dimensional. The following algorithm can be used to find the basis vectors.

**Algorithm 1.**

- 1: Let  $G = S \cong G_{1,0}$  and  $V = \mathbb{C}[S] \cong \mathbb{C}[G_{1,0}]$ .
- 2: Let  $\mathbf{u}_1$  be the sum of all basis elements in  $V$  and define  $V^{(1)} = \text{span}\{\mathbf{u}_1\}$ . Such subspace always carries the trivial representation and it is  $G$ -invariant since  $g\mathbf{u}_1 = \mathbf{u}_1$  for every  $g \in G$ .
- 3: Compute a basis for the orthogonal complement of  $V^{(1)}$  in  $V$  and rename this complement as  $V$ . This orthogonal complement is obviously 3-dimensional and it is  $G$ -invariant by Proposition 1.
- 4: Using Groebner basis technique [8], find a 1-dimensional  $G$ -invariant subspace  $V^{(2)}$  in  $V$  and find its spanning vector  $\mathbf{u}_2$ .
- 5: Find a 2-dimensional orthogonal complement of  $V^{(2)}$  in  $V$ . Call this complement  $V$ . By the same reasoning, it is  $G$ -invariant.
- 6: Find a 1-dimensional  $G$ -invariant subspace  $V^{(3)}$  in  $V$  different from  $V^{(2)}$  and its spanning vector  $\mathbf{u}_3$ .
- 7: Find a basis for the orthogonal complement  $V^{(4)}$  of  $V^{(1)} \oplus V^{(2)} \oplus V^{(3)}$  in  $\mathbb{C}[G_{1,0}]$  and its spanning vector  $\mathbf{u}_4$ .
- 8: The algorithm terminates since the dimension of  $\mathbb{C}[G_{1,0}]$  is finite.

From the above procedure, one obtains all basis vectors  $\mathbf{u}_i$  as linear combinations of the standard basis  $\mathcal{B} = \{1, -1, e_1, -e_1\}$  of  $\mathbb{C}[G_{1,0}]$  as follows:

$$\begin{aligned}
 V^{(1)} &= \text{span}\{\mathbf{u}_1\}, & \mathbf{u}_1 &= (1)1 + (1)(-1) + (1)(e_1) + (1)(-e_1), \\
 V^{(2)} &= \text{span}\{\mathbf{u}_2\}, & \mathbf{u}_2 &= (1)1 + (-1)(-1) + (-1)(e_1) + (1)(-e_1), \\
 V^{(3)} &= \text{span}\{\mathbf{u}_3\}, & \mathbf{u}_3 &= (-1)1 + (1)(-1) + (-1)(e_1) + (1)(-e_1), \\
 V^{(4)} &= \text{span}\{\mathbf{u}_4\}, & \mathbf{u}_4 &= (-1)1 + (-1)(-1) + (1)(e_1) + (1)(-e_1).
 \end{aligned}
 \tag{23}$$

Once the decomposition (22) has been determined, one can find all four irreducible inequivalent representations  $X^{(1)}$ ,  $X^{(2)}$ ,  $X^{(3)}$ , and  $X^{(4)}$  in the corresponding subspaces  $V^{(1)}$ ,  $V^{(2)}$ ,  $V^{(3)}$ , and  $V^{(4)}$ . These are all 1-dimensional and can be read off from the following character table.

$$\begin{array}{c|cccc}
 \text{char/class} & K_1 & K_2 & K_3 & K_4 \\
 \hline
 \chi^{(1)} & 1 & 1 & 1 & 1 \\
 \chi^{(2)} & 1 & -1 & -1 & 1 \\
 \chi^{(3)} & 1 & -1 & 1 & -1 \\
 \chi^{(4)} & 1 & 1 & -1 & -1
 \end{array}
 \tag{24}$$

The explicit matrix representations are shown in Table 12 in Appendix B. Note that in the character table, rows and columns are orthonormal. Let  $\chi^{(i)}$  denote the character of the representation  $X^{(i)}$ . So, for example, the inner product of the characters  $\chi^{(2)}$  and  $\chi^{(3)}$  from the above table is computed as follows:

$$\langle \chi^{(2)}, \chi^{(3)} \rangle = \frac{1}{4} \sum_{i=1}^4 |K_i| \chi_{K_i}^{(2)} \overline{\chi_{K_i}^{(3)}} = \frac{1}{4} ((1)(1) + (-1)(-1) + (-1)(1) + (1)(-1)) = 0$$

since  $|K_i| = 1$  for each class. This verifies the character orthogonality relation of the first kind. In a similar manner one can verify the character relation of the second kind.

### 3.1.2. The group $G_{0,1} = \mathbb{Z}_4$

The group  $G_{0,1}$  is generated by  $-1$  and  $e_1$  with  $e_1^2 = -1$  while the group  $S \subset S_4$  isomorphic to it is generated by the permutations  $(1, 2)(3, 4)$  and  $(1, 3, 2, 4)$  (see Table 5). That is,  $-1 \mapsto (1, 2)(3, 4)$  and  $e_1 \mapsto (1, 3, 2, 4)$  under the isomorphism  $F$ . For completeness,  $-e_1 \mapsto (1, 4, 2, 3)$  and  $1 \mapsto (1)$ .

One needs to again find four vectors  $\mathbf{u}_1, \mathbf{u}_2, \mathbf{u}_3, \mathbf{u}_4$  which span 1-dimensional  $G_{0,1}$ -invariant subspaces  $V^{(1)}, V^{(2)}, V^{(3)}$ , and  $V^{(4)}$  such that

$$(25) \quad \mathbb{C}[G_{0,1}] = V^{(1)} \oplus V^{(2)} \oplus V^{(3)} \oplus V^{(4)}$$

and  $V^{(i)} = \text{span}\{\mathbf{u}_i\}$ ,  $i = 1, \dots, 4$ . The subspaces  $V^{(i)}$  again are of dimension 1 since  $G_{0,1}$  is abelian and so all its irreducible modules are one dimensional. Applying now Algorithm 1 to  $\mathbb{C}[G_{0,1}]$ , one finds this basis:

$$(26) \quad \begin{aligned} V^{(1)} &= \text{span}\{\mathbf{u}_1\}, & \mathbf{u}_1 &= (1)(1) + (1)(-1) + (1)(e_1) + (1)(-e_1), \\ V^{(2)} &= \text{span}\{\mathbf{u}_2\}, & \mathbf{u}_2 &= (-i)1 + (i)(-1) + (-1)(e_1) + (1)(-e_1), \\ V^{(3)} &= \text{span}\{\mathbf{u}_3\}, & \mathbf{u}_3 &= (-1)1 + (-1)(-1) + (1)(e_1) + (-1)(-e_1), \\ V^{(4)} &= \text{span}\{\mathbf{u}_4\}, & \mathbf{u}_4 &= (i)1 + (-i)(-1) + (-1)(e_1) + (1)(-e_1). \end{aligned}$$

Once the decomposition (25) has been found, one can determine all four irreducible inequivalent representations  $X^{(1)}, X^{(2)}, X^{(3)}$ , and  $X^{(4)}$  in the corresponding subspaces  $V^{(1)}, V^{(2)}, V^{(3)}$ , and  $V^{(4)}$ . These are all 1-dimensional and can be read off from the character table.

$$(27) \quad \begin{array}{c|cccc} \text{char/class} & K_1 & K_2 & K_3 & K_4 \\ \hline \chi^{(1)} & 1 & 1 & 1 & 1 \\ \chi^{(2)} & 1 & -1 & i & -i \\ \chi^{(3)} & 1 & 1 & -1 & -1 \\ \chi^{(4)} & 1 & -1 & -i & i \end{array}$$

The explicit matrix representations are shown in Table 13 in Appendix B. Like in the previous example, one can verify that the columns and rows in the above character table are orthonormal. This is in agreement with the character orthogonality relations of the first and of the second kind.



### 3.2. Groups of order 8

Since the vee groups  $G_{2,0}$ ,  $G_{1,1}$  and  $G_{0,2}$  are isomorphic to  $D_8$ ,  $D_8$  and  $Q_8$ , respectively, their character tables are easy to compute by hand and are well-known. However, computation of their representations is not so simple. For completeness and in preparation for handling groups of order 16, we describe an algorithm for finding irreducible representations and characters of these groups. Note that the conjugacy classes for these groups are shown in (20).

#### 3.2.1. The extra-special group $G_{2,0} = D_8 = N_1$

The group  $G_{2,0}$  is generated by  $-1$ ,  $e_1$  and  $e_2$  with  $e_1^2 = e_2^2 = 1$ ,  $e_1 e_2 = -e_2 e_1$ , while the group  $S \subset S_8$  isomorphic to  $G_{2,0}$  is generated by the permutations  $(1, 2)(3, 4)(5, 6)(7, 8)$ ,  $(1, 3)(2, 4)(5, 7)(6, 8)$  and  $(1, 5)(2, 6)(3, 8)(4, 7)$  (see Table 6). That is,

$$-1 \mapsto (1, 2)(3, 4)(5, 6)(7, 8), \quad e_1 \mapsto (1, 3)(2, 4)(5, 7)(6, 8), \quad e_2 \mapsto (1, 5)(2, 6)(3, 8)(4, 7)$$

under the isomorphism  $F$  mentioned above.

In a manner similar to  $G_{1,0}$ , we describe an algorithm for finding the decomposition of  $\mathbb{C}[G_{2,0}]$  into invariant subspaces

$$(28) \quad \mathbb{C}[G_{2,0}] = \bigoplus_{i=1}^6 V^{(i)},$$

where  $V^{(i)} = \text{span}\{\mathbf{u}_i\}$ ,  $i = 1, \dots, 4$ , are one-dimensional subspaces while  $V^{(5)}$  and  $V^{(6)}$  are two-dimensional subspaces carrying equivalent representations according to Proposition 4, Theorem 10 and Theorem 11.

The basis vectors  $\mathbf{u}_i$ ,  $i = 1, \dots, 8$ , are displayed in (43) in Appendix B. They have been found by using the following algorithm.

#### Algorithm 2.

- 1: Let  $G = S \cong G_{2,0}$  and  $V = \mathbb{C}[S] \cong \mathbb{C}[G_{2,0}]$ .
- 2: Apply Algorithm 1 to find vectors  $\mathbf{u}_1, \mathbf{u}_2, \mathbf{u}_3, \mathbf{u}_4$  providing bases for the one-dimensional  $G$ -invariant submodules  $V^{(1)}, V^{(2)}, V^{(3)}, V^{(4)}$  in  $V$ .
- 3: Find a basis for the orthogonal complement of  $V^{(1)} \oplus V^{(2)} \oplus V^{(3)} \oplus V^{(4)}$  in  $V$  and call it  $V$ . It is 4-dimensional.
- 4: Using Groebner basis technique, find any 2-dimensional  $G$ -invariant subspace in  $V$  and call it  $V^{(5)}$ . That is, find its basis vectors  $\mathbf{u}_5$  and  $\mathbf{u}_6$ .
- 5: Find a basis for the orthogonal complement of  $V^{(5)}$  in  $V$  and call it  $V^{(6)}$ . That is, find its spanning vectors  $\mathbf{u}_7$  and  $\mathbf{u}_8$ .
- 6: The algorithm terminates when all eight vectors  $\mathbf{u}_1, \dots, \mathbf{u}_8$  are found and these vectors provide a basis for the decomposition of  $\mathbb{C}[G_{2,0}]$ .

Once the decomposition of  $\mathbb{C}[G_{2,0}]$  has been found, one can compute all irreducible representations  $X^{(i)}$ ,  $i = 1, \dots, 6$ , of  $G_{2,0}$  in the six invariant submodules  $V^{(i)}$ . The degree-one representations  $X^{(1)}$ ,  $X^{(2)}$ ,  $X^{(3)}$ , and  $X^{(4)}$  are all inequivalent since their characters are different as shown in the character table below. The two irreducible representations  $X^{(5)}$  and  $X^{(6)}$  of degree two are equivalent. All representations are displayed in Table 14 in Appendix B. The extended character table with all representations, including the equivalent ones, for  $G_{2,0}$  is as follows:

char/class	$K_1$	$K_2$	$K_3$	$K_4$	$K_5$
$\chi^{(1)}$	1	1	1	1	1
$\chi^{(2)}$	1	1	-1	-1	1
$\chi^{(3)}$	1	1	1	-1	-1
$\chi^{(4)}$	1	1	-1	1	-1
$\chi^{(5)}$	2	-2	0	0	0
$\chi^{(6)}$	2	-2	0	0	0

Note that  $X^{(5)}$  and  $X^{(6)}$  are equivalent since their characters are the same. To illustrate the character orthogonality relations, compute the inner product of the characters  $\chi^{(2)}$  and  $\chi^{(3)}$  while taking into consideration the number of elements in each conjugacy class:

$$\begin{aligned}
 \langle \chi^{(2)}, \chi^{(3)} \rangle &= \frac{1}{8} \sum_{i=1}^5 |K_i| \chi_{K_i}^{(2)} \overline{\chi_{K_i}^{(3)}} \\
 (30) \quad &= \frac{1}{8} (1 \cdot (1)(1) + 1 \cdot (1)(1) + 2 \cdot (-1)(1) + 2 \cdot (-1)(-1) + 2 \cdot (1)(-1)) \\
 &= 0.
 \end{aligned}$$

In a similar manner one can verify the character relation of the second kind.

Since the group  $G_{1,1}$  since it belongs to the same class  $N_1$  as  $G_{2,0}$ , it will be not discussed separately.

### 3.2.2. The extra-special group $G_{0,2} = Q_8 = N_2$

The group  $G_{0,2}$  is generated by  $-1$ ,  $e_1$  and  $e_2$  with  $e_1^2 = e_2^2 = -1$ ,  $e_1 e_2 = -e_2 e_1$  while the group  $S \subset S_8$  isomorphic to  $G_{0,2}$  is generated by the permutations  $(1, 2)(3, 4)(5, 6)(7, 8)$ ,  $(1, 3, 2, 4)(5, 7, 6, 8)$  and  $(1, 5, 2, 6)(3, 8, 4, 7)$  (see Table 6). So,

$$-1 \mapsto (1, 2)(3, 4)(5, 6)(7, 8), \quad e_1 \mapsto (1, 3, 2, 4)(5, 7, 6, 8), \quad e_2 \mapsto (1, 5, 2, 6)(3, 8, 4, 7)$$

under the isomorphism  $F$ .

Since the group algebra  $\mathbb{C}[G_{0,2}]$  formally decomposes like (28), using Algorithm 2 one can find the decomposition of  $\mathbb{C}[G_{0,2}]$ . The basis vectors spanning the invariant subspaces are shown in (45) in Appendix B. Once the decomposition has been found, one can compute all six irreducible representations  $X^{(i)}$ ,  $i = 1, \dots, 6$ , in the corresponding submodules  $V^{(i)}$ . These representations are shown in Table 15 in Appendix B. The character table with all representations for  $G_{0,2}$  is as follows:

(31)

char/class	$K_1$	$K_2$	$K_3$	$K_4$	$K_5$
$\chi^{(1)}$	1	1	1	1	1
$\chi^{(2)}$	1	1	-1	1	-1
$\chi^{(3)}$	1	1	1	-1	-1
$\chi^{(4)}$	1	1	-1	-1	1
$\chi^{(5)}$	2	-2	0	0	0
$\chi^{(6)}$	2	-2	0	0	0

Note that since the characters of  $X^{(5)}$  and  $X^{(6)}$  are the same, these representations are equivalent. The character table without the last row again shows that the characters satisfy the two orthogonality relations.

### 3.3. Groups of order 16

In this section we discuss the vee groups  $G_{3,0}$ ,  $G_{2,1}$ ,  $G_{1,2}$  and  $G_{0,3}$ . Conjugacy classes of these groups are given in (21). Their character tables can be computed using a combination of Algorithm 1 and Algorithm 2, as required.

#### 3.3.1. The group $G_{3,0} = S_1$

The group  $G_{3,0}$  is generated by  $-1$ ,  $e_1$ ,  $e_2$  and  $e_3$  with  $e_1^2 = e_2^2 = e_3^2 = 1$ ,  $e_i e_j = -e_j e_i$ ,  $i \neq j$ , while the group  $S \subset S_{16}$  isomorphic to  $G_{3,0}$  and generated by corresponding permutations is shown in Table 8 in Appendix A.

In a manner similar to the groups of orders 4 and 8, one can find the decomposition of  $\mathbb{C}[G_{3,0}]$  into invariant subspaces

$$(32) \quad \mathbb{C}[G_{3,0}] = \bigoplus_{i=1}^{12} V^{(i)},$$

where  $V^{(i)} = \text{span}\{\mathbf{u}_i\}$ ,  $i = 1, \dots, 8$ , are one-dimensional while

$$(33) \quad \begin{aligned} V^{(9)} &= \text{span}\{\mathbf{u}_9, \mathbf{u}_{10}\}, & V^{(10)} &= \text{span}\{\mathbf{u}_{11}, \mathbf{u}_{12}\}, \\ V^{(11)} &= \text{span}\{\mathbf{u}_{13}, \mathbf{u}_{14}\}, & V^{(12)} &= \text{span}\{\mathbf{u}_{15}, \mathbf{u}_{16}\} \end{aligned}$$

are two-dimensional subspaces carrying two pairwise equivalent representations according to Proposition 4, Theorem 10 and Theorem 11.

The basis vectors  $\mathbf{u}_i$  are displayed in (47) in Appendix B. They have been found by using the above two algorithms.

Once the decomposition of  $\mathbb{C}[G_{3,0}]$  has been determined, one can compute all irreducible representations  $X^{(i)}$  of  $G_{3,0}$ . The representations are displayed in Table 16 in Appendix B. The extended character table for  $G_{3,0}$  is as follows:

char/class	$K_1$	$K_2$	$K_3$	$K_4$	$K_5$	$K_6$	$K_7$	$K_8$	$K_9$	$K_{10}$
$\chi^{(1)}$	1	1	1	1	1	1	1	1	1	1
$\chi^{(2)}$	1	1	-1	-1	1	1	-1	1	-1	-1
$\chi^{(3)}$	1	1	-1	-1	1	-1	1	-1	1	-1
$\chi^{(4)}$	1	1	1	1	1	-1	-1	-1	-1	1
$\chi^{(5)}$	1	1	-1	-1	-1	1	1	-1	-1	1
$\chi^{(6)}$	1	1	1	1	-1	1	-1	-1	1	-1
$\chi^{(7)}$	1	1	1	1	-1	-1	1	1	-1	-1
$\chi^{(8)}$	1	1	-1	-1	-1	-1	-1	1	1	1
$\chi^{(9)}$	2	-2	$2i$	$-2i$	0	0	0	0	0	0
$\chi^{(10)}$	2	-2	$-2i$	$2i$	0	0	0	0	0	0
$\chi^{(11)}$	2	-2	$-2i$	$2i$	0	0	0	0	0	0
$\chi^{(12)}$	2	-2	$2i$	$-2i$	0	0	0	0	0	0

Note that  $X^{(9)} \cong X^{(12)}$  and  $X^{(9)} \cong X^{(12)}$  since their characters are the same. To illustrate orthogonality of the characters, consider the inner product of the characters  $\chi^{(2)}$  and  $\chi^{(3)}$ :

$$\begin{aligned}
 \langle \chi^{(2)}, \chi^{(3)} \rangle &= \frac{1}{16} \sum_{i=1}^{10} |K_i| \chi_{K_i}^{(2)} \overline{\chi_{K_i}^{(3)}} \\
 &= \frac{1}{16} (1 \cdot (1)(1) + 1 \cdot (1)(1) + 1 \cdot (-1)(-1) + 1 \cdot (-1)(-1) \\
 &\quad + 2 \cdot (1)(1) + 2 \cdot (1)(-1) + 2 \cdot (-1)(1) \\
 &\quad + 2 \cdot (1)(-1) + 2 \cdot (-1)(1) + 2 \cdot (-1)(-1)) \\
 &= 0.
 \end{aligned}
 \tag{35}$$

which verifies the character orthogonality relation of the first kind. In a similar manner one can verify the character relation of the second kind.

Since the group  $G_{1,2}$  belongs to the same class  $S_1$  as  $G_{3,0}$ , it will not be discussed separately.

### 3.3.2. The group $G_{2,1} = \Omega_1$

The group  $G_{2,1}$  is generated by  $-1$ ,  $e_1$ ,  $e_2$  and  $e_3$  with  $e_1^2 = e_2^2 = 1$  and  $e_3^2 = -1$ ,  $e_i e_j = -e_j e_i$ ,  $i \neq j$ , while the group  $S \subset S_{16}$  isomorphic to  $G_{2,1}$  is generated by the permutations of  $S_{16}$  as shown in Table 9 in Appendix A.

The decomposition of  $\mathbb{C}[G_{2,1}]$  looks the same as that of  $\mathbb{C}[G_{3,0}]$  displayed in (32), while the basis vectors  $\mathbf{u}_i$  for this decomposition are displayed in (49) in Appendix B. They have been found by using the above two algorithms.

Once the decomposition of  $\mathbb{C}[G_{2,1}]$  has been found, one can compute all irreducible representations  $X^{(i)}$  of  $G_{2,1}$ . The representations are displayed in Table 17 in Appendix B. The extended character table for  $G_{2,1}$  is as follows:

char/class	$K_1$	$K_2$	$K_3$	$K_4$	$K_5$	$K_6$	$K_7$	$K_8$	$K_9$	$K_{10}$
$\chi^{(1)}$	1	1	1	1	1	1	1	1	1	1
$\chi^{(2)}$	1	1	-1	-1	1	1	-1	1	-1	-1
$\chi^{(3)}$	1	1	-1	-1	1	-1	1	-1	1	-1
$\chi^{(4)}$	1	1	1	1	1	-1	-1	-1	-1	1
$\chi^{(5)}$	1	1	-1	-1	-1	1	1	-1	-1	1
$\chi^{(6)}$	1	1	1	1	-1	1	-1	-1	1	-1
$\chi^{(7)}$	1	1	1	1	-1	-1	1	1	-1	-1
$\chi^{(8)}$	1	1	-1	-1	-1	-1	-1	1	1	1
$\chi^{(9)}$	2	-2	-2	2	0	0	0	0	0	0
$\chi^{(10)}$	2	-2	2	-2	0	0	0	0	0	0
$\chi^{(11)}$	2	-2	-2	2	0	0	0	0	0	0
$\chi^{(12)}$	2	-2	2	-2	0	0	0	0	0	0

Note that  $X^{(9)} \cong X^{(11)}$  and  $X^{(10)} \cong X^{(12)}$  since their characters are the same.

### 3.3.3. The group $G_{0,3} = \Omega_2$

The group  $G_{0,3}$  is generated by  $-1$ ,  $e_1$ ,  $e_2$  and  $e_3$  with  $e_1^2 = e_2^2 = e_3^2 = -1$ ,  $e_i e_j = -e_j e_i$ ,  $i \neq j$ , while the group  $S \subset S_{16}$  isomorphic to  $G_{0,3}$  is generated by the corresponding permutations of  $S_{16}$  shown in Table 11 in Appendix A.

The decomposition of  $\mathbb{C}[G_{0,3}]$  again looks the same as that of  $\mathbb{C}[G_{3,0}]$  in (32), while the basis vectors  $\mathbf{u}_i$  are displayed in (51) in Appendix B. They have been found by using the above two algorithms. The irreducible representations  $X^{(i)}$  of  $G_{0,3}$  have been computed in the same manner. They are displayed in Table 17 in Appendix B. The extended character table for  $G_{0,3}$  is as follows:

char/class	$K_1$	$K_2$	$K_3$	$K_4$	$K_5$	$K_6$	$K_7$	$K_8$	$K_9$	$K_{10}$
$\chi^{(1)}$	1	1	1	1	1	1	1	1	1	1
$\chi^{(2)}$	1	1	-1	-1	1	1	-1	1	-1	-1
$\chi^{(3)}$	1	1	-1	-1	1	-1	1	-1	1	-1
$\chi^{(4)}$	1	1	1	1	1	-1	-1	-1	-1	1
$\chi^{(5)}$	1	1	-1	-1	-1	1	1	-1	-1	1
$\chi^{(6)}$	1	1	1	1	-1	1	-1	-1	1	-1
$\chi^{(7)}$	1	1	1	1	-1	-1	1	1	-1	-1
$\chi^{(8)}$	1	1	-1	-1	-1	-1	-1	1	1	1
$\chi^{(9)}$	2	-2	-2	2	0	0	0	0	0	0
$\chi^{(10)}$	2	-2	2	-2	0	0	0	0	0	0
$\chi^{(11)}$	2	-2	-2	2	0	0	0	0	0	0
$\chi^{(12)}$	2	-2	2	-2	0	0	0	0	0	0

Note that  $X^{(9)} \cong X^{(11)}$  and  $X^{(10)} \cong X^{(12)}$  since their characters are the same.

## 4. Conclusions

Due to the renewed interest in the relationship between finite Salingaros' vee groups  $G = G_{p,q}$  and Clifford algebras, the main goal of this paper has been to show how one can construct irreducible representations of these groups by decomposing their regular modules. In the process, two algorithms have been formulated which have allowed us to completely decompose regular modules of groups of orders 4, 8, and 16 into irreducible  $G$ -submodules. These algorithms have used Groebner basis approach to find bases in these  $G$ -submodules as well as the  $G$ -invariance of an inner product defined on the complex regular module  $\mathbb{C}G$ . In the process, we have computed character tables of these groups. Of course, the character tables of these groups are known and can be found in the literature, e.g., see [12] and references therein. It is much more efficient to derive the character tables using the character theory instead of finding the actual representations first. Furthermore, knowing the irreducible characters of a finite group  $G$ , one can use them to decompose any  $G$ -module, let it be regular or, for example, a permutation module, into a direct sum of  $G$ -submodules without a common composition factor. This approach is based on defining, for each irreducible character  $\chi_i$  of  $G$  an idempotent element  $e_i$  in the group algebra  $\mathbb{C}G$  such that these (not necessarily primitive) idempotents provide an orthogonal decomposition of the unity in  $\mathbb{C}G$ . This way, for example, the regular module  $\mathbb{C}G$  can be decomposed into a direct sum of two sided ideals  $\mathbb{C}Ge_i$  generated by the idempotents. These ideals as  $G$ -submodules, do not share a common composition factor and are reducible if the degree of  $\chi_i$  is greater than 1. [12] Then, to achieve a complete decomposition, these reducible  $G$ -modules can be further decomposed by an algorithm similar to the Algorithm 2. The two algorithms can be applied to groups of higher order than 16, if needed.

### A. Images of the generators of the vee groups

In this Appendix, we show images of the generators of the vee groups  $G_{p,q}$  for  $p + q \leq 3$  in the symmetric groups  $S_n$  where  $n = 2^{1+p+q}$ .

Tab. 5: Generators for  $G_{1,0}$  and  $G_{0,1}$  in  $S_4$ .

	$G_{1,0}$	Order	$G_{0,1}$	Order
$-1$	$(1, 2)(3, 4)$	2	$(1, 2)(3, 4)$	2
$e_1$	$(1, 3)(2, 4)$	2	$(1, 3, 2, 4)$	4

### B. Irreducible representations of the vee groups

In this Appendix, we show matrices for one representative  $g$  from each conjugacy class  $K_i$  in each irreducible representation  $X^{(j)}$  for all vee groups of orders 4, 8, and 16. Here, the index  $i$  runs through all conjugacy classes whereas the index  $j$  runs through all irreducible representations including equivalent ones.

Tab. 6: Generators for  $G_{2,0}$  and  $G_{1,1}$  in  $S_8$ .

	$G_{2,0}$	Order	$G_{1,1}$	Order
$-1$	$(1, 2)(3, 4)(5, 6)(7, 8)$	2	$(1, 2)(3, 4)(5, 6)(7, 8)$	2
$e_1$	$(1, 3)(2, 4)(5, 7)(6, 8)$	2	$(1, 3)(2, 4)(5, 7)(6, 8)$	2
$e_2$	$(1, 5)(2, 6)(3, 8)(4, 7)$	2	$(1, 5, 2, 6)(3, 8, 4, 7)$	4

Tab. 7: Generators for  $G_{0,2}$  in  $S_8$ .

	$G_{0,2}$	Order
$-1$	$(1, 2)(3, 4)(5, 6)(7, 8)$	2
$e_1$	$(1, 3, 2, 4)(5, 7, 6, 8)$	4
$e_2$	$(1, 5, 2, 6)(3, 8, 4, 7)$	4

Tab. 8: Generators for  $G_{3,0}$  in  $S_{16}$ .

	$G_{3,0}$	Order
$-1$	$(1, 2)(3, 4)(5, 6)(7, 8)(9, 10)(11, 12)(13, 14)(15, 16)$	2
$e_1$	$(1, 3)(2, 4)(5, 9)(6, 10)(7, 11)(8, 12)(13, 15)(14, 16)$	2
$e_2$	$(1, 5)(2, 6)(3, 10)(4, 9)(7, 13)(8, 14)(11, 16)(12, 15)$	2
$e_3$	$(1, 7)(2, 8)(3, 12)(4, 11)(5, 14)(6, 13)(9, 15)(10, 16)$	2

For consistency, matrices shown in the tables below always represent the first element in each class. For the groups of order 4, all representations are inequivalent, and are shown in Tables 12 and 13.

In Table 12, the irreducible representations  $X^{(i)}$  of  $G_{1,0}$  are realized in irreducible  $G_{1,0}$ -invariant submodules of the group algebra  $\mathbb{C}[G_{1,0}]$  which is decomposed as follows:

$$(38) \quad \mathbb{C}[G_{1,0}] = V^{(1)} \oplus V^{(2)} \oplus V^{(3)} \oplus V^{(4)}.$$

The one-dimensional submodules  $V^{(i)}$  are spanned by the corresponding vectors  $\mathbf{u}_i$ ,  $i = 1, \dots, 4$ . The coordinates of these vectors in the basis  $\mathcal{B} = \{1, -1, e_1, -e_1\}$  are as follows:

$$(39) \quad \begin{aligned} V^{(1)} &= \text{span}\{\mathbf{u}_1\}, & \mathbf{u}_1 &= (1, 1, 1, 1), \\ V^{(2)} &= \text{span}\{\mathbf{u}_2\}, & \mathbf{u}_2 &= (1, -1, -1, 1), \\ V^{(3)} &= \text{span}\{\mathbf{u}_3\}, & \mathbf{u}_3 &= (-1, 1, -1, 1), \\ V^{(4)} &= \text{span}\{\mathbf{u}_4\}, & \mathbf{u}_4 &= (-1, -1, 1, 1). \end{aligned}$$

In Table 13, the irreducible representations  $X^{(i)}$  of  $G_{0,1}$  are realized in irreducible  $G_{0,1}$ -invariant submodules of the group algebra  $\mathbb{C}[G_{0,1}]$  which is decomposed as follows:

Tab. 9: Generators for  $G_{2,1}$  in  $S_{16}$ .

	$G_{2,1}$	Order
$-1$	$(1, 2)(3, 4)(5, 6)(7, 8)(9, 10)(11, 12)(13, 14)(15, 16)$	2
$e_1$	$(1, 3)(2, 4)(5, 9)(6, 10)(7, 11)(8, 12)(13, 15)(14, 16)$	2
$e_2$	$(1, 5)(2, 6)(3, 10)(4, 9)(7, 13)(8, 14)(11, 16)(12, 15)$	2
$e_3$	$(1, 7, 2, 8)(3, 12, 4, 11)(5, 14, 6, 13)(9, 15, 10, 16)$	4

Tab. 10: Generators for  $G_{1,2}$  in  $S_{16}$ .

	$G_{1,2}$	Order
$-1$	$(1, 2)(3, 4)(5, 6)(7, 8)(9, 10)(11, 12)(13, 14)(15, 16)$	2
$e_1$	$(1, 3)(2, 4)(5, 9)(6, 10)(7, 11)(8, 12)(13, 15)(14, 16)$	2
$e_2$	$(1, 5, 2, 6)(3, 10, 4, 9)(7, 13, 8, 14)(11, 16, 12, 15)$	4
$e_3$	$(1, 7, 2, 8)(3, 12, 4, 11)(5, 14, 6, 13)(9, 15, 10, 16)$	4

Tab. 11: Generators for  $G_{0,3}$  in  $S_{16}$ .

	$G_{0,3}$	Order
$-1$	$(1, 2)(3, 4)(5, 6)(7, 8)(9, 10)(11, 12)(13, 14)(15, 16)$	2
$e_1$	$(1, 3, 2, 4)(5, 9, 6, 10)(7, 11, 8, 12)(13, 15, 14, 16)$	4
$e_2$	$(1, 5, 2, 6)(3, 10, 4, 9)(7, 13, 8, 14)(11, 16, 12, 15)$	4
$e_3$	$(1, 7, 2, 8)(3, 12, 4, 11)(5, 14, 6, 13)(9, 15, 10, 16)$	4

$$(40) \quad \mathbb{C}[G_{0,1}] = V^{(1)} \oplus V^{(2)} \oplus V^{(3)} \oplus V^{(4)}.$$

The one-dimensional submodules  $V^{(i)}$  are spanned by the corresponding vectors  $\mathbf{u}_i$ ,  $i = 1, \dots, 4$ . The complex-valued coordinates of these vectors in the basis  $\mathcal{B} = \{1, -1, e_1, -e_1\}$  are as follows:

$$(41) \quad \begin{aligned} V^{(1)} &= \text{span}\{\mathbf{u}_1\}, & \mathbf{u}_1 &= (1, 1, 1, 1), \\ V^{(2)} &= \text{span}\{\mathbf{u}_2\}, & \mathbf{u}_2 &= (i, -i, -1, 1), \\ V^{(3)} &= \text{span}\{\mathbf{u}_3\}, & \mathbf{u}_3 &= (-1, -1, 1, -1), \\ V^{(4)} &= \text{span}\{\mathbf{u}_4\}, & \mathbf{u}_4 &= (i, -i, -1, 1). \end{aligned}$$

In Table 14, the irreducible representations  $X^{(i)}$  of  $G_{2,0} = D_8 = N_1$  are realized in irreducible  $G_{2,0}$ -invariant submodules of the group algebra  $\mathbb{C}[G_{2,0}]$  which is decomposed as follows:

$$(42) \quad \mathbb{C}[G_{2,0}] = V^{(1)} \oplus V^{(2)} \oplus V^{(3)} \oplus V^{(4)} \oplus V^{(5)} \oplus V^{(6)}.$$

The submodules  $V^{(i)}$  are spanned by the corresponding vectors  $\mathbf{u}_i$ ,  $i = 1, \dots, 8$ , as shown below. The coordinates of these vectors in the standard basis



Tab. 12: Representations of  $G_{1,0} = D_4$ .

	$K_1$	$K_2$	$K_3$	$K_4$
$g$	1	-1	$e_1$	$-e_1$
$X^{(1)}$	(1)	(1)	(1)	(1)
$X^{(2)}$	(1)	(-1)	(-1)	(1)
$X^{(3)}$	(1)	(-1)	(1)	(-1)
$X^{(4)}$	(1)	(1)	(-1)	(-1)

Tab. 13: Representations of  $G_{0,1} = \mathbb{Z}_4$ .

	$K_1$	$K_2$	$K_3$	$K_4$
$g$	1	-1	$e_1$	$-e_1$
$X^{(1)}$	(1)	(1)	(1)	(1)
$X^{(2)}$	(1)	(-1)	( $i$ )	( $-i$ )
$X^{(3)}$	(1)	(1)	(-1)	(-1)
$X^{(4)}$	(1)	(-1)	( $-i$ )	( $i$ )

$$\mathcal{B} = \{1, -1, e_1, -e_1, e_2, -e_2, e_{12}, -e_{12}\}$$

are as follows:

$$\begin{aligned}
V^{(1)} &= \text{span}\{\mathbf{u}_1\}, & \mathbf{u}_1 &= (1, 1, 1, 1, 1, 1, 1, 1), \\
V^{(2)} &= \text{span}\{\mathbf{u}_2\}, & \mathbf{u}_2 &= (-1, -1, 1, 1, 1, 1, -1, -1), \\
V^{(3)} &= \text{span}\{\mathbf{u}_3\}, & \mathbf{u}_3 &= (-1, -1, -1, -1, 1, 1, 1, 1), \\
V^{(4)} &= \text{span}\{\mathbf{u}_4\}, & \mathbf{u}_4 &= (1, 1, -1, -1, 1, 1, -1, -1), \\
V^{(5)} &= \text{span}\{\mathbf{u}_5, \mathbf{u}_6\}, & \mathbf{u}_5 &= (-1, 1, -1, 1, -1, 1, 1, -1), \\
& & \mathbf{u}_6 &= (-5, 5, -5, 5, -1, 1, 1, -1), \\
V^{(6)} &= \text{span}\{\mathbf{u}_7, \mathbf{u}_8\}, & \mathbf{u}_7 &= (1, -1, -1, 1, 0, 0, 0, 0), \\
& & \mathbf{u}_8 &= (1, -1, -1, 1, -1, 1, -1, 1).
\end{aligned}
\tag{43}$$

While the one-dimensional representations  $X^{(1)}, X^{(2)}, X^{(3)}, X^{(4)}$  are inequivalent, the two-dimensional representations  $X^{(5)}$  and  $X^{(6)}$  are equivalent.

In Table 15, the irreducible representations  $X^{(i)}$  of  $G_{0,2} = Q_8 = N_2$  are realized in irreducible  $G_{0,2}$ -invariant submodules of the group algebra  $\mathbb{C}[G_{0,2}]$  which is decomposed as follows:

$$(44) \quad \mathbb{C}[G_{0,2}] = V^{(1)} \oplus V^{(2)} \oplus V^{(3)} \oplus V^{(4)} \oplus V^{(5)} \oplus V^{(6)}.$$

The submodules  $V^{(i)}$  are spanned by the corresponding vectors  $\mathbf{u}_i$ ,  $i = 1, \dots, 8$ , as shown below. The coordinates of these vectors in the standard basis

$$\mathcal{B} = \{1, -1, e_1, -e_1, e_2, -e_2, e_{12}, -e_{12}\}$$

Tab. 14: Representations of  $G_{2,0} = D_4 = N_1$ .

	$K_1$	$K_2$	$K_3$	$K_4$	$K_5$
$g$	1	-1	$e_1$	$e_2$	$e_{12}$
$X^{(1)}$	(1)	(1)	(1)	(1)	(1)
$X^{(2)}$	(1)	(1)	(-1)	(-1)	(1)
$X^{(3)}$	(1)	(1)	(1)	(-1)	(-1)
$X^{(4)}$	(1)	(1)	(-1)	(1)	(-1)
$X^{(5)}$	$\begin{pmatrix} 1 & 0 \\ 0 & 1 \end{pmatrix}$	$\begin{pmatrix} -1 & 0 \\ 0 & -1 \end{pmatrix}$	$\begin{pmatrix} -\frac{3}{2} & -\frac{5}{2} \\ \frac{1}{2} & \frac{3}{2} \end{pmatrix}$	$\begin{pmatrix} 1 & 6 \\ 0 & -1 \end{pmatrix}$	$\begin{pmatrix} -\frac{3}{2} & -\frac{13}{2} \\ \frac{1}{2} & \frac{3}{2} \end{pmatrix}$
$X^{(6)}$	$\begin{pmatrix} 1 & 0 \\ 0 & 1 \end{pmatrix}$	$\begin{pmatrix} -1 & 0 \\ 0 & -1 \end{pmatrix}$	$\begin{pmatrix} -1 & -2 \\ 0 & 1 \end{pmatrix}$	$\begin{pmatrix} 1 & 0 \\ -1 & -1 \end{pmatrix}$	$\begin{pmatrix} 1 & 2 \\ -1 & -1 \end{pmatrix}$

are as follows:

$$\begin{aligned}
V^{(1)} &= \text{span}\{\mathbf{u}_1\}, & \mathbf{u}_1 &= (1, 1, 1, 1, 1, 1, 1, 1), \\
V^{(2)} &= \text{span}\{\mathbf{u}_2\}, & \mathbf{u}_2 &= (-1, -1, 1, 1, -1, -1, 1, 1), \\
V^{(3)} &= \text{span}\{\mathbf{u}_3\}, & \mathbf{u}_3 &= (-1, -1, -1, -1, 1, 1, 1, 1), \\
V^{(4)} &= \text{span}\{\mathbf{u}_4\}, & \mathbf{u}_4 &= (1, 1, -1, -1, -1, -1, 1, 1), \\
V^{(5)} &= \text{span}\{\mathbf{u}_5, \mathbf{u}_6\}, & \mathbf{u}_5 &= (0, 0, 0, 0, -i, i, 1, -1), \\
& & \mathbf{u}_6 &= (-i, i, -1, 1, -i, i, 1, -1), \\
V^{(6)} &= \text{span}\{\mathbf{u}_7, \mathbf{u}_8\}, & \mathbf{u}_7 &= (1, -1, i, -i, 0, 0, 0, 0), \\
(45) \quad & & \mathbf{u}_8 &= (0, 0, 0, 0, 1, -1, -i, i).
\end{aligned}$$

While the one-dimensional representations  $X^{(1)}, X^{(2)}, X^{(3)}, X^{(4)}$  are inequivalent, the two-dimensional representations  $X^{(5)}$  and  $X^{(6)}$  are equivalent.

Tab. 15: Representations of  $G_{0,2} = Q_8 = N_2$ .

	$K_1$	$K_2$	$K_3$	$K_4$	$K_5$
$g$	1	-1	$e_1$	$e_2$	$e_{12}$
$X^{(1)}$	(1)	(1)	(1)	(1)	(1)
$X^{(2)}$	(1)	(1)	(-1)	(1)	(-1)
$X^{(3)}$	(1)	(1)	(1)	(-1)	(-1)
$X^{(4)}$	(1)	(1)	(-1)	(-1)	(1)
$X^{(5)}$	$\begin{pmatrix} 1 & 0 \\ 0 & 1 \end{pmatrix}$	$\begin{pmatrix} -1 & 0 \\ 0 & -1 \end{pmatrix}$	$\begin{pmatrix} -i & -2i \\ 0 & i \end{pmatrix}$	$\begin{pmatrix} 1 & 2 \\ -1 & -1 \end{pmatrix}$	$\begin{pmatrix} i & 0 \\ -i & -i \end{pmatrix}$
$X^{(6)}$	$\begin{pmatrix} 1 & 0 \\ 0 & 1 \end{pmatrix}$	$\begin{pmatrix} -1 & 0 \\ 0 & -1 \end{pmatrix}$	$\begin{pmatrix} -i & 0 \\ 0 & i \end{pmatrix}$	$\begin{pmatrix} 0 & -1 \\ 1 & 0 \end{pmatrix}$	$\begin{pmatrix} 0 & i \\ i & 0 \end{pmatrix}$

In Table 16, the irreducible representations  $X^{(i)}$  of  $G_{3,0} = S_1$  are realized in irreducible  $G_{3,0}$ -invariant submodules of the group algebra  $\mathbb{C}[G_{3,0}]$  which is decomposed as follows:

Tab. 16: Part 1: Representations of  $G_{3,0} = S_1$  for  $K_i$ ,  $i = 1, \dots, 5$ .

	$K_1$	$K_2$	$K_3$	$K_4$	$K_5$
$g$	1	-1	$e_{123}$	$-e_{123}$	$e_1$
$X^{(1)}$	(1)	(1)	(1)	(1)	(1)
$X^{(2)}$	(1)	(1)	(-1)	(-1)	(1)
$X^{(3)}$	(1)	(1)	(-1)	(-1)	(1)
$X^{(4)}$	(1)	(1)	(1)	(1)	(1)
$X^{(5)}$	(1)	(1)	(-1)	(-1)	(-1)
$X^{(6)}$	(1)	(1)	(1)	(1)	(-1)
$X^{(7)}$	(1)	(1)	(1)	(1)	(-1)
$X^{(8)}$	(1)	(1)	(-1)	(-1)	(-1)
$X^{(9)}$	$\begin{pmatrix} 1 & 0 \\ 0 & 1 \end{pmatrix}$	$\begin{pmatrix} -1 & 0 \\ 0 & -1 \end{pmatrix}$	$\begin{pmatrix} i & 0 \\ 0 & i \end{pmatrix}$	$\begin{pmatrix} -i & 0 \\ 0 & -i \end{pmatrix}$	$\begin{pmatrix} 0 & 1 \\ 1 & 0 \end{pmatrix}$
$X^{(10)}$	$\begin{pmatrix} 1 & 0 \\ 1 & 0 \end{pmatrix}$	$\begin{pmatrix} -1 & 0 \\ 0 & -1 \end{pmatrix}$	$\begin{pmatrix} -i & 0 \\ 0 & -i \end{pmatrix}$	$\begin{pmatrix} i & 0 \\ 0 & i \end{pmatrix}$	$\begin{pmatrix} 1 & 0 \\ 0 & -1 \end{pmatrix}$
$X^{(11)}$	$\begin{pmatrix} 1 & 0 \\ 0 & 1 \end{pmatrix}$	$\begin{pmatrix} -1 & 0 \\ 0 & -1 \end{pmatrix}$	$\begin{pmatrix} -i & 0 \\ 0 & -i \end{pmatrix}$	$\begin{pmatrix} i & 0 \\ 0 & i \end{pmatrix}$	$\begin{pmatrix} -1 & 0 \\ 0 & 1 \end{pmatrix}$
$X^{(12)}$	$\begin{pmatrix} 1 & 0 \\ 0 & 1 \end{pmatrix}$	$\begin{pmatrix} -1 & 0 \\ 0 & -1 \end{pmatrix}$	$\begin{pmatrix} i & 0 \\ 0 & i \end{pmatrix}$	$\begin{pmatrix} -i & 0 \\ 0 & -i \end{pmatrix}$	$\begin{pmatrix} 0 & 1 \\ 1 & 0 \end{pmatrix}$

Tab. 16: Part 2: Representations of  $G_{3,0} = S_1$  for  $K_i$ ,  $i = 6, \dots, 10$ .

	$K_6$	$K_7$	$K_8$	$K_9$	$K_{10}$
$g$	$e_2$	$e_3$	$e_{12}$	$e_{13}$	$e_{23}$
$X^{(1)}$	(1)	(1)	(1)	(1)	(1)
$X^{(2)}$	(1)	(-1)	(1)	(-1)	(-1)
$X^{(3)}$	(-1)	(1)	(-1)	(1)	(-1)
$X^{(4)}$	(-1)	(-1)	(-1)	(-1)	(1)
$X^{(5)}$	(1)	(1)	(-1)	(-1)	(1)
$X^{(6)}$	(1)	(-1)	(-1)	(1)	(-1)
$X^{(7)}$	(-1)	(1)	(1)	(-1)	(-1)
$X^{(8)}$	(-1)	(-1)	(1)	(1)	(1)
$X^{(9)}$	$\begin{pmatrix} 0 & -i \\ i & 0 \end{pmatrix}$	$\begin{pmatrix} 1 & 0 \\ 0 & -1 \end{pmatrix}$	$\begin{pmatrix} i & 0 \\ 0 & -i \end{pmatrix}$	$\begin{pmatrix} 0 & -1 \\ 1 & 0 \end{pmatrix}$	$\begin{pmatrix} 0 & i \\ i & 0 \end{pmatrix}$
$X^{(10)}$	$\begin{pmatrix} 0 & -1 \\ -1 & 0 \end{pmatrix}$	$\begin{pmatrix} 0 & -i \\ i & 0 \end{pmatrix}$	$\begin{pmatrix} 0 & -1 \\ 1 & 0 \end{pmatrix}$	$\begin{pmatrix} 0 & -i \\ -i & 0 \end{pmatrix}$	$\begin{pmatrix} -i & 0 \\ 0 & i \end{pmatrix}$
$X^{(11)}$	$\begin{pmatrix} 0 & -1 \\ -1 & 0 \end{pmatrix}$	$\begin{pmatrix} 0 & i \\ -i & 0 \end{pmatrix}$	$\begin{pmatrix} 0 & 1 \\ -1 & 0 \end{pmatrix}$	$\begin{pmatrix} 0 & -i \\ -i & 0 \end{pmatrix}$	$\begin{pmatrix} i & 0 \\ 0 & -i \end{pmatrix}$
$X^{(12)}$	$\begin{pmatrix} 0 & -i \\ i & 0 \end{pmatrix}$	$\begin{pmatrix} 1 & 0 \\ 0 & -1 \end{pmatrix}$	$\begin{pmatrix} i & 0 \\ 0 & -i \end{pmatrix}$	$\begin{pmatrix} 0 & -1 \\ 1 & 0 \end{pmatrix}$	$\begin{pmatrix} 0 & i \\ i & 0 \end{pmatrix}$

$$(46) \quad \mathbb{C}[G_{3,0}] = \bigoplus_{i=1}^{12} V^{(i)}.$$

The submodules  $V^{(i)}$  are spanned by the corresponding vectors  $\mathbf{u}_i$ ,  $i = 1, \dots, 16$ , as shown below. The coordinates of these vectors in the standard basis

$$\mathcal{B} = \{1, -1, e_1, -e_1, e_2, -e_2, e_3, -e_3, e_{12}, -e_{12}, e_{13}, -e_{13}, e_{23}, -e_{23}, e_{123}, -e_{123}\}$$

are as follows:

$$\begin{aligned}
V^{(1)} &= \text{span}\{\mathbf{u}_1\}, & \mathbf{u}_1 &= (1, 1, 1, 1, 1, 1, 1, 1, 1, 1, 1, 1, 1, 1, 1, 1), \\
V^{(2)} &= \text{span}\{\mathbf{u}_2\}, & \mathbf{u}_2 &= (-1, -1, -1, -1, -1, -1, 1, 1, -1, -1, 1, 1, 1, 1, 1, 1), \\
V^{(3)} &= \text{span}\{\mathbf{u}_3\}, & \mathbf{u}_3 &= (-1, -1, -1, -1, 1, 1, -1, -1, 1, 1, -1, -1, 1, 1, 1, 1), \\
V^{(4)} &= \text{span}\{\mathbf{u}_4\}, & \mathbf{u}_4 &= (1, 1, 1, 1, -1, -1, -1, -1, -1, -1, -1, -1, 1, 1, 1, 1), \\
V^{(5)} &= \text{span}\{\mathbf{u}_5\}, & \mathbf{u}_5 &= (-1, -1, 1, 1, -1, -1, -1, -1, 1, 1, 1, 1, -1, -1, 1, 1), \\
V^{(6)} &= \text{span}\{\mathbf{u}_6\}, & \mathbf{u}_6 &= (1, 1, -1, -1, 1, 1, -1, -1, -1, -1, 1, 1, -1, -1, 1, 1), \\
V^{(7)} &= \text{span}\{\mathbf{u}_7\}, & \mathbf{u}_7 &= (1, 1, -1, -1, -1, -1, 1, 1, 1, 1, -1, -1, -1, -1, 1, 1), \\
V^{(8)} &= \text{span}\{\mathbf{u}_8\}, & \mathbf{u}_8 &= (-1, -1, 1, 1, 1, 1, 1, 1, -1, -1, -1, -1, -1, -1, 1, 1), \\
V^{(9)} &= \text{span}\{\mathbf{u}_9, \mathbf{u}_{10}\}, & \mathbf{u}_9 &= (-i, i, 0, 0, 0, 0, -i, i, -1, 1, 0, 0, 0, 0, -1, 1), \\
& & \mathbf{u}_{10} &= (0, 0, -i, i, -1, 1, 0, 0, 0, 0, -i, i, -1, 1, 0, 0), \\
V^{(10)} &= \text{span}\{\mathbf{u}_{11}, \mathbf{u}_{12}\}, & \mathbf{u}_{11} &= (0, 0, 0, 0, -i, i, -1, 1, -i, i, -1, 1, 0, 0, 0, 0), \\
& & \mathbf{u}_{12} &= (i, -i, -i, i, 0, 0, 0, 0, 0, 0, 0, 0, 1, -1, -1, 1), \\
V^{(11)} &= \text{span}\{\mathbf{u}_{13}, \mathbf{u}_{14}\}, & \mathbf{u}_{13} &= (0, 0, 0, 0, -i, i, 1, -1, i, -i, -1, 1, 0, 0, 0, 0), \\
& & \mathbf{u}_{14} &= (i, -i, i, -i, 0, 0, 0, 0, 0, 0, 0, 0, -1, 1, -1, 1), \\
V^{(12)} &= \text{span}\{\mathbf{u}_{15}, \mathbf{u}_{16}\}, & \mathbf{u}_{15} &= (0, 0, -i, i, 1, -1, 0, 0, 0, 0, i, -i, -1, 1, 0, 0), \\
(47) \quad & & \mathbf{u}_{16} &= (-i, i, 0, 0, 0, 0, i, -i, 1, -1, 0, 0, 0, 0, -1, 1).
\end{aligned}$$

While the representations  $X^{(i)}$ ,  $i = 1, \dots, 10$ , are all inequivalent and irreducible, the remaining two-dimensional irreducible representations are equivalent as follows:  $X^{(12)} \cong X^{(9)}$  and  $X^{(11)} \cong X^{(10)}$ .

In Table 17, the irreducible representations  $X^{(i)}$  of  $G_{2,1} = \Omega_1$  are realized in irreducible  $G_{2,1}$ -invariant submodules of the group algebra  $\mathbb{C}[G_{2,1}]$  which is decomposed as follows:

$$(48) \quad \mathbb{C}[G_{2,1}] = \bigoplus_{i=1}^{12} V^{(i)}.$$

The submodules  $V^{(i)}$  are spanned by the corresponding vectors  $\mathbf{u}_i$ ,  $i = 1, \dots, 16$ , as shown below. The coordinates of these vectors in the standard basis

Tab. 17: Part 1: Representations of  $G_{2,1} = \Omega_1$  for  $K_i$ ,  $i = 1, \dots, 5$ .

	$K_1$	$K_2$	$K_3$	$K_4$	$K_5$
$g$	1	-1	$e_{123}$	$-e_{123}$	$e_1$
$X^{(1)}$	(1)	(1)	(1)	(1)	(1)
$X^{(2)}$	(1)	(1)	(-1)	(-1)	(1)
$X^{(3)}$	(1)	(1)	(-1)	(-1)	(1)
$X^{(4)}$	(1)	(1)	(1)	(1)	(1)
$X^{(5)}$	(1)	(1)	(-1)	(-1)	(-1)
$X^{(6)}$	(1)	(1)	(1)	(1)	(-1)
$X^{(7)}$	(1)	(1)	(1)	(1)	(-1)
$X^{(8)}$	(1)	(1)	(-1)	(-1)	(-1)
$X^{(9)}$	$\begin{pmatrix} 1 & 0 \\ 0 & 1 \end{pmatrix}$	$\begin{pmatrix} -1 & 0 \\ 0 & -1 \end{pmatrix}$	$\begin{pmatrix} -1 & 0 \\ 0 & -1 \end{pmatrix}$	$\begin{pmatrix} 1 & 0 \\ 0 & 1 \end{pmatrix}$	$\begin{pmatrix} 1 & 0 \\ 0 & -1 \end{pmatrix}$
$X^{(10)}$	$\begin{pmatrix} 1 & 0 \\ 0 & 1 \end{pmatrix}$	$\begin{pmatrix} -1 & 0 \\ 0 & -1 \end{pmatrix}$	$\begin{pmatrix} 1 & 0 \\ 0 & 1 \end{pmatrix}$	$\begin{pmatrix} -1 & 0 \\ 0 & -1 \end{pmatrix}$	$\begin{pmatrix} -1 & 0 \\ 0 & 1 \end{pmatrix}$
$X^{(11)}$	$\begin{pmatrix} 1 & 0 \\ 0 & 1 \end{pmatrix}$	$\begin{pmatrix} -1 & 0 \\ 0 & -1 \end{pmatrix}$	$\begin{pmatrix} -1 & 0 \\ 0 & -1 \end{pmatrix}$	$\begin{pmatrix} 1 & 0 \\ 0 & 1 \end{pmatrix}$	$\begin{pmatrix} 1 & 0 \\ 0 & -1 \end{pmatrix}$
$X^{(12)}$	$\begin{pmatrix} 1 & 0 \\ 0 & 1 \end{pmatrix}$	$\begin{pmatrix} -1 & 0 \\ 0 & -1 \end{pmatrix}$	$\begin{pmatrix} 1 & 0 \\ 0 & 1 \end{pmatrix}$	$\begin{pmatrix} -1 & 0 \\ 0 & -1 \end{pmatrix}$	$\begin{pmatrix} 1 & 0 \\ 0 & -1 \end{pmatrix}$

Tab. 17: Part 2: Representations of  $G_{2,1} = \Omega_1$  for  $K_i$ ,  $i = 6, \dots, 10$ .

	$K_6$	$K_7$	$K_8$	$K_9$	$K_{10}$
$g$	$e_2$	$e_3$	$e_{12}$	$e_{13}$	$e_{23}$
$X^{(1)}$	(1)	(1)	(1)	(1)	(1)
$X^{(2)}$	(1)	(-1)	(1)	(-1)	(-1)
$X^{(3)}$	(-1)	(1)	(-1)	(1)	(-1)
$X^{(4)}$	(-1)	(-1)	(-1)	(-1)	(1)
$X^{(5)}$	(1)	(1)	(-1)	(-1)	(1)
$X^{(6)}$	(1)	(-1)	(-1)	(1)	(-1)
$X^{(7)}$	(-1)	(1)	(1)	(-1)	(-1)
$X^{(8)}$	(-1)	(-1)	(1)	(1)	(1)
$X^{(9)}$	$\begin{pmatrix} 0 & -1 \\ -1 & 0 \end{pmatrix}$	$\begin{pmatrix} 0 & -1 \\ 1 & 0 \end{pmatrix}$	$\begin{pmatrix} 0 & -1 \\ 1 & 0 \end{pmatrix}$	$\begin{pmatrix} 0 & -1 \\ -1 & 0 \end{pmatrix}$	$\begin{pmatrix} -1 & 0 \\ 0 & 1 \end{pmatrix}$
$X^{(10)}$	$\begin{pmatrix} 0 & -1 \\ -1 & 0 \end{pmatrix}$	$\begin{pmatrix} 0 & -1 \\ 1 & 0 \end{pmatrix}$	$\begin{pmatrix} 0 & 1 \\ -1 & 0 \end{pmatrix}$	$\begin{pmatrix} 0 & 1 \\ 1 & 0 \end{pmatrix}$	$\begin{pmatrix} -1 & 0 \\ 0 & 1 \end{pmatrix}$
$X^{(11)}$	$\begin{pmatrix} 0 & -1 \\ -1 & 0 \end{pmatrix}$	$\begin{pmatrix} 0 & -1 \\ 1 & 0 \end{pmatrix}$	$\begin{pmatrix} 0 & -1 \\ 1 & 0 \end{pmatrix}$	$\begin{pmatrix} 0 & -1 \\ -1 & 0 \end{pmatrix}$	$\begin{pmatrix} -1 & 0 \\ 0 & 1 \end{pmatrix}$
$X^{(12)}$	$\begin{pmatrix} 0 & -1 \\ -1 & 0 \end{pmatrix}$	$\begin{pmatrix} 0 & 1 \\ -1 & 0 \end{pmatrix}$	$\begin{pmatrix} 0 & -1 \\ 1 & 0 \end{pmatrix}$	$\begin{pmatrix} 0 & 1 \\ 1 & 0 \end{pmatrix}$	$\begin{pmatrix} 1 & 0 \\ 0 & -1 \end{pmatrix}$

$$\mathcal{B} = \{1, -1, e_1, -e_1, e_2, -e_2, e_3, -e_3, e_{12}, -e_{12}, e_{13}, -e_{13}, e_{23}, -e_{23}, e_{123}, -e_{123}\}$$

are as follows:

$$\begin{aligned}
V^{(1)} &= \text{span}\{\mathbf{u}_1\}, & \mathbf{u}_1 &= (1, 1, 1, 1, 1, 1, 1, 1, 1, 1, 1, 1, 1, 1, 1, 1), \\
V^{(2)} &= \text{span}\{\mathbf{u}_2\}, & \mathbf{u}_2 &= (-1, -1, -1, -1, -1, -1, 1, 1, -1, -1, 1, 1, 1, 1, 1, 1), \\
V^{(3)} &= \text{span}\{\mathbf{u}_3\}, & \mathbf{u}_3 &= (-1, -1, -1, -1, 1, 1, -1, -1, 1, 1, -1, -1, 1, 1, 1, 1), \\
V^{(4)} &= \text{span}\{\mathbf{u}_4\}, & \mathbf{u}_4 &= (1, 1, 1, 1, -1, -1, -1, -1, -1, -1, -1, -1, 1, 1, 1, 1), \\
V^{(5)} &= \text{span}\{\mathbf{u}_5\}, & \mathbf{u}_5 &= (-1, -1, 1, 1, -1, -1, -1, -1, 1, 1, 1, 1, -1, -1, 1, 1), \\
V^{(6)} &= \text{span}\{\mathbf{u}_6\}, & \mathbf{u}_6 &= (1, 1, -1, -1, 1, 1, -1, -1, -1, -1, 1, 1, -1, -1, 1, 1), \\
V^{(7)} &= \text{span}\{\mathbf{u}_7\}, & \mathbf{u}_7 &= (1, 1, -1, -1, -1, -1, 1, 1, 1, 1, -1, -1, -1, -1, 1, 1), \\
V^{(8)} &= \text{span}\{\mathbf{u}_8\}, & \mathbf{u}_8 &= (-1, -1, 1, 1, 1, 1, 1, 1, -1, -1, -1, -1, -1, -1, 1, 1), \\
V^{(9)} &= \text{span}\{\mathbf{u}_9, \mathbf{u}_{10}\}, & \mathbf{u}_9 &= (1, -1, 1, -1, 0, 0, 0, 0, 0, 0, 0, 0, -1, 1, -1, 1), \\
& & \mathbf{u}_{10} &= (0, 0, 0, 0, -1, 1, 1, -1, 1, -1, -1, 1, 0, 0, 0, 0), \\
V^{(10)} &= \text{span}\{\mathbf{u}_{11}, \mathbf{u}_{12}\}, & \mathbf{u}_{11} &= (0, 0, 0, 0, 1, -1, 1, -1, -1, 1, -1, 1, 0, 0, 0, 0), \\
& & \mathbf{u}_{12} &= (-1, 1, -1, 1, 0, 0, 0, 0, 0, 0, 0, 0, -1, 1, -1, 1), \\
V^{(11)} &= \text{span}\{\mathbf{u}_{13}, \mathbf{u}_{14}\}, & \mathbf{u}_{13} &= (0, 0, 0, 0, -1, 1, -1, 1, -1, 1, -1, 1, 0, 0, 0, 0), \\
& & \mathbf{u}_{14} &= (1, -1, -1, 1, 0, 0, 0, 0, 0, 0, 0, 0, 1, -1, -1, 1), \\
V^{(12)} &= \text{span}\{\mathbf{u}_{15}, \mathbf{u}_{16}\}, & \mathbf{u}_{15} &= (0, 0, 0, 0, 1, -1, -1, 1, 1, -1, -1, 1, 0, 0, 0, 0), \\
(49) & & \mathbf{u}_{16} &= (-1, 1, 1, -1, 0, 0, 0, 0, 0, 0, 0, 0, 1, -1, -1, 1).
\end{aligned}$$

While the representations  $X^{(i)}$ ,  $i = 1, \dots, 10$  are all inequivalent and irreducible, the remaining two-dimensional irreducible representations are equivalent as follows:

$$X^{(11)} \cong X^{(9)} \quad \text{and} \quad X^{(12)} \cong X^{(10)}.$$

In Table 18, the irreducible representations  $X^{(i)}$  of  $G_{0,3} = \Omega_2$  are realized in irreducible  $G_{0,3}$ -invariant submodules of the group algebra  $\mathbb{C}[G_{0,3}]$  which is decomposed as follows:

$$(50) \quad \mathbb{C}[G_{0,3}] = \bigoplus_{i=1}^{12} V^{(i)}.$$

The submodules  $V^{(i)}$  are spanned by the corresponding vectors  $\mathbf{u}_i$ ,  $i = 1, \dots, 16$ , as shown below. The coordinates of these vectors in the standard basis

$$\mathcal{B} = \{1, -1, e_1, -e_1, e_2, -e_2, e_3, -e_3, e_{12}, -e_{12}, e_{13}, -e_{13}, e_{23}, -e_{23}, e_{123}, -e_{123}\}$$

are as follows:

Tab. 18: Part 1: Representations of  $G_{0,3} = \Omega_2$  for  $K_i$ ,  $i = 1, \dots, 5$ .

	$K_1$	$K_2$	$K_3$	$K_4$	$K_5$
$g$	1	-1	$e_{123}$	$-e_{123}$	$e_1$
$X^{(1)}$	(1)	(1)	(1)	(1)	(1)
$X^{(2)}$	(1)	(1)	(-1)	(-1)	(1)
$X^{(3)}$	(1)	(1)	(-1)	(-1)	(1)
$X^{(4)}$	(1)	(1)	(1)	(1)	(1)
$X^{(5)}$	(1)	(1)	(-1)	(-1)	(-1)
$X^{(6)}$	(1)	(1)	(1)	(1)	(-1)
$X^{(7)}$	(1)	(1)	(1)	(1)	(-1)
$X^{(8)}$	(1)	(1)	(-1)	(-1)	(-1)
$X^{(9)}$	$\begin{pmatrix} 1 & 0 \\ 0 & 1 \end{pmatrix}$	$\begin{pmatrix} -1 & 0 \\ 0 & -1 \end{pmatrix}$	$\begin{pmatrix} -1 & 0 \\ 0 & -1 \end{pmatrix}$	$\begin{pmatrix} 1 & 0 \\ 0 & 1 \end{pmatrix}$	$\begin{pmatrix} i & 0 \\ 0 & -i \end{pmatrix}$
$X^{(10)}$	$\begin{pmatrix} 1 & 0 \\ 0 & 1 \end{pmatrix}$	$\begin{pmatrix} -1 & 0 \\ 0 & -1 \end{pmatrix}$	$\begin{pmatrix} 1 & 0 \\ 0 & 1 \end{pmatrix}$	$\begin{pmatrix} -1 & 0 \\ 0 & -1 \end{pmatrix}$	$\begin{pmatrix} -i & 0 \\ 0 & i \end{pmatrix}$
$X^{(11)}$	$\begin{pmatrix} 1 & 0 \\ 0 & 1 \end{pmatrix}$	$\begin{pmatrix} -1 & 0 \\ 0 & -1 \end{pmatrix}$	$\begin{pmatrix} -1 & 0 \\ 0 & -1 \end{pmatrix}$	$\begin{pmatrix} 1 & 0 \\ 0 & 1 \end{pmatrix}$	$\begin{pmatrix} i & 0 \\ 0 & -i \end{pmatrix}$
$X^{(12)}$	$\begin{pmatrix} 1 & 0 \\ 0 & 1 \end{pmatrix}$	$\begin{pmatrix} -1 & 0 \\ 0 & -1 \end{pmatrix}$	$\begin{pmatrix} 1 & 0 \\ 0 & 1 \end{pmatrix}$	$\begin{pmatrix} -1 & 0 \\ 0 & -1 \end{pmatrix}$	$\begin{pmatrix} i & 0 \\ 0 & -i \end{pmatrix}$

Tab. 18: Part 2: Representations of  $G_{0,3} = \Omega_2$  for  $K_i$ ,  $i = 6, \dots, 10$ .

	$K_6$	$K_7$	$K_8$	$K_9$	$K_{10}$
$g$	$e_2$	$e_3$	$e_{12}$	$e_{13}$	$e_{23}$
$X^{(1)}$	(1)	(1)	(1)	(1)	(1)
$X^{(2)}$	(1)	(-1)	(1)	(-1)	(-1)
$X^{(3)}$	(-1)	(1)	(-1)	(1)	(-1)
$X^{(4)}$	(-1)	(-1)	(-1)	(-1)	(1)
$X^{(5)}$	(1)	(1)	(-1)	(-1)	(1)
$X^{(6)}$	(1)	(-1)	(-1)	(1)	(-1)
$X^{(7)}$	(-1)	(1)	(1)	(-1)	(-1)
$X^{(8)}$	(-1)	(-1)	(1)	(1)	(1)
$X^{(9)}$	$\begin{pmatrix} 0 & -1 \\ 1 & 0 \end{pmatrix}$	$\begin{pmatrix} 0 & -i \\ -i & 0 \end{pmatrix}$	$\begin{pmatrix} 0 & -i \\ -i & 0 \end{pmatrix}$	$\begin{pmatrix} 0 & 1 \\ -1 & 0 \end{pmatrix}$	$\begin{pmatrix} i & 0 \\ 0 & -i \end{pmatrix}$
$X^{(10)}$	$\begin{pmatrix} 0 & i \\ i & 0 \end{pmatrix}$	$\begin{pmatrix} 0 & -1 \\ 1 & 0 \end{pmatrix}$	$\begin{pmatrix} 0 & 1 \\ -1 & 0 \end{pmatrix}$	$\begin{pmatrix} 0 & i \\ i & 0 \end{pmatrix}$	$\begin{pmatrix} i & 0 \\ 0 & -i \end{pmatrix}$
$X^{(11)}$	$\begin{pmatrix} 0 & 1 \\ -1 & 0 \end{pmatrix}$	$\begin{pmatrix} 0 & i \\ i & 0 \end{pmatrix}$	$\begin{pmatrix} 0 & i \\ i & 0 \end{pmatrix}$	$\begin{pmatrix} 0 & -1 \\ 1 & 0 \end{pmatrix}$	$\begin{pmatrix} i & 0 \\ 0 & -i \end{pmatrix}$
$X^{(12)}$	$\begin{pmatrix} 0 & 1 \\ -1 & 0 \end{pmatrix}$	$\begin{pmatrix} 0 & -i \\ -i & 0 \end{pmatrix}$	$\begin{pmatrix} 0 & i \\ i & 0 \end{pmatrix}$	$\begin{pmatrix} 0 & 1 \\ -1 & 0 \end{pmatrix}$	$\begin{pmatrix} -i & 0 \\ 0 & i \end{pmatrix}$

$$\begin{aligned}
V^{(1)} &= \text{span}\{\mathbf{u}_1\}, & \mathbf{u}_1 &= (1, 1, 1, 1, 1, 1, 1, 1, 1, 1, 1, 1, 1, 1), \\
V^{(2)} &= \text{span}\{\mathbf{u}_2\}, & \mathbf{u}_2 &= (-1, -1, -1, -1, -1, -1, 1, 1, -1, -1, 1, 1, 1, 1), \\
V^{(3)} &= \text{span}\{\mathbf{u}_3\}, & \mathbf{u}_3 &= (-1, -1, -1, -1, 1, 1, -1, -1, 1, 1, -1, -1, 1, 1), \\
V^{(4)} &= \text{span}\{\mathbf{u}_4\}, & \mathbf{u}_4 &= (1, 1, 1, 1, -1, -1, -1, -1, -1, -1, -1, -1, 1, 1), \\
V^{(5)} &= \text{span}\{\mathbf{u}_5\}, & \mathbf{u}_5 &= (-1, -1, 1, 1, -1, -1, -1, -1, 1, 1, 1, 1, -1, -1), \\
V^{(6)} &= \text{span}\{\mathbf{u}_6\}, & \mathbf{u}_6 &= (1, 1, -1, -1, 1, 1, -1, -1, -1, -1, 1, 1, -1, -1), \\
V^{(7)} &= \text{span}\{\mathbf{u}_7\}, & \mathbf{u}_7 &= (1, 1, -1, -1, -1, -1, 1, 1, 1, 1, -1, -1, -1, -1), \\
V^{(8)} &= \text{span}\{\mathbf{u}_8\}, & \mathbf{u}_8 &= (-1, -1, 1, 1, 1, 1, 1, 1, -1, -1, -1, -1, -1, -1), \\
V^{(9)} &= \text{span}\{\mathbf{u}_9, \mathbf{u}_{10}\}, & \mathbf{u}_9 &= (1, -1, -i, i, 0, 0, 0, 0, 0, 0, 0, 0, -i, i, -1, 1), \\
& & \mathbf{u}_{10} &= (0, 0, 0, 0, 1, -1, i, -i, i, -i, -1, 1, 0, 0, 0, 0), \\
V^{(10)} &= \text{span}\{\mathbf{u}_{11}, \mathbf{u}_{12}\}, & \mathbf{u}_{11} &= (0, 0, 0, 0, i, -i, 1, -1, -1, 1, i, -i, 0, 0, 0, 0), \\
& & \mathbf{u}_{12} &= (-1, 1, i, -i, 0, 0, 0, 0, 0, 0, 0, 0, -i, i, -1, 1), \\
V^{(11)} &= \text{span}\{\mathbf{u}_{13}, \mathbf{u}_{14}\}, & \mathbf{u}_{13} &= (0, 0, 0, 0, 1, -1, -i, i, -i, i, -1, 1, 0, 0, 0, 0), \\
& & \mathbf{u}_{14} &= (1, -1, i, -i, 0, 0, 0, 0, 0, 0, 0, 0, i, -i, -1, 1), \\
V^{(12)} &= \text{span}\{\mathbf{u}_{15}, \mathbf{u}_{16}\}, & \mathbf{u}_{15} &= (0, 0, 0, 0, -1, 1, -i, i, i, -i, -1, 1, 0, 0, 0, 0), \\
(51) & & \mathbf{u}_{16} &= (-1, 1, -i, i, 0, 0, 0, 0, 0, 0, 0, 0, i, -i, -1, 1).
\end{aligned}$$

While the representations  $X^{(i)}$ ,  $i = 1, \dots, 10$  are all inequivalent and irreducible, the remaining two-dimensional irreducible representations are equivalent as follows:  $X^{(12)} \cong X^{(10)}$  and  $X^{(11)} \cong X^{(9)}$ .

## References

- [1] R. Abłamowicz, **SymGroupAlgebra**, A Maple package for computations in the group algebra of the symmetric group, <http://math.tntech.edu/rafal/cliff12/>, 2013.
- [2] R. Abłamowicz and B. Fauser, *On the transposition anti-involution in real Clifford algebras I: The transposition map*, Linear and Multilinear Algebra **59**, no. 12 (2011), 1331–1358, Online version: 2011, 1–28, iFirst DOI:10.1080/03081087.2010.517201
- [3] R. Abłamowicz and B. Fauser, *On the transposition anti-involution in real Clifford algebras II: Stabilizer groups of primitive idempotents*, Linear and Multilinear Algebra **59**, no. 12 (2011), 1359–1381, Online version: 2011, 1–23, iFirst DOI:10.1080/03081087.2010.517202.
- [4] R. Abłamowicz and B. Fauser, *On the transposition anti-involution in real Clifford algebras III: The automorphism group of the transposition scalar product on spinor spaces*, Linear and Multilinear Algebra **60**, no. 6 (2012), 621–644, iFirst DOI:10.1080/03081087.2011.624093.
- [5] H. Albuquerque and S. Majid, *Clifford algebras obtained by twisting of group algebras*, J. of Pure and Appl. Algebra **171** (2002), 133–148.



- [6] H. W. Braden, *N-dimensional spinors: Their properties in terms of finite groups*, J. Math. Phys. **26** (1985), 613–620.
- [7] S. Caenepeel and F. Van Ostaeyen, *A note on generalized Clifford algebras and representations*, Communications in Algebra, **17**, no. 1 (1989), 93–102.
- [8] D. Cox, J. Little, and D. O'Shea, *Ideals, Varieties, and Algorithms*, Springer, New York 2008.
- [9] L. Dornhoff, *Group Representation Theory, Part A: Ordinary Representation Theory*, Marcel Dekker, Inc., New York 1971.
- [10] D. Gorenstein, *Finite Groups*, New York-Chelsea 1980.
- [11] M. Hall, Jr., and J. K. Senior, *The Groups of Order  $2^n$* . MacMillan, New York 1964.
- [12] G. James and M. Liebeck, *Representations and Characters of Groups*, Cambridge University Press, Cambridge 2001.
- [13] C. R. Leedham-Green and S. McKay, *The structure of groups of prime power order*, London Mathematical Society Monographs, New Series, 27, Oxford University Press, Oxford 2002.
- [14] P. Lounesto, *Clifford Algebras and Spinors*, Cambridge University Press, Cambridge 2001.
- [15] E. A. O'Brien and M. C. Slattery, *Clifford algebras and finite groups*, J. Phys. A: Math. Gen. **22** (1989), 3159–3160.
- [16] J. J. Rotman, *Advanced Modern Algebra*, Prentice Hall, 2002.
- [17] B. E. Sagan, *The Symmetric Group – Representations, Combinatorial Algorithms, and Symmetric Functions*, Wadsworth & Brooks/Cole Mathematics Series, Springer, 2001.
- [18] N. Salingaros, *Realization, extension, and classification of certain physically important groups and algebras*, J. Math. Phys. **22** (1981), 226–232.
- [19] N. Salingaros, *On the classification of Clifford algebras and their relation to spinors in  $n$  dimensions*, J. Math. Phys. **23**, no. 1 (1982), 1–7.
- [20] N. Salingaros, *The relationship between finite groups and Clifford algebras*, J. Math. Phys. **25** (1984), 738–742.
- [21] R. Shaw, *A new view of  $d = 7$  Clifford algebra*, J. Phys. A: Math. Gen. **21** (1988), 7–16.
- [22] V. V. Varlamov, *CPT Groups of Spinor Fields in de Sitter and Anti-de Sitter Spaces*, Adv. Appl. Clifford Algebras **25**, no. 2 (2015), 487–616.

Department of Mathematics  
 University of Kentucky  
 Lexington, KY 40506  
 USA  
 e-mail: kgma225@g.uky.edu

Department of Mathematics  
 Tennessee Technological University  
 Cookeville, TN 38505  
 USA  
 e-mail: rablamowicz@tntech.edu

Presented by Jakub Rembieliński at the Session of the Mathematical-Physical Commission of the Łódź Society of Sciences and Arts on October 29, 2015

## REPREZENTACJE I CHARAKTERY GRUP vee SALINGAROSA NISKIEGO RZĘDU

### S t r e s z c z e n i e

Rozpatrujemy nieredukowalne reprezentacje i charaktery grup vee Salingarosa rzędów 4, 8 i 16 jako 2-grupy o wykładniku 4. W szczególności konstruujemy zespolone nieredukowalne moduły grup i jawne reprezentacje tych grup. Dowodzimy twierdzenie dotyczące liczby klas sprzężenia i liczby nierównoważnych nieredukowalnych reprezentacji stopnia jeden i dwa. Wskazujemy, jak rozłożyć zespoloną algebrę grupy na nieredukowalne podmoduły w zgodności z twierdzeniem Maschkego. Formułujemy dwa algorytmy dla znalezienia baz tych podmodułów, które zależą od metod baz Groebnera. Wreszcie zestawiamy tablice charakterów tych grup.

*Słowa kluczowe:* algebra Clifforda, centrum, tablica charakterów, klasy sprzężenia, wynikowa podgrupa, reprezentacja grupy, baza Groebnera, twierdzenie Maschkego, 2-grupa

## B U L L E T I N

DE LA SOCIÉTÉ DES SCIENCES ET DES LETTRES DE ŁÓDŹ

2016

Vol. LXVI

Recherches sur les déformations

no. 1

pp. 75–91

*Contribution to the jubilee volume, dedicated  
to Professors J. Ławrynowicz and L. Wojtczak*

*Krzysztof Podlaski and Grzegorz Wiatrowski*

**MULTI-OBJECTIVE OPTIMIZATION OF VEHICLE ROUTING  
PROBLEM USING HYBRID GA-PSO ALGORITHM  
WITH MODIFIED BEST COST ROUTE Crossover OPERATOR**

**Summary**

The Vehicle Routing Problem (VRP) is a well-known nondeterministic polynomial (NP) hard and multi-objective optimization problem in computer science. Moreover, VRP has many implementations in everyday life problems like cost optimization in logistics. Established exact methods known today cannot consistently solve VRP instances with 100 customers and more in reasonable time, while in real-life applications this is still not satisfactory. Genetic algorithms (GA) and Particle Swarm Optimization (PSO) are well-known and very promising methods used for solving tasks of this kind. In this paper we propose a modification of Best Cost Route Crossover (BCRC) operator and use it within particle swarm optimization technique. This hybrid GA-PSO algorithm is applied to known Solomon's benchmarks for Vehicle Routing Problem with Time Windows (VRPTW) taking into account two minimization objectives: overall route length and number of vehicles. Our numerical experiments followed by their statistical analysis show that this modified operator gives better results than original BCRC one.

*Keywords and phrases:* vehicle routing problem, time windows, particle swarm optimization, genetic algorithms, multi-objective optimization

**1. Introduction**

There are many combinatorial nondeterministic polynomial (NP) hard problems in computer science that have a real-life applications. One of the most known is Vehicle Routing Problem (VRP) proposed by Dantzig and Ramser in 1959 [5]. Many versions

of VRP were already proposed in the literature. In this paper the Vehicle Routing Problem with Time Windows (VRPTW) is taken into account.

The VRPTW can be described as a task for a depot with an associated fleet of trucks to deliver a cargo to many customers respecting their time constraints. There are following rules important during search for an optimal solution:

- every customer can be visited only once,
- every customer has defined a demand of cargo,
- every customer has defined an opening time window for trucks (ready and due time),
- every customer has defined a service time,
- the time of travel between customers is equal to the distance,
- every truck has defined a capacity and has to deliver supplies to customers within defined time windows,
- a car that arrives too early to a customer has to wait until a service would start at the open time for a given customer,
- if a vehicle arrives after the due time, the customer cannot be serviced.

The problem can be interpreted as a multi-objective optimization task because we have to optimize not only overall distance covered by trucks but also the number of used vehicles.

Many different approaches to VRP were already proposed: exact [6, 10, 27], tabu search [4, 18], heuristic [2, 12], genetic algorithms [3, 17, 19] and swarm intelligence [7, 15, 22]. In order to be able to compare different methods some benchmark tasks were defined, the best known benchmarks are known as Solomon's benchmarks [25].

As it was recalled above, there are some exact methods proposed to solve the VRPTW tasks. However, the complexity of such combinatorial problems makes this approaches computationally difficult. For large problem instances it is rarely possible to obtain an optimal route in reasonable time [14]. Moreover, none of the existing exact methods can solve optimally all VRPTW problems with 100 customers or more. That is the reason why meta-heuristic approaches are much more promising for this kind of optimization problems.

In the paper, we propose a hybrid GA-PSO approach using a new genetic crossover operator based on BCRC. Experimental results discussed below show that using this new crossover operator we obtained better results than with original BCRC.

The paper is organized as follows. In Section 2 the idea of PSO and its hybrid GA-PSO modification for VRPTW is presented. In the same section one can find description of the Best Cost Route Crossover operator as well as Confined Inverse Mutation both used in GA-PSO implementation. In the next Section a proposed

modification of BCRC operator is described in detail. The Section 4 contains the obtained numerical results. The article ends with Conclusions and Bibliography.

## 2. Particle Swarm Optimization for VRPTW

The Particle Swarm Optimization (PSO) is one of evolutionary algorithms based on observation of a real life. The main idea for this method comes from R.C. Eberhart and J. Kennedy and it was introduced in 1995 [9]. PSO is a technique based on observations of a social behaviour of flocking birds. The main goal of PSO is to find, using agent methodology, the point where a fitness function has a minimal or maximal value. In order to find the best place the PSO uses a swarm of particles, each of them moves in a search space and in that way individually search for an optimal spot. The philosophy behind the original particle swarm optimization is to conclude the final solution from its own experience of an individual and the best individual experience of the whole swarm. The rule for particle position changes in continuous space is defined as:

$$(1) \quad \begin{aligned} v_{k,i} &= w * v_{k,i-1} + c_1 * (p_k^{lb} - p_{k,i-1}) + c_2 * (p^{gb} - p_{k,i-1}), \\ p_{k,i} &= p_{k,i-1} + v_{k,i}, \end{aligned}$$

where  $p_{k,i}$  is  $k$ -th particle position in  $i$ -th iteration of algorithm,  $v_{k,i}$  represents velocity of this particle,  $p_k^{lb}$  is  $k$ -th particle local best position and  $p^{gb}$  stands for the global best position in considered swarm,  $w$ ,  $c_1$ ,  $c_2$  are algorithm parameters (weight coefficients).

Presented PSO approach was originally derived for problems in continuous search space. However, the search space of VRPTW problem is a discrete space. That means, in order to use this method for the VRPTW problem one has to redefine the equation (1) and add a new meaning to a particle and its position. There are at least two different approaches: one that uses order encoding [1,15] and the other based on genetic chromosome representation [19,20]. In this paper we choose the latter.

### 2.1. VRPTW formulation for PSO

At first, we have to define what we mean by a particle and its position. The particle in this paper describes one solution of VRPTW and its position contains information of used vehicles and their routes. Each customer is denoted by a unique integer number  $i > 0$ , the depot is denoted as 0. The position of particle is described as a sequence of serviced customers. Each vehicle starts and ends at depot, the order of customers for each vehicle is the same as the order they are visited by a vehicle. For example we can write the position  $p$  of a particle in the form  $p = \{0, 2, 4, 5, 0, 1, 7, 0, 3, 6, 0\}$  and this describe a solution of VRP problem with 7 customers and 3 trucks. The graphical representation of such solution is presented on Fig.1.

In order to solve VRPTW problem all vehicle routes have to preserve time windows constraints and vehicles capacities. The hybrid GA-PSO equation for the position change would have the form:

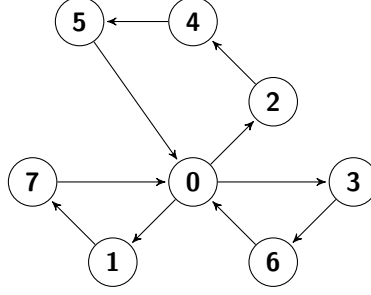


Fig. 1: Graphical representation of the particle position  $p = \{0, 2, 4, 5, 0, 1, 7, 0, 3, 6, 0\}$  for VRP problem with 7 cars and 3 vehicles.

$$(2) \quad p_{k,i} = \begin{cases} p_{k,i-1} \otimes p_k^{lb}, & \text{with probability } \nu^{lb}, \\ p_{k,i-1} \otimes p^{gb}, & \text{with probability } \nu^{gb}, \end{cases}$$

where  $\otimes$  denotes crossover operator and probabilities  $\nu^{lb}$  and  $\nu^{gb}$  depending on overall lengths of  $p_k^{lb}$  and  $p^{gb}$ :

$$(3) \quad \begin{aligned} \nu^{lb} &= \frac{|p_k^{gb}|}{|p_k^{lb}| + |p^{gb}|}, \\ \nu^{gb} &= \frac{|p^{lb}|}{|p_k^{lb}| + |p^{gb}|}, \end{aligned}$$

where  $|p|$  denotes the overall length of route  $p$ .

In the presented approach a genetic crossover operator  $\otimes$  is used for generation of a new particle position. There are many available crossover operators in literature. As a base for our approach we have chosen the Best Cost Route Crossover Operator (BCRC) [19].

We can observe that if historically best particle route  $p_i^{lb}$  is much longer than best swarm position  $p^{gb}$ , we prefer to operate with global best. In the presented approach usage of only the crossover operator could produce too fast convergence to some local optima instead of a global one. That is why we have to introduce mutation operation acting on particles in the swarm. After each iteration step we would apply a mutation to a particle with some chosen probability. In the paper we use the constrained version of the inversion mutation [19].

Then the proposed hybrid GA-PSO algorithm for VRPTW problem has the form:

0. initialize the swarm,
1. for all particles from the swarm,
  - (a) count new position of a particle using (2),
  - (b) perform mutations on a particle,
  - (c) update a particle local best if needed,

- (d) update the swarm global best if needed,
- 2. repeat step 1 until the maximal number of iterations is reached,
- 3. return the swarm global best as an optimization result.

The presented hybrid GA-PSO approach preserves the most important elements from original PSO, the learning from the experience of each individual particle and the experience of the swarm.

## 2.2. Best Cost Route Crossover Operator

The crossover operator in genetic algorithms is used to define how parent's chromosomes influence chromosomes of their offspring. In order to use genetic crossover we need to define a chromosome for VRPTW. In VRPTW a chromosome is a sequence representation of a particle position (presented earlier). There are many crossover operators that can be used for combinatorial problems. Many of them were incorporated to solve the VRP problems [21]. Unfortunately most of such operators applied to VRPTW chromosome erase all information connected to vehicles. After their application we would lose all information about how the route was divided into vehicles. On the other hand the BCRC operator was introduced specially for VRPTW and preserves information about used vehicles and their routes. Suppose we have two parents  $P1$  and  $P2$ . The BCRC recombination procedure is as follows:

1. create an offspring  $O12$  chromosome by copying the chromosome of parent  $P1$ ,
2. select randomly a vehicle  $v$  from parent  $P2$ ,
3. erase all customers serviced by vehicle  $v$  from offspring  $O12$ ,
4. reinsert all customers from  $v$  into  $O12$  in the best possible places, respecting the constraints on truck capacity and customers time windows. If a customer cannot be inserted into existing vehicles in  $O12$  we add a new vehicle in  $O12$ ,
5. create offspring  $O21$  repeating the steps from 1 to 4 exchanging the roles of parents  $P1$  and  $P2$  in the process,
6. select the better of generated offspring  $O12$  or  $O21$ .

The presented procedure ensures that if parents  $P1$  and  $P2$  respect conditions on time and capacity, the obtained offspring also respects these constraints. An easy example of such procedure is presented below:

**Example BCRC operator:** Assume that we have two parents of the form:

$$P1 = \{0, 2, 4, 5, 0, 1, 7, 0, 3, 6, 0\},$$

$$P2 = \{0, 1, 6, 0, 5, 7, 2, 0, 3, 4, 0\}.$$

Their graphical representation is on Fig. 2. We randomly select a vehicle from  $P2$ , suppose it's  $v = \{5, 7, 2\}$ , then copy  $P1$  into offspring  $O12$ . Each customer can be visited only once, that means we have to erase from  $O12$  all customers from selected vehicle  $v$  then the offspring has the form:

$$O12 = \{0, 4, 0, 1, 0, 3, 6, 0\}.$$

Now, we randomly select an element from  $v$ , suppose it's customer 5. We have to check where we could put this element. In the example the most optimal position is after customer 4 is serviced by a second car. We have to repeat the same operation for the rest of elements in  $v$ . If an element cannot be placed anywhere (fulfilling the time or capacity conditions) we have to add a new car to an offspring.

Thus we have finished creation of the offspring:

$$O12 = \{0, 4, 5, 0, 1, 7, 0, 2, 3, 6, 0\}.$$

The graphical representation of presented example is shown on Fig. 2. As we can see most of edges from parent  $P1$  was copied into offspring  $O12$ , and on the other hand none of edges from parent  $P2$  was copied into the offspring  $O12$ . Similar procedure is used to create the second offsprings  $O21$ . At the end the better of two offspring  $O12$  and  $O21$  is used as a result of presented recombination procedure. The better-worse relation for two chromosomes is described in details in section 2.4.

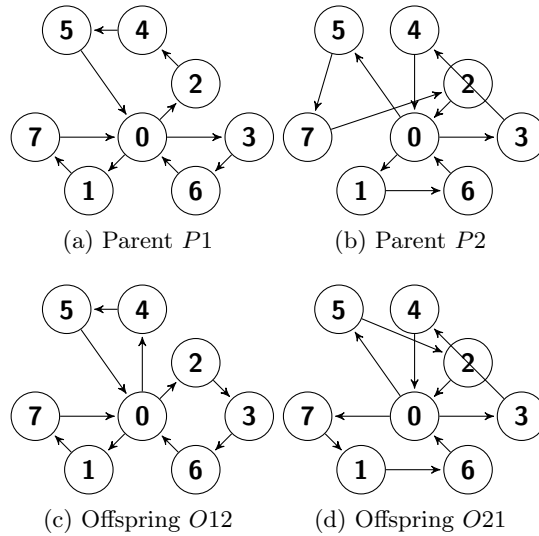


Fig. 2: Graphical representation of BCRC operator example.



### 2.3. Constrained Route Inversion Operator

In order to prevent the hybrid GA-PSO algorithm to stuck on some local optimal point, we introduce mutation operation. The inversion mutation operator was chosen. The operator acts as follows:

1. randomly select the cutting points,
2. invert elements between selected cutting points.

**Example *Inversion Mutation operator*:** Suppose we have a chromosome in the form  $p = \{0, 2, 4, 5, 0, 1, 7, 0, 3, 6, 0\}$ , we randomly select two cutting points inside position  $p = \{0, 2, 4, |5, 0, 1, 7, 0, 3, |6, 0\}$ . Then we have to invert elements between cutting points, after this operation the resulting position is:  $p' = \{0, 2, 4, 3, 0, 7, 1, 0, 5, 6, 0\}$ . Now we have to check if  $p'$  respects conditions on vehicle capacity and arrival times.

The condition on time windows is more probable to be violated if cutpoints are distant. This is the reason why (following [19]) we employ a constraint inversion mutation, which is limited in length to 2-3 customers.

### 2.4. Multi-objectivity and fitness function

At each iteration of presented GA-PSO procedure we have to decide if an actual position is better than the local best or the global best position. For VRPTW problems we may formulate four possible fitness criteria:

- Distance – sum of distances travelled by vehicles in selected solution. The lower value gives a better solution;
- Distance and Vehicles Count – we try to minimize both of these values but we set the higher priority to the distance;
- Vehicles Count and Distance – similar to previous but the distance has lower priority;
- Weighted Method – we try to find a minimum of a fitness function  $F(p) = \alpha|v_p| + \beta|p|$ , where  $|v_p|$  denotes vehicles count in particle  $p$  and  $|p|$  is a distance travelled by vehicles in  $p$ . The parameters  $\alpha$  and  $\beta$  are usually established empirically and most often the values are:  $\alpha = 100$  and  $\beta = 0.001$  [17, 19].

During our experiments we have decided to use Weighted Method. The VRPTW problems were created for the need of logistic companies. Analyzing the cost of such type of activities, we can stress that overall distance is connected to the costs of the fuel and the number of vehicles is connected to the cost of the workforce. The choice of the Weighted Method and the parameters  $\alpha$  and  $\beta$  expresses the idea that for a logistic company it is better (in economical aspects) to spend a little more on the fuel than on the next truck or driver. The choice of fitness policy has important impact on the final results.

### 3. Modification of BCRC operator for VRPTW

The numerical experiments that use the presented BCRC operator within hybrid GA-PSO algorithm for selected Solomon's benchmarks show that there is still place for improvement (see Sec. 4). Analyzing the structure of BCRC operator one can observe that there are parts of chromosome of only one of the parents copied into the offspring, the second parent gives some additional mixing but does not incorporate any part of its own chromosome. This observation leads to the new Modified BCRC operator.

First, we introduce a mean route length  $d_m$  for a vehicle  $v$  as an overall length of route travelled by a car  $v$  divided by the number of visited customers. We denote a distance function between customers  $c_a$  and  $c_b$  as  $dist(c_a, c_b)$ . Assuming that a vehicle  $v$  visits  $n$  customers in sequence  $c_1, c_2, \dots, c_n$ , we can write formula for mean route length as:

$$(4) \quad d_m(v) = \frac{dist(0, c_1) + \left[ \sum_{i=1}^{n-1} dist(c_i, c_{i+1}) \right] + dist(c_n, 0)}{n}.$$

Using proposed mean route length we can order all vehicles in a solution from lowest to highest values of  $d_m$ . Then we denote the vehicle with lowest mean route length in the particle as the best vehicle in the particle and the vehicle with highest  $d_m$  as the worst vehicle in the solution.

Modified BCRC operator applied to parents  $P1$  and  $P2$ :

1. count value of mean length for vehicles in parents  $P1$  and  $P2$ ,
2. identify the best and the worst vehicles  $v_1^b$  and  $v_1^w$  from parent  $P1$  and  $v_2^b, v_2^w$  from  $P2$ ,
3. create offspring  $O12$  chromosome by copying the chromosome of parent  $P1$ ,
4. erase from  $O12$  all customers serviced by  $v_2^b$ ,
5. exchange  $v_1^w$  with  $v_2^b$  in offspring  $O12$ ,
6. select randomly a vehicle  $v$  from parent  $P2$ ,
7. erase all customers serviced by vehicle  $v$  from offspring  $O12$ ,
8. reinsert all customers from  $v$  and  $v_1^w$  into  $O12$  in the best possible places, respecting the constraints on truck capacity and customers time windows. If a customer cannot be inserted into existing vehicles in  $O12$  we add a new vehicle in  $O12$ ,
9. create offspring  $O21$  repeating the steps from 3 to 8 exchanging the roles of parents  $P1, P2$  in the process,
10. select better of generated offspring  $O12$  or  $O21$ .

The proposed Modified BCRC operator incorporates elements of chromosomes from both parents and at the same time finds the best possible places for some of customers (step 8).

#### 4. Experimental results

The described hybrid GA-PSO algorithm, with two presented crossover operators: BCRC and Modified BCRC was implemented. For all optimization tasks the Constrained Route Inversion Operator was used. The results are obtained for selected Solomon's benchmarks with 25, 50 and 100 customers and presented in Tab. 1, 2 and 3. During experiments we used the swarm that contains 30 particles, each run of the algorithm has a maximal number of iterations set to 2500. The mutation was applied to a particle at each iteration with probability 0.1.

The proposed hybrid GA-PSO algorithm used with both crossover operators gives good results comparable with other results published (i.e. [17, 19, 20]), obtained in approaches based on genetic algorithms or particle swarm optimization. The presented results are also very similar to known best solutions obtained usually by exact methods, in every case the known best solution and its reference is given.

Table 1: Results for Solomon's VRPTW benchmark instances with 25 customers. Best means the best result obtained in 100 algorithm runs, Worst is the worst result. Results are presented in the form  $\#V/\#D$  where  $\#V$  – is the number of vehicles used and  $\#D$  – overall distance. The best known results are taken from [11].

Problem	BCRC		Modified BCRC		Best Known $\#V/\#D$
	Best $\#V/\#D$	Worst $\#V/\#D$	Best $\#V/\#D$	Worst $\#V/\#D$	
R101	8/ 618.33	8/ 642.1	8/ 618.33	8/ 625.5	8/ 617.1 [11]
R102	7/ 553.2	7/ 575.0	7/ 553.2	7/ 572.1	7/ 547.1 [11]
R109	5/ 442.7	5/ 456.0	5/ 442.7	5/ 492.6	5/ 441.3 [11]
C201	2/ 215.5	2/ 230.4	2/ 215.5	2/ 247.6	2/ 214.7 [11]
RC201	3/ 361.2	3/ 370.7	3/ 361.2	3/ 372.6	3/ 360.2 [11]

The method presented in this paper gives satisfying result for each of selected benchmarks for any number of customers. As was stressed previously the Modified BCRC operator in most of cases gives better results than BCRC. It is worth to mention that for cases with 100 customers the use of Modified BCRC gives better results than BCRC (Tab. 3). The results of both crossover operators are much more similar for smaller benchmark instances with 25 and 50 customers (Tab. 1, 2).

In most of presented cases the best result has optimal number of vehicles but with longer overall distance than in known optimal solutions. This means that the proposed Modified BCRC operator has still some place for improvements. For cases R105 and RC101 in Tab. 3 the resulting number of vehicles is higher than in best known solution. The case RC101 with 100 customers is even more interesting because our results having higher number of vehicles have also shorter overall travelled distance. However, according to the economic decisions presented in section 2.4 and chosen fitness criteria the best known solution is still better than we obtained. The opposite case is with R201 and R202 for 50 customers (Tab. 2), according to our Weighted Method criteria the obtained solutions are longer but use smaller number of vehicles.

Table 2: Results for Solomon’s VRPTW benchmark instances with 50 customers. Best means the best result obtained in 100 algorithm runs, Worst is the worst result. Results are presented in the form  $\#V/\#D$  where  $\#V$  – is the number of vehicles used and  $\#D$  – overall distance. The best known results are taken from [8, 11, 13].

Problem	BCRC		Modified BCRC		Best Known $\#V/\#D$
	Best $\#V/\#D$	Worst $\#V/\#D$	Best $\#V/\#D$	Worst $\#V/\#D$	
R101	12/ 1057.0	13/ 1109.8	12/ 1058.5	14/ 1111.4	12/ 1044 [11]
R201	4/ 817.7	6/ 873.5	4/ 817.7	7/ 883.0	6/ 791.9 [8]
R202	4/ 729.1	5/ 880.4	4/ 730.7	6/ 825.6	5/ 689.5 [8]
C101	5/ 363.2	6/ 403.6	5/ 363.2	6/ 406.8	5/ 362.5 [11]
C201	3/ 361.8	4/ 459.5	3/ 361.8	4/ 469.2	3/ 360.2 [13]
RC101	8/ 949.8	10/ 1067.4	8/ 949.8	10/ 1065.4	8/ 944 [11]

The difference between Worst and Best solution is noticeable but when we look at the chromosomes we can notice that both solutions are very similar. In order to illustrate this observation we present in Fig. 3 geographical representation of best and worst solutions for problem C201 with 50 customers (Tab. 2). We can see that most of chromosomes of both solutions are identical. One of vehicles is totally the same (blue vehicle), the additional vehicle (green dashed line) in the worst solution (in Fig. 3b) services some of the customers from orange and black vehicles from the best solution (in Fig. 3a).

As is shown on plot of convergence (Fig. 4) the operator BCRC converges faster to the final point and the modified version of BCRC is moving much slower in the direction of the final position. This behaviour can prevent the situation that the

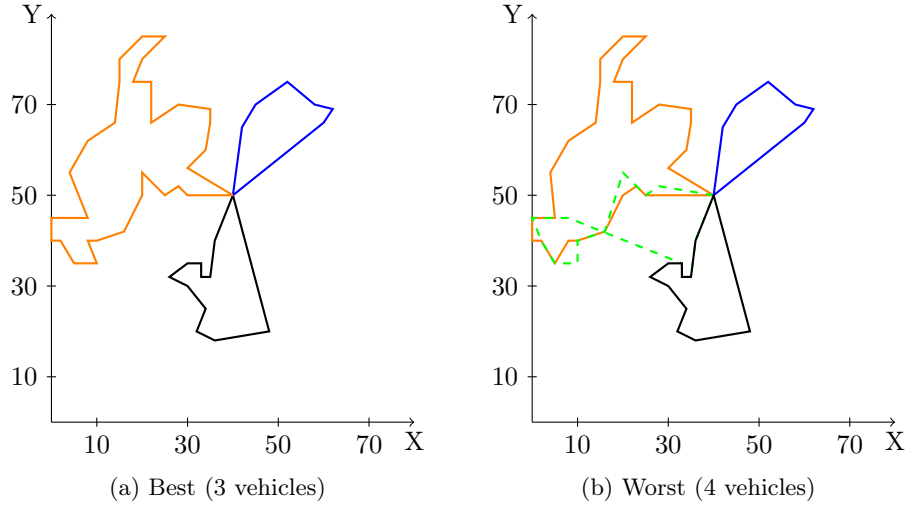


Fig. 3: Geographical representation of Best and Worst solutions for C201 problem with 50 customers according to Tab. 2

Table 3: Results for Solomon's VRPTW benchmark instances with 100 customers. Best means the best result obtained in 100 algorithm runs, Worst is the worst result. Results are presented in the form  $\#V/\#D$  where  $\#V$  – is the number of vehicles used and  $\#D$  – overall distance. The best known results are taken from [23, 24, 26].

Problem	BCRC		Modified BCRC		Best Known $\#V/\#D$
	Best $\#V/\#D$	Worst $\#V/\#D$	Best $\#V/\#D$	Worst $\#V/\#D$	
R101	20/ 1692.6	21/ 1758.2	19/ 1689.8	20/ 1775.8	19/ 1650.8 [23]
R102	18/ 1541.4	19/ 1581.5	17/ 1562.8	20/ 1600.7	17/ 1486.1 [23]
R105	15/ 1447.4	17/ 1582.5	15/ 1434.6	17/ 1642.7	14/ 1377.1 [24]
C101	10/ 828.9	11/ 872.4	10/ 828.9	11/ 869.3	10/ 828.9 [23]
RC101	15/ 1706.5	17/ 1811.2	15/ 1684.0	18/ 1894.4	14/ 1696.9 [26]

algorithm converges too fast into some local optimal solution. Moreover, the PSO-GA optimization procedure used with Modified BCRC operator returns more often better results. This statement is based on consideration of distributions of results obtained with presented crossover operators. Thus, we present also histograms of these distributions on Figs. 5, 6, 7, 8, 9 for the instances with 100 customers.

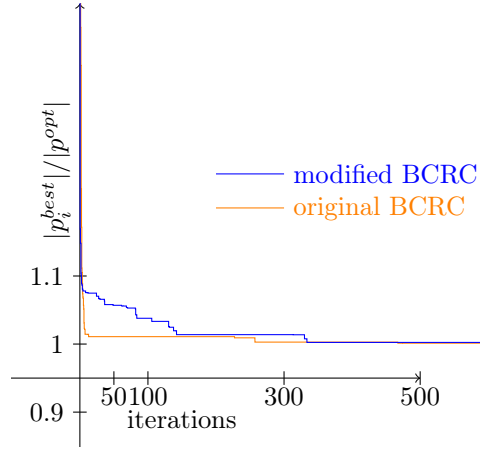


Fig. 4: Convergence of algorithms for best solution R101 with 100 customers using BCRC and Modified BCRC operator.  $|p_i^{gb}|$  – denotes length of global best position in the swarm after  $i$ -th iteration,  $|p^{opt}|$  – length of final optimal solution.

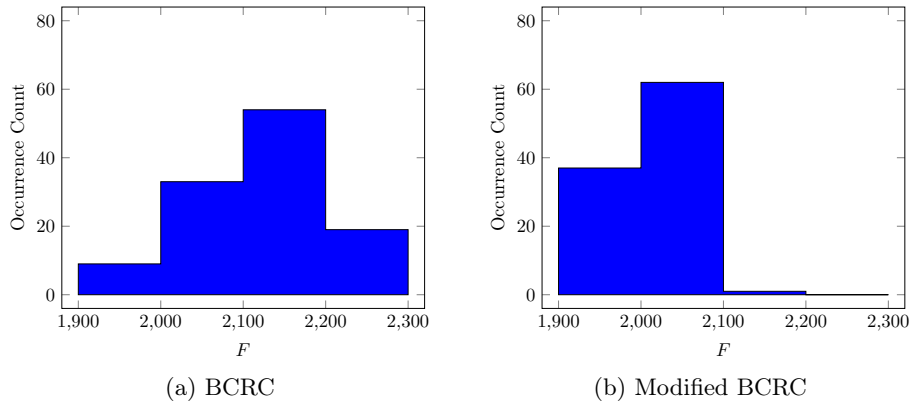


Fig. 5: Histogram of distribution of the the weighted fitness function ( $F$ ) values for instance R101 with 100 customers using BCRC and Modified BCRC operators.  $F(p) = \alpha|v_p| + \beta|p|$ , where  $\alpha = 100$  and  $\beta = 0.001$ .

## 5. Statistical comparison of obtained results

The distribution of results obtained in numerical experiments suggests that approach which uses MBCRC gives better results than the ones with BCRC (Figs. 5, 6, 7, 8, 9). In order to prove this hypothesis we can use Mann-Whitney Test U [16]. This nonparametric statistical test allows to decide if two independent statistical samples came from the same population (have the same statistical distribution). The test defines a statistical number called  $U$ , based on elements from both samples, the value

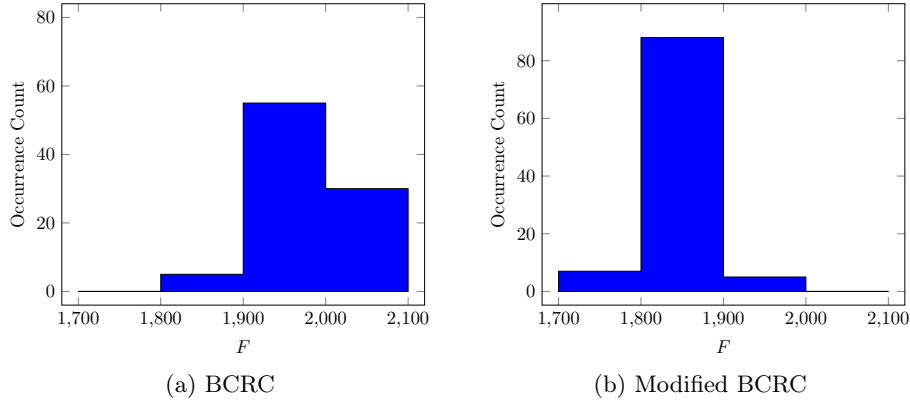


Fig. 6: Histogram of distribution of the the weighted fitness function ( $F$ ) values for instance R102 with 100 customers using BCRC and Modified BCRC operators.  $F(p) = \alpha|v_p| + \beta|p|$ , where  $\alpha = 100$  and  $\beta = 0.001$ .

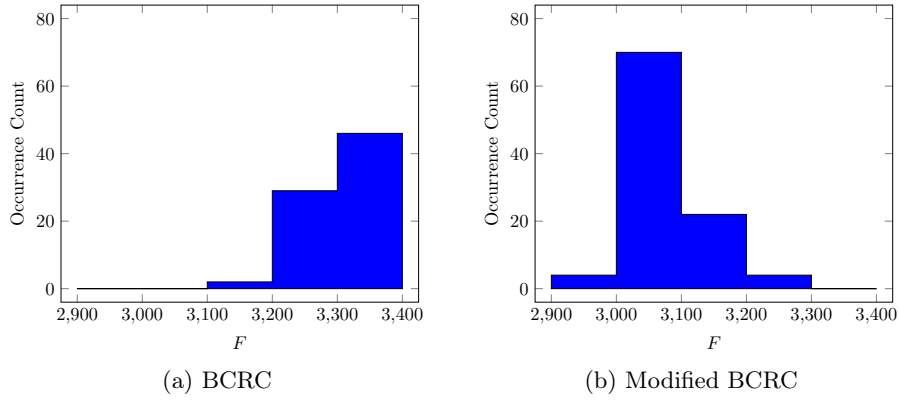


Fig. 7: Histogram of distribution of the the weighted fitness function ( $F$ ) values for instance R105 with 100 customers using BCRC and Modified BCRC operators.  $F(p) = \alpha|v_p| + \beta|p|$ , where  $\alpha = 100$  and  $\beta = 0.001$ .

of  $U$  describes mixing of results in both samples. In many cases Mann-Whitney U test allows to prove if one sample represents population that has statistically bigger values than the other.

At first we have to formulate our null hypothesis ( $H_0$ ) and appropriate alternative hypothesis ( $H_1$ ), then we apply Mann-Whitney Test U in order to decide if we can accept hypothesis  $H_0$ .

**Hypothesis  $H_0$**  The distributions of results for both crossover operators BCRC and MBCRC are statistically the same.

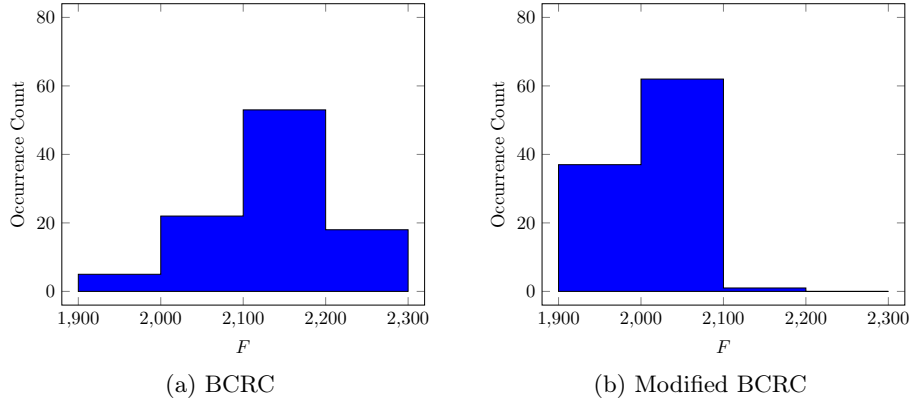


Fig. 8: Histogram of distribution of the the weighted fitness function ( $F$ ) values for instance RC101 with 100 customers using BCRC and Modified BCRC operators.  $F(p) = \alpha|v_p| + \beta|p|$ , where  $\alpha = 100$  and  $\beta = 0.001$ .

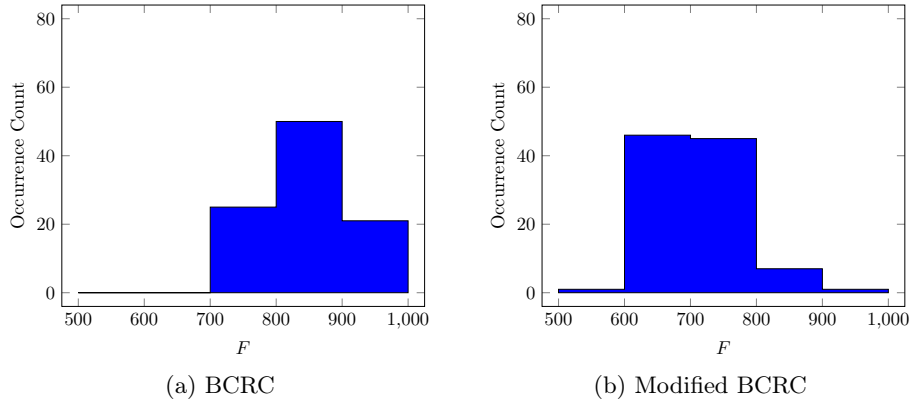


Fig. 9: Histogram of distribution of the the weighted fitness function ( $F$ ) for results obtained for instance RC201 with 100 customers using BCRC and Modified BCRC operators.  $F(p) = \alpha|v_p| + \beta|p|$ , where  $\alpha = 100$  and  $\beta = 0.001$ .

**Hypothesis H1** The distributions of results for both crossover operators BCRC and MBCRC are statistically different.

For each of obtained results the distribution for which we have calculated statistical value  $U$  and appropriate  $z_U$  is given by (5).

$$(5) \quad z_u = \frac{|U - (n_1 n_2 / 2)|}{\sqrt{\frac{n_1 n_2 (n_1 + n_2 + 1)}{12}}},$$

where  $n_1, n_2$  are sizes of statistical ensembles.



The Hypothesis H0 can be accepted with significance set to 0.05 if  $z_U < 2.575$ . The results of our statistical tests for instances with 100 customers are presented in Table. 4. We can conclude that for all considered cases hypothesis H0 has to be rejected.

Table 4: Results of Mann-Whitney Test U calculated for distributions of obtained results for instances with 100 customers.

Problem	$U$	$z_U$
R101	963	9.86
R102	137	11.88
R105	43	12.11
RC101	968	9.85
RC201	250	11.60

## 6. Conclusions

In this paper, we present multi-objective approach to the vehicle routing problem with time windows. A hybrid GA-PSO algorithm is used for numerical experiments with two crossover operators Best Cost Crossover Operator and its modified version. The original BCRC [19] operator was specially derived for VRPTW task. Analysis of this operator lead us to the conclusion that elements of the chromosome of only one of the parents can be found in an offspring. We introduce a modification of this operator in order to ensure that elements from both of parents can be found in an offspring. The results show that for analyzed Solomon's benchmark tasks the introduced Modified BCRC operator gives better results than original BCRC, when used in GA-PSO algorithm for instances with 100 customers. Comparing obtained results with known optimal results and other presented in literature we conclude that proposed method gives satisfying results, statistically better than those obtained using BCRC operator. However there is still place for improvements and the next modifications of presented algorithm will be investigated in the future works.

## References

- [1] T. J. Ai and V. Kachitvichyanukul. *A particle swarm optimization for the vehicle routing problem with simultaneous pickup and delivery*, Computers & Operations Research **36**, no. 5 (2009), 1693–1702.
- [2] M. Battarra, *Exact and heuristic algorithms for routing problems*, 4OR **9**, no. 4 (2011), 421–424.
- [3] J. Berger and M. Barkaoui, *A parallel hybrid genetic algorithm for the vehicle routing problem with time windows*, Computers & Operations Research, **31**, no. 12 (2004), 2037–2053.

- [4] J.-F. Cordeau, G. Laporte, A. Mercier, et al., *A unified tabu search heuristic for vehicle routing problems with time windows*, Journal of the Operational Research Society, **52**, no. 8 (2001), 928–936.
- [5] G. B. Dantzig and J. H. Ramser, *The truck dispatching problem*, Management Science **6**, no. 1 (1959), 80–91.
- [6] M. L. Fisher, *Optimal solution of vehicle routing problems using minimum  $k$ -trees*, Operations Research **42**, no. 4 (1994), 626–642.
- [7] S. Geetha, G. Poonthalir, and P. T. Vanathi, *A hybrid particle swarm optimization with genetic operator for vehicle routing problem*, Journal of Advances in Information Technology **1**, no. 4 (2010).
- [8] B. Kallehauge, J. Larsen, and O. B. Madsen, *Lagrangian duality applied to the vehicle routing problem with time windows*, Computers & Operations Research **33**, no. 5 (2006), 1464–1487.
- [9] J. Kennedy and R. Eberhart, *Particle swarm optimization*, in: Neural Networks, 1995; Proceedings IEEE International Conference **4** (1995), 1942–1948.
- [10] N. Kohl, *Exact methods for time constrained routing and related scheduling problems*, PhD thesis, Technical University of Denmark, 1995.
- [11] N. Kohl, J. Desrosiers, O. B. Madsen, M. M. Solomon, and F. Soumis, *2-path cuts for the vehicle routing problem with time windows*, Transportation Science **33**, no. 1 (1999), 101–116.
- [12] G. Laporte, M. Gendreau, J.-Y. Potvin, and F. Semet, *Classical and modern heuristics for the vehicle routing problem*, International Transactions in Operational Research **7**, no. 4–5 (2000), 285–300.
- [13] J. Larsen, *Parallelization of the vehicle routing problem with time windows*, PhD thesis, Technical University of Denmark, Department of Informatics and Mathematical Modeling, 1999.
- [14] J. K. Lenstra and A. Kan, *Complexity of vehicle routing and scheduling problems*, Networks **11**, no. 2 (1981), 221–227.
- [15] B. Liu, L. Wang, and Y.-H. Jin, *An effective hybrid pso-based algorithm for flow shop scheduling with limited buffers*, Computers & Operations Research **35**, no. 9 (2008), 2791–2806.
- [16] H. B. Mann and D. R. Whitney, *On a test of whether one of two random variables is stochastically larger than the other*, Ann. Math. Statist. **18**, no. 1 (1947), 50–60.
- [17] B. Minocha and S. Tripathi, *Two phase algorithm for solving vrptw problem*, International Journal of Artificial Intelligence and Expert Systems **4** (2013).
- [18] L. Moccia, J.-F. Cordeau, and G. Laporte, *An incremental tabu search heuristic for the generalized vehicle routing problem with time windows*, Journal of the Operational Research Society **63**, no. 2 (2012), 232–244.
- [19] B. Ombuki, B. J. Ross, and F. Hanshar, *Multi-objective genetic algorithms for vehicle routing problem with time windows*, Applied Intelligence **24** (2006), 2006.
- [20] D. Ponce, *Bio-inspired metaheuristics for the vehicle routing problem*, Proceedings of the 9th WSEAS International Conference on Applied Computer Science, World Scientific and Engineering Academy and Society (WSEAS), 2009, 80–84.
- [21] K. Puljić and R. Manger, *Comparison of eight evolutionary crossover operators for the vehicle routing problem*, Mathematical Communications **18**, no. 2 (2013), 359–375.
- [22] M. Reimann, K. Doerner, and R. F. Hartl, *D-ants: Savings based ants divide and conquer the vehicle routing problem*, Computers & Operations Research **31**, no. 4 (2004), 563–591.

- [23] Y. Rochat and É. D. Taillard, *Probabilistic diversification and intensification in local search for vehicle routing*, Journal of Heuristics **1**, no. 1 (1995), 147–167.
- [24] P. Shaw, **Using constraint programming and local search methods to solve vehicle routing problems**, in: Principles and Practice of Constraint Programming-CP98, Springer, 1998, 417–431.
- [25] M. Solomon, *Solomon's vrptw benchmark problems*, 1999.
- [26] É. Taillard, P. Badeau, M. Gendreau, F. Guertin, and J.-Y. Potvin, *A tabu search heuristic for the vehicle routing problem with soft time windows* Transportation science **31**, no. 2 (1997), 170–186.
- [27] Z. Zhang, H. Qin, A. Lim, and S. Guo, *Branch and bound algorithm for a single vehicle routing problem with toll-by-weight scheme*, in: Trends in Applied Intelligent Systems, eds. N. García-Pedrajas, F. Herrera, C. Fyfe, J. Benitez, and M. Ali, Lecture Notes in Computer Science **6098** (2010), 179–188.

Department of Physics and Applied Informatics  
Faculty of Physics and Applied Informatics  
University of Łódź  
Pomorska 149/153, PL-90-236 Łódź  
Poland  
e-mail: podlaski@uni.lodz.pl  
wiatr@uni.lodz.pl

Presented by Ilona Zasada at the Session of the Mathematical-Physical Commission of the Łódź Society of Sciences and Arts on December 16, 2015

## **OPTYMALIZACJA WIELOKRYTERIALNA PROBLEMU MARSZRUTYZACJI WYKORZYSTUJĄCA HYBRYDOWY ALGORYTM GA-PSO WRAZ Z ZMODYFIKOWANYM OPERATOREM KRZYŻOWANIA BCRC**

### **S t r e s z c z e n i e**

Jednym z ciekawszych znanych problemów optymalizacyjnych jest VRPTW (problem marszrutyzacji z ograniczeniami czasowymi). W pracy zaproponowano hybrydowy algorytm optymalizacyjny łączący w sobie elementy dwu metod ewolucyjnych: optymalizacji stadnej (PSO) oraz algorytmów genetycznych (GA). W zaprojektowanym algorytmie wykorzystano znany operator krzyżowania (BCRC) [19], jednocześnie dokonano modyfikacji operatora BCRC tworząc nowy operator MBCRC. Zaimplementowano stworzony algorytm i zastosowano do znanych przykładowych zadań VRPTW. Numeryczne wyniki doświadczeń pokazują dobrą efektywność zaproponowanego algorytmu. Jednocześnie stosowanie zmodyfikowanego operatora MBCRC pozwala uzyskać lepsze wyniki w porównaniu z tymi otrzymanymi przy pomocy operatora BCRC.

*Słowa kluczowe:* optymalizacja globalna, optymalizacja stadna/rojem cząsteczek, genetyczne operatory krzyżowania, problem marszrutyzacji



## B U L L E T I N

DE LA SOCIÉTÉ DES SCIENCES ET DES LETTRES DE ŁÓDŹ

2016

Vol. LXVI

Recherches sur les déformations

no. 1

pp. 93–101

*Contribution to the jubilee volume, dedicated  
to Professors J. Lawrynowicz and L. Wojtczak*

*Marek Moneta, Małgorzata Antoszevska-Moneta and Romuald Brzozowski*

**HEAVY IONS SPUTTERING AND IMPLANTATION OF SURFACE  
MONITORED WITH PIXE****Summary**

Characteristic X-rays emitted from surfaces and specially prepared thin films as a result of impact of slow heavy ions were measured and analysed. Kinematics of the interaction was simulated numerically with stopping and range of ions matter (SRIM) program in time intervals and in grazing incident-exit angle geometry in order to determine dynamics of formation of the subsurface region damaged through heavy ions (HI) implantation, sputtering and interface mixing. It was shown that the structure and composition of surfaces and films are not stable against HI irradiation due to preferential sputtering and implantation of ions and recoils and that dynamics of such a modification can be *in-situ* monitored with particle-induced X-ray emission (PIXE) technique.

*Keywords and phrases:* PIXE, thin film, heavy ions, SRIM, sputtering, implantation, interface mixing

**1. Introduction**

Interaction of heavy ions (HI) with surface of a multicomponent material results in implantation of the beam ions, preferential sputtering of surface elements and selective implantation of recoils, thus changing primary composition of the surface, creation of ion tracks and production of structural defects [1–3]. The intensive kinematic mixing of the surface and interfaces combined with local thermal heating caused by energy deposited in the surface can be observed as the HI slow down [4]. These phenomena determine structural transformations of the materials and influence their electric and magnetic, as well as thermal properties [5–8].

The particle induced X-rays emission (PIXE) is one of the methods which can give an insight into these processes [9, 10]. The method is based on the analysis of characteristic X-rays emitted by atoms excited through collision with HI. It provides information on fundamental atomic excitation and subsequent recombination processes and gives practical information on elemental composition and dynamics of restructuring of the films and subsurface region measured during irradiation [11]. We use PIXE accompanied with extensive simulations to determine transformations and dynamics of composition change in case of multicomponent thin film subjected to prolonged irradiation with HI.

Since HI impact is a destructive event, the X-rays spectra emitted by Si surface and by Fe/Si and Fe/Cu/Si thin films during the irradiation with Ar ions of the energy around 200 keV were measured in subsequent time intervals in order to determine stability of the films against HI sputtering, interface mixing, implantation of HI and creation of recoils and cascades.

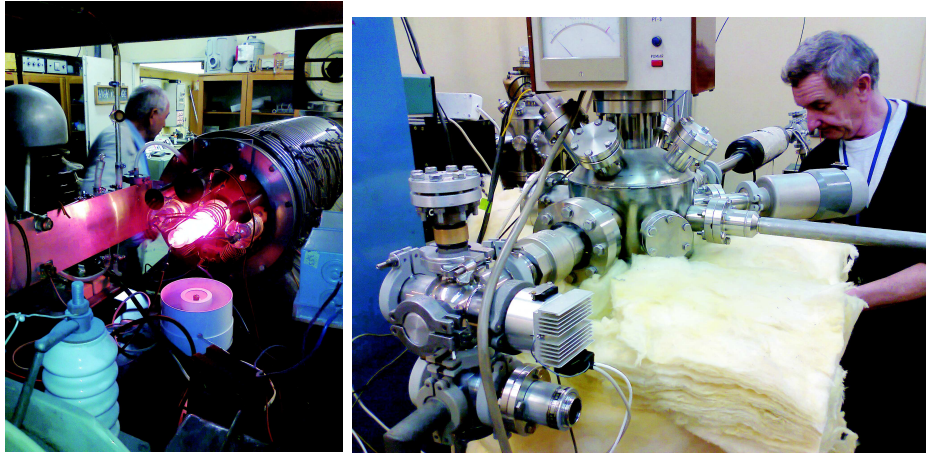


Fig. 1: The present experimental setup based on noble-gas-ion beams from 300 keV accelerator with vacuum in reaction chamber better than 0.1 mPa.

## 2. Experimental set-up

The present experimental setup, shown in Fig.1 was described elsewhere [11]. In brief it is based on noble-gas-ion beams from 300 keV accelerator with vacuum in reaction chamber better than 0.1 mPa. Thin films were evaporated from Knudsen cell on Si surface cleaned from native oxides in HF acid at high temperature. The targets were mounted on a two axis goniometer in double alignment geometry: the incident grazing angle was fixed at  $\phi_{\text{in}} \leq 5^\circ$  and the exit grazing angle was fixed at  $\phi_{\text{out}} \leq 0.5^\circ$  after preliminary measurements minimizing the signal from the Si background. PIXE spectra were measured by a SDD (Si drift detector) spectrometer (fwhm 120 eV@6.4 keV) placed behind a 25  $\mu\text{m}$  kapton window.

### 3. Results and discussion

#### 3.1. Si surface and Fe/Si film against Ar impact

We measured characteristic X-rays emitted during impact of 240 keV Ar ions into Si crystal. Spectra were registered in time sequence as a result of impact of  $10^{11}$  Ar/cm<sup>2</sup> ions through 0.25 mm<sup>2</sup> collimator per 300 s measurement and thus exciting the sample and the previously implanted dose. Incident ions were directed at 45° to the surface and the emitted radiation was measured at grazing exit angle. In this geometry the penetration depth is  $L \approx 170$  nm, the sputtering yield is  $Y \approx 2.6$  Si/Ar [4] so destruction of the surface is negligible, but the RBS yield is  $\approx 1\%$  which means that nearly all the incident ions are implanted, thus changing subsurface composition. Spectra in the inset in Fig. 2 reveal clearly shaped Ar peaks and suppressed bremsstrahlung background. The intensity of signal from Ar, proportional to area under Ar peak in the PIXE spectrum, related to the intensity of signal from Si were drawn in Fig. 2 as a function of implanted Ar dose. There are two regions in the figure: in the first one the signal from Ar fluctuates around the noise level, as if the X-rays were emitted mainly by incident ions. In the second region, above  $10^{12}$  Ar/cm<sup>2</sup>, the signal coming from accumulating Ar could be clearly resolved and the intensity is proportional to implanted dose.

Another analysis of PIXE induced by Ar impact onto Fe(10nm)/Si(110) film is shown in Fig. 3. The X-ray intensity from Ar increases monotonically and shortly becomes comparable with the decreasing signal from Si. Ar atoms in this geometry, are mainly (53%) scattered out of the surface, whereas the remaining (implanted) part tends to be uniformly distributed in the film with a slight density increase (up to 0.06%) in the region of mixed Fe/Si interface [4], thus intensifying radiation through molecular effect in symmetric collisions. The fading radiation from Si substrate can be understood as an effect of absorption of radiation by additional Ar component of the film. The decrease of signal from Fe can be explained by intensive surface sputtering at this geometry  $Y = 30$  Fe/Ar, thus thinning the film at speed of 1 Å of Fe per  $10^{12}$  Ar/cm<sup>2</sup> dose, as it is illustrated in Fig. 3.

#### 3.2. PIXE from Fe/Cu/Si thin film irradiated with Ar

An example of the PIXE spectrum with Fe, Cu and Si K-shell X-rays emitted by a trilayer Fe(10 Å)/Cu(10 Å)/Si(110) during irradiation with Ar ions of the energy 200 keV at  $3 \times 10^{12}$  Ar/cm<sup>2</sup>, is shown in Fig. 4. The spectrum also contains K-shell signal from Ar which is accumulated during irradiation and signals from trace impurities S, Cl and elements contained in the environment Mn, Ni. The ions were directed at the incidence angle  $\phi_{in} = 3^\circ$  to the surface in order to have low penetration depth. Radiation was measured at the grazing exit angle in order to suppress bremsstrahlung.

In order to determine stability of the films against HI sputtering and recoil implantation, again we used time sequence in measuring X-ray signals coming from the

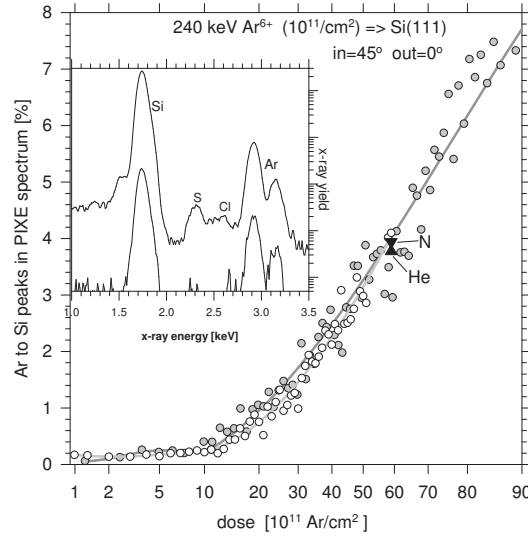


Fig. 2: Ar K-X-rays intensity in the PIXE spectrum induced during irradiation of Si wafer with 240 keV Ar $^{6+}$ . The detection limit is about  $10^{12}$  Ar/cm $^2$   $\sim$  1.2 ppm of Ar in Si. The ratio of Ar/Si measured with 240 keV He and N ions shown with arrows. The angles are measured in respect to Si surface.

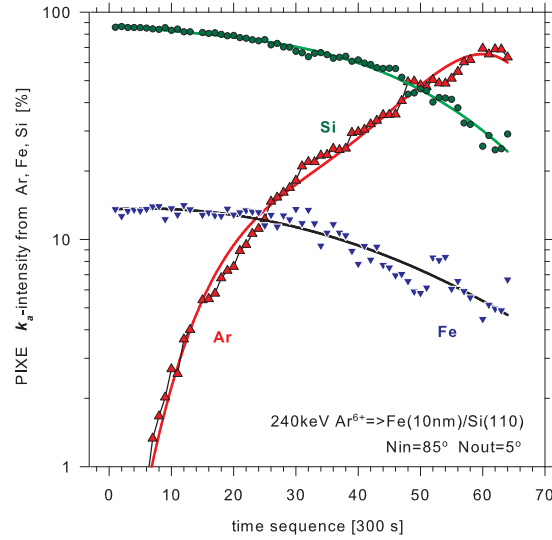


Fig. 3: Time sequence dependence of the intensity of radiation from Fe, Si and Ar in the PIXE spectra during impact of 240 keV Ar ions on Fe(10 nm)/Si(110) film. The 300 s corresponds to an implanted dose of  $10^{12}$  Ar/cm $^2$ . The sputtering yield  $Y = 30$  Fe/Ar, the Ar RBS = 0.53 [4]. The angles are related to the surface normal.



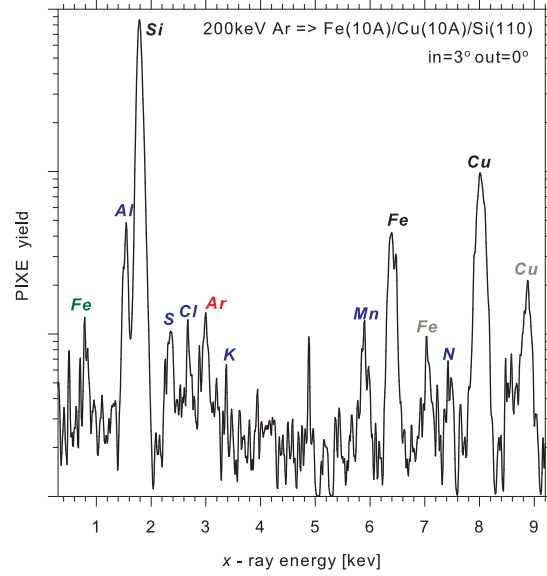


Fig. 4: PIXE spectrum induced during irradiation of Fe(10 Å)/Cu(10 Å)/Si(110) with 200 keV Ar<sup>6+</sup>. The implanted dose  $3 \times 10^{12}$  Ar/cm<sup>2</sup> corresponds to about 3.5 ppm of Ar. Thin films were evaporated from Knudsen cell. Thickness was measured with a quartz resonator. Angles  $\phi_{in} = 3^\circ$  and  $\phi_{out} = 0^\circ$  are related to the surface. The SDD X-ray spectrometer with the resolution of 120 eV/6.4 keV was used. Figure from [11].

films or implanted elements and related them to the signal from Si base. The result of PIXE analysis for 200 keV Ar impact on Fe(10 Å)/Cu(10 Å)/Si(110) is shown in Fig. 5. It can be seen that not only signals from Fe and Cu decrease by a few per cent but also the signal from Si loses intensity, whereas radiation from Ar increases proportionally to the implanted dose and becomes detectable at the concentration of a few ppm. That means that use of HI at this geometry enables X-ray characterisation of the film, despite the destructive consequences of HI impact.

In order to get some insight into the ion scattering process, the present experimental arrangement with 50–250 keV Ar ion beam impact on Fe/Cu/Si trilayer and on Fe/Si bilayer at  $5^\circ$  angles of incidence (and other appropriate initial parameters) were simulated with stopping and range of ions in matter (SRIM) program [4] and presented in Fig. 6. They reveal that emission of atomic species from the irradiated surface is strongly energy and incident angle dependent. Also reflection of incident ions from the surface shows the similar angular dependence. In the grazing incidence geometry  $\phi_{in} < 5^\circ$ , an Ar ion can sputter about 30 Fe atoms and about 50% incident Ar ions fluence is scattered back from the surface, whereas the remaining part is implanted. If an incident fluence of  $10^{15}$  Ar/cm<sup>2</sup> at  $\phi_{in} = 5^\circ$  is assumed, a 3 nm thick layer will be sputtered from the Fe surface. This should be compared

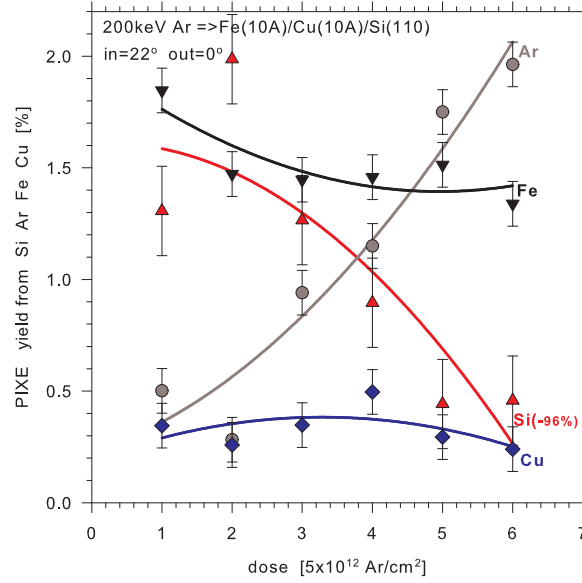


Fig. 5: Stability of Fe(10 Å)/Cu(10 Å)/Si(110) thin film against the dose of 200 keV Ar beam at the grazing-exit geometry measured by signals from Ar, Fe, Cu and Si in the PIXE spectra shown in Fig. 4. Angles  $\phi_{in} = 22^\circ$  and  $\phi_{out} = 0^\circ$  are related to the surface. Figure from [11].

with penetration depth of 40 nm and projected range of 100 nm of Ar ions in Fe. Before backscattering or stopping the ions suffer multiple collisions losing energy to electrons and creating vacancies and cascades. The Cu film and Si substrate are expected to be sputtered at a negligible yield of 0.45 Cu/Ar (Cu atoms per incident Ar ion) and 0.35 Si/Ar respectively, thus being completely screened by Fe film.

In *SRIM*-simulation of irradiation of Fe(10 Å)/Cu(10 Å)/Si trilayer with 220 keV Ar ions at the grazing incidence of  $5^\circ$  we observe in Fig. 7 depth distributions: of the energy absorbed by Fe, Cu and Si recoils – in (a), of these recoils themselves – in (b), of vacancies left behind these recoils – in (c), and of the energy on ionisation lost by the ions and recoils – in (d). It can be seen that ions backscattering, recoils sputtering, transfer of energy, creation of vacancies and recoils cascades are localised in the surface itself and dominate in the first thin film. The depth distributions of Fe, Cu and Si recoils prove extensive interface mixing and deep homogenization of the irradiated trilayer through implantation of recoils. The part of incident ions which is not backscattered travels in the surface layer, initializes cascades and excites atoms in the topmost thin films. That means that in this geometry there is measured the PIXE radiation which is emitted mainly from the excited target atoms leaving the surface and from the incident ions backscattered in an excited state. Radiation from deep layers and substrate should be fairly suppressed.

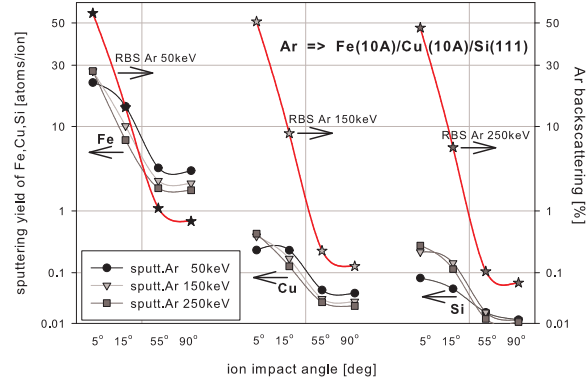


Fig. 6: Erosion of the surface composed of thin films subjected to HI irradiation as sputtering yield of Fe(10 Å)/Cu(10 Å)/Si(111) trilayer under impact of 50–250 keV Ar ions at different incident angles – simulation with *SRIM* [4]. Also, the reflection of the ion beam as backscattering (RBS) of incident Ar ions is shown as a function of initial energy and angle of impact on the surface.

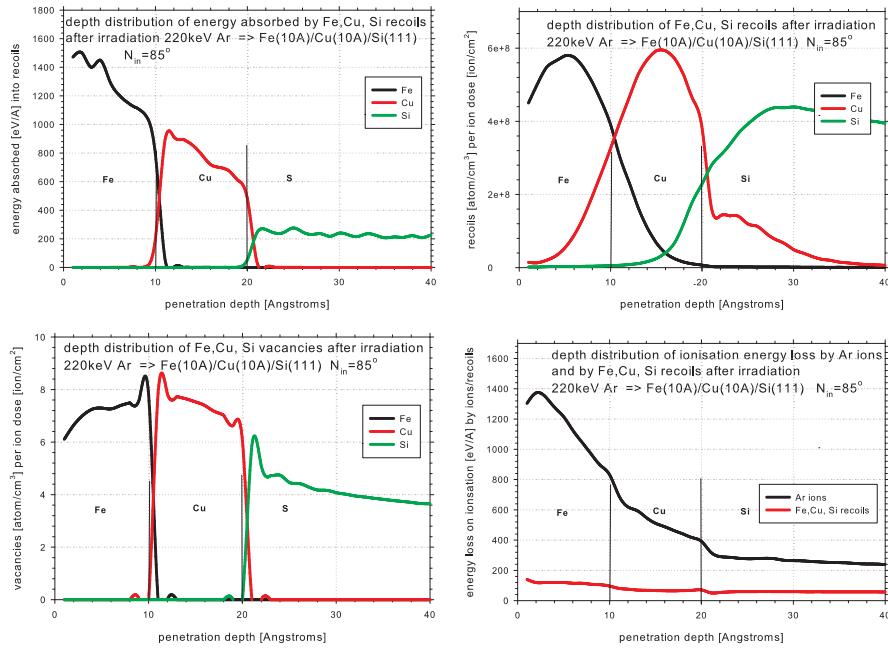


Fig. 7: From top-left to bottom-right respectively the depth distributions of: a) the energy absorbed by recoils, b) Fe, Cu, Si recoils, c) vacancies, and d) the energy loss by ions and recoils on ionisation in Fe(10 Å)/Cu(10 Å)/Si trilayer after irradiation with 220 keV Ar ions at the grazing incidence of 5°. Calculated with *SRIM* [4].

## 4. Conclusions

There was shown with the use of simulation with *SRIM* that the structure and composition of the surface is not stable against HI irradiation due to preferential sputtering, interface mixing and implantation of ions and recoils and that dynamics of such modification can be quantitatively monitored by means of the PIXE measurements.

## References

- [1] M. Toulemonde, C Dufour, and E. Paumier, Phys. Rev. B **46** (1992), 14362.
- [2] A. El-Said, R. Heller, W. Meissl, R. Ritter, S. Facsko, C. Lemell, B. Solleder, I. Gebeshuber, G. Betz, M. Toulemonde, W. Moller, J. Burgdorfer, and F. Aumayr, Phys. Rev. Lett. **100** (2008), 237601.
- [3] B. Pawłowski and M. Moneta, Nucl. Instr. Meth. Phys. Res. B **297** (2012), 194.
- [4] J. F. Ziegler, J. P. Biersack, and M. D. Ziegler, *The Stopping and Range of Ions in Solids*, (2008) <http://www.SRIM.org>.
- [5] G. Herzer, IEEE Trans. Magn. **26** (1990), 1397.
- [6] R. Brzozowski, M. Wasiak, H. Piekarski, P. Sovak, P. Uznański, and M. Moneta, J. Alloys Comp. **470** (2009), 5.
- [7] M. Moneta, R. Brzozowski, M. Wasiak, and P. Uznański, Nucl. Instr. Meth. Phys. Res. B **267** (2009), 411–414.
- [8] R. Brzozowski and M. Moneta, Nucl. Instr. Meth. Phys. Res. B **297** (2012), 208.
- [9] S. A. E. Johansson and J. L. Campbell, and K. G. Malmqvist. *Particle Induced X-ray Emission Spectrometry (PIXE)*, Wiley, 1995.
- [10] Y. Mokuno, Y. Horino, A. Kinomura, A. Chayahara, N. Tsubouchi, and K. Fujii, Nucl. Instr. Meth. Phys. Res. B **109** (1996), 573.
- [11] M. Antoszewska, R. Brzozowski, J. Balcerski, K. Dolecki, E. Frątczak, B. Pawłowski, M. Moneta, Nuclear Instr. Meth. Phys. Res. B **310** (2013), 27–31.

Department of Solid State Physics  
 Faculty of Physics and Applied Informatics  
 University of Łódź  
 Pomorska 149/153, PL-90-236 Łódź  
 Poland  
 e-mail: marek\_moneta@uni.lodz.pl

Presented by Marek Moneta at the Session of the Mathematical-Physical Commission of the Łódź Society of Sciences and Arts on September 10, 2015

## ROZPYLANIE CIĘŻKIMI JONAMI I IMPLANTACJA POWIERZCHNI MONITOROWANA PRZY POMOCY PIXE

### S t r e s z c z e n i e

Zmierzono i przeanalizowano charakterystyczne promieniowanie X emitowane na skutek uderzenia powolnych ciężkich jonów z powierzchnią i specjalnie przygotowanymi cienkimi warstwami. W celu określenia dynamiki formowania się obszarów przypowierzchniowych uszkodzanych w wyniku implantacji ciężkich jonów, rozpylania i mieszania się międzywierzchni, kinematykę oddziaływania przeanalizowano numerycznie programem SRIM w funkcji czasu oraz w geometrii stycznego padania jonów i detekcji promieniowania. Pokazano, że struktura i skład powierzchni i warstw są niestabilne wobec napromieniowania ciężkimi jonami, preferencyjnego rozpylania pierwiastków, implantacji jonów i atomów odrzutu oraz że dynamika takich zmian może być monitorowana w trakcie ich zachodzenia metodą PIXE.

*Słowa kluczowe:* implantacja ciężkich jonów i rozpylanie powierzchni, PIXE, SRIM



## B U L L E T I N

DE LA SOCIÉTÉ DES SCIENCES ET DES LETTRES DE ŁÓDŹ

2016

Vol. LXVI

Recherches sur les déformations

no. 1

pp. 103–122

*Contribution to the jubilee volume, dedicated  
to Professors J. Lawrynowicz and L. Wojtczak*

*Ewelina Z. Frątczak, Paweł Uznański, and Marek E. Moneta*

**MOLECULAR ORGANIZATION IN PENTACENE THIN FILM ON  
SiO<sub>2</sub> SURFACE USING SPECTROSCOPIC ELLIPSOMETRY,  
INFRARED SPECTROSCOPY, AND ATOMIC FORCE  
MICROSCOPY**

**Summary**

Thin films of pentacene of 32-nm thickness obtained by organic molecular beam deposition (OMBD) in high vacuum conditions onto silicon/native silica (Si/SiO<sub>2</sub>) and fused silica substrates were examined. Anisotropic optical properties, alignment and morphology were studied in ambient conditions using variable angle spectroscopic ellipsometry (VASE), UV-VIS absorption, infrared (IR) transmission and polarized grazing angle attenuated total reflection (GATR) techniques, and atomic force microscopy (AFM). The symmetry assignment of the vibrational transitions was also discussed. The films exhibit continuous texture with uniaxial alignment of pentacene molecules and strongly anisotropic optical properties evidenced in the ellipsometric measurements. For the first time dichroic GATR IR spectra were recorded for thin films and conclusions on pentacene orientation were deduced on the basis of dichroic ratio of the IR-active vibrations.

*Keywords and phrases:* pentacene, optical properties, molecular orientation, ellipsometry, infrared spectroscopy, atomic force microscopy

**1. Introduction**

The impact of structure, alignment and morphology on a function, performance, and lifetime of organic devices is of high interest for organic light emitting diodes (OLEDs), organic field effect transistors (OFETs) or organic photovoltaic cells

(OPVs) [1]. Nowadays, the most important growth strategy is based on the use of surfactants or self-assembled monolayers [2–7]. High-ordered layers can be produced on organic substrates as interface structures between the active layer and dielectrics [2]. Different types of organic molecules deposited in ultra-high vacuum (UHV) conditions on inorganic surfaces show various molecular orientation and anisotropic properties depending on a structure of the molecule and the nature of substrate.

Among many organic semiconducting molecules, pentacene (PEN) is a leading molecule to have one of the highest field-effect mobility of free charge carriers and stability among organic semiconducting materials, and it is still the subject of extensive studies [8–10]. Thin film structures of pentacene were investigated by X-ray diffraction (XRD) [8, 11], atomic force microscopy (AFM) [9, 11], ellipsometry [10, 12–15], infrared [16–20] and Raman spectroscopy [11], to elucidate the impact of ordering and grain morphology on OFET performance [9, 21]. Thin pentacene films on common dielectric layers such as  $\text{SiO}_2$  exhibit a coexistence of morphologically multiple phases which, after attaining the appropriate thickness, grow sequentially during deposition. Vapor-deposited pentacene nucleates as orthorhombic phase with interlayer spacing 1.57 nm and after obtaining a critical thickness of 16–30 nm starts to grow as “thin film” phase and further as triclinic phase [8, 11]. The deposition process is identified as a gradual decrease of a tilt angle of pentacene long axis from the substrate surface from  $\sim 78^\circ$  to  $\sim 65^\circ$ . The molecular orientation determines the morphological properties, which strongly affect the charge transport properties [9, 21].

In this work we present data on optical and structural investigations of pentacene films arising from its organization examined by spectroscopic ellipsometry and a modern and extremely sensitive infrared (IR) technique, which allows to characterize very thin molecular materials together with determination their molecular orientation. Thin films of pentacene were deposited in high vacuum by organic molecular beam deposition (OMBD). Optical and structural measurements were performed *ex situ* under ambient conditions. The film growth was monitored by a quartz crystal microbalance and its thickness was determined from the ellipsometric measurements. The orientation of pentacene molecules was deduced from vibrational analysis obtained by Fourier transform infrared spectroscopy (FTIR) with attenuated total reflectance geometry at grazing angle (GATR) and a transmission mode. Single reflection Ge-GATR with polarized irradiation is a powerful tool for the investigation of a thin film on a silicon substrate [22, 23]. Although thin pentacene films were studied previously by IR spectroscopy in the multiple internal reflection geometry [20] and by reflection-absorption mode on gold surface [18, 24], GATR method is a new approach for pentacene thin films investigation. This method is simple, and much more available than sophisticated XRD methods [8, 11, 25, 26] and other IR thin film analyzing techniques [18, 24]. In this paper we show how from the spectroscopic ellipsometry (VASE) measurements and polarized IR GATR spectra one can obtain information on organization of pentacene molecules on silicon substrate.



The results are consistent with previous IR studies [18]. The detailed results of the ellipsometric and IR studies were completed by UV-VIS, which can also probe the mean orientation of the PEN molecules in the thin film. The surface morphology was examined by AFM. Polarized vibrational modes studied in this work can help to specify the orientation of the sputtered samples which, in turn, is responsible for structural properties and consequently for the charge transport properties [9, 27, 28].

## 2. Experimental methods

Powdered pentacene product of Sigma-Aldrich Co. was used as supplied for samples preparation. Native Si/SiO<sub>2</sub> and fused silica wafers were used as substrates. The substrates were cleaned in acetone and alcohol in three 15 min. cycles using ultrasonic bath, and dried in nitrogen stream. Growth of pentacene layers was carried out using OMBD method in a UHV chamber at pressure of  $4 \cdot 10^{-7}$  mbar. The chamber was equipped with a home-made evaporator located at the bottom, whereas the samples were placed centrally above the evaporator in the upper part of the chamber. The distance between the source compound and substrate was 12 cm. Pentacene was deposited on the substrates at temperature of 25° C with the deposition rate 1 nm/min. There were more samples deposited in the experiment [29] but the one of 32-nm thickness is discussed in the article.

Optical parameters of the PEN films were determined by means of spectroscopic ellipsometry using V-VASE apparatus and software (J. A. Woolam Co. Inc.). The measurements were taken at four different angles of light incidence from 45° to 75° in steps of 10°. Experimental ellipsometric parameters  $\Psi$  and  $\Delta$  were collected in steps of 1 nm throughout the spectral range from 260 to 1300 nm. The ellipsometry data were analyzed using the commercial *WVASE32* software. Spectroscopic ellipsometry (SE) is commonly applied for measurements of thin film thickness and optical constants. The data contain a measured change in a polarization state of light after interaction with the sample [30]. A beam source produces unpolarized light which passes through a polarizer. The polarizer axis is set between *p*- and *s*-planes that both can arrive at the sample surface. The polarized light reflects from the sample surface, becomes elliptically polarized and passes through a rotating polarizer (analyzer). The amount of light passing through depends on the orientation of the polarizer to the electric field coming from the sample. The change in polarization of the reflected light is compared to the input polarization after conversion of the output polarization into electronic signal by a detector.

The optical properties of PEN films were isotropic within the plane of the film as it was observed by rotating the sample on the ellipsometer holder. However, the ellipsometric parameters of the PEN films could not be properly computer-simulated using the isotropic model due to a large optical anisotropy between in-plane and out-of-plane direction. Modeling of experimental data and determination of optoelectronic properties, and the film thicknesses have been correctly carried out only

with application of an uniaxial model and a General Oscillator Model. General Oscillator (GenOsc) allows to combine a large number of oscillator models and dispersion relations to model even very complicated dielectric functions. Complementary measurements were performed using UV-VIS spectroscopy (HP 8453 diode array spectrophotometer).

Optical and structural studies were performed to determine the properties of pentacene layers on SiO<sub>2</sub> surface. For this purpose attenuated total reflection spectroscopy, which utilizes total internal reflection phenomenon, was used. Vibrational spectra of pentacene molecules were measured by IR spectroscopy on a Thermo Nicolet 6700 FTIR spectrometer with 4 cm<sup>-1</sup> resolution. Attenuated total reflection spectra (ATR) were measured using single reflection Golden Gate accessory (Specac) with a diamond-ATR crystal at 45° incident angle. Analysis of thin film was carried out with the VariGATR grazing angle ATR optical system (Harrick Scientific Products, Inc.) equipped with a slip-clutch exerting 492 gcm<sup>-2</sup> of pressure for improving contact between the sample and the Ge-ATR crystal. In the experiment a KRS-5 gold wire grid polarizer was used. Different bands intensities, related to characteristic vibrations of chemical bonds in polarized IR spectra in incident plane (*p*-polarization) and perpendicular to it (*s*-polarization), enable for determining of polarization of transition moments. Internal reflection spectra were measured with unpolarized and polarized light at 63° incidence optimized for the highest sensitivity. For weakly absorbing pentacene films deposited on a SiO<sub>2</sub> substrate, the sensitivity is even more enhanced when the film thickness is much smaller than the wavelength of the light. In the GATR experiment a Ge crystal with a high refractive index and excellent IR transmitting properties is placed in close contact with the sample. The beam of propagating irradiation undergoes total internal reflection at the sample interface from a medium with a higher refractive index,  $n_1$  into a medium with a lower refractive index,  $n_2$ , provided the angle of incidence at the interface exceeds the critical angle  $\theta$  (Fig. 1). Total internal reflection of the light at the interface between two media of different refractive index creates an evanescent wave that penetrates into the medium of lower refractive index. The evanescent field is a wave which propagates normal to the surface, whose intensity decreases deeper in the medium, therefore, the field exists only in the vicinity of the surface. The total electric field  $E$  in the medium is split into two perpendicular vectors: an  $E_x$  component parallel to the surface and an  $E_z$  component perpendicular to the surface. Thus the evanescent wave refers to the  $E_z$  component. The component  $E_x$  passes continuously through a layer system of optically different phases and therefore retains its initial field amplitude throughout the layer system. The perpendicular electric field passing through the interface between media of different densities experiences a strong amplification that corresponds to enhancement of the perpendicular vibrations in the IR spectrum. Because in GATR geometry a thin organic film is sandwiched between a germanium ATR crystal and a silicon substrate, the evanescent wave will be absorbed by the sample and its intensity is attenuated in regions of the IR spectrum where the sample

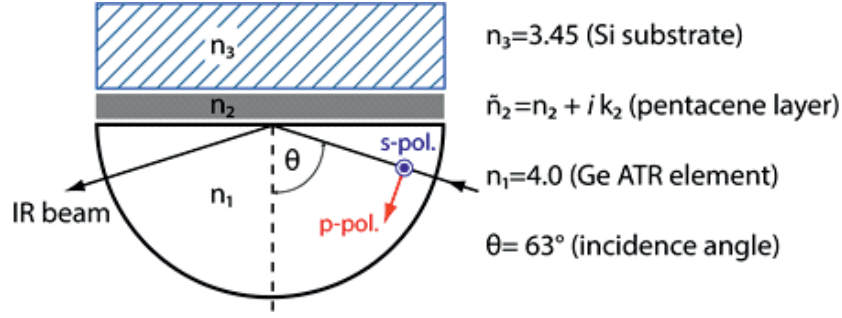


Fig. 1: Scheme of geometrical configuration of a GATR optical element with a definition of directions of IR polarized beam.

absorbs, thus, less intensity can be reflected. The resultant attenuated radiation as a function of wavelength produces an ATR spectrum which is similar to the conventional absorption spectrum. Theoretical calculations show that the enhanced electric field perpendicular to the Ge surface [22, 23, 31] allows detecting weak bands and molecular orientation of pentacene in a thin film when polarized light is applied.

Preliminary estimation of the sample surface topography and morphology of the deposited pentacene layers required AFM measurements. The images were recorded under ambient atmosphere at 25° C using a Nanoscope IIIa MultiMode microscope (Veeco, Santa Barbara, CA) equipped with a commercially available rectangular probe (RTESP from Veeco) with a scanner of the highest available sampling resolution of  $512 \times 512$  data points. The AFM images were analyzed by the *WSxM* program [32].

### 3. Basic theory

Theoretical description of spectroscopic ellipsometry and GATR technique is related to reflectance expressed by ratio of Fresnel reflection coefficients  $r_p$  and  $r_s$  for  $p$ - and  $s$ -polarized light:

$$(1) \quad \rho \equiv \frac{r_p}{r_s}.$$

Expression in Eq. (1) can be developed differently depending on which parameters are measured in each technique [13, 22]. Fresnel reflection coefficients come from Snells law which satisfies the Maxwell equations when light entering the material is refracted at an angle  $\Phi_t$ :

$$(2) \quad n_0 \sin \Phi_i = n_1 \sin \Phi_t,$$

where  $n_0$  and  $n_1$  are the refractive indexes of the incident and refraction medium,  $\Phi_i$  and  $\Phi_t$  are the incident and refractive angles.

In spectroscopic ellipsometry for bulk materials reflected or transmitted light must be separated into orthogonal components because of the boundary conditions

providing different solutions for electric fields parallel and perpendicular to the sample surface. The electric field parallel to the incidence plane is called  $p$ -polarized and the perpendicular one  $s$ -polarized. Thus the Fresnel reflection and transmission coefficients can be calculated independently:

$$(3a) \quad r_p = \frac{n_1 \cos \Phi_i - n_0 \cos \Phi_t}{n_0 \cos \Phi_t + n_1 \cos \Phi_i},$$

$$(3b) \quad r_s = \frac{n_0 \cos \Phi_i - n_1 \cos \Phi_t}{n_0 \cos \Phi_t + n_1 \cos \Phi_i},$$

$$(3c) \quad t_p = \frac{2n_0 \cos \Phi_i}{n_0 \cos \Phi_t + n_1 \cos \Phi_i},$$

$$(3d) \quad t_s = \frac{2n_0 \cos \Phi_i}{n_0 \cos \Phi_i + n_1 \cos \Phi_t}.$$

For thin films the phase thickness (optical thickness) of a film is defined as:

$$(4) \quad \beta = 2\pi n_1 \frac{d}{\lambda} \cos \Phi_t = 2\pi \frac{d}{\lambda} \sqrt{n_1^2 - n_0^2 \sin^2 \Phi_i},$$

taking into account that beam wavelength is  $\lambda$  and the thickness is  $d$ .

In the GATR technique where a beam passes from a more dense medium of Ge crystal (with a refractive index  $n_1$ ) through a less dense medium of a thin film ( $n_2$ ) and to a more dense substrate ( $n_3$ ), the reflectance is written as:

$$(5) \quad \rho^P = \frac{r_{12}^P + r_{23}^P \exp\left(4\pi i k d \sqrt{n_2^2 - n_1^2 \sin^2 \Phi_i}\right)}{1 + r_{12}^P r_{23}^P \exp\left(4\pi i k d \sqrt{n_2^2 - n_1^2 \sin^2 \Phi_i}\right)},$$

where  $P$  means polarization of incident light,  $r_{12}^P$  and  $r_{23}^P$  are Fresnel amplitude coefficients for interfaces from medium with  $n_1$  to medium with  $n_3$ ,  $k$  is the wavenumber ( $k = 1/\lambda$ ) and  $\Phi_i$  is the angle of incident beam [22].

The directly measured values in spectroscopic ellipsometry are  $\Psi$  and  $\Delta$  related to ellipsometric parameter taken from Eq. (1):

$$(6) \quad \rho \equiv \frac{r_p}{r_s} = \tan(\Psi) \cdot \exp(i\Delta) = f(\varepsilon_1, \varepsilon_2, d).$$

The ellipsometric parameters  $\Psi(\lambda)$  and  $\Delta(\lambda)$  measured as a function of incidence wavelength ( $\lambda$ ) and incidence angle ( $\alpha$ ) relative to the surface normal in Eq. (6) are related to the Fresnel complex reflection coefficients  $r_p$  and  $r_s$  for  $p$ - and  $s$ -polarized light. On the other hand, they are considered as a function of complex dielectric constants  $\varepsilon_1$  and  $i\varepsilon_2$ , and thickness  $d$  of a thin film. Its exceptional sensitivity is derived from a phase change of the reflected light contained in the parameter  $\Delta$ . The amplitude ratio of the complex reflection coefficients is contained in  $\tan(\Psi)$ . When the ellipsometrically analyzed material is built from few layers of different components, the analysis requires use of several theoretical models. Thus the roughness of the film surface is included in effective medium approximation (EMA) model.

Semiconductors below a fundamental bandgap can be described with simple Cauchy model which assumes one oscillator [33]. Some materials, depending on their orientation and symmetry, require more complex descriptions as general oscillator (GenOsc) model which consists of many functions (i.e. Gauss, Lorentz, etc.) and different oscillations. In EMA the effective optical constants are calculated from optical constants and volume fractions ( $f$ ) of the constituent materials in the composite surface. The Bruggeman EMA used in this model is defined by:

$$(7) \quad f_{\text{PEN}} \frac{\varepsilon_{\text{PEN}} - \varepsilon}{\varepsilon_{\text{PEN}} + 2\varepsilon} + f_{\text{void}} \frac{\varepsilon_{\text{void}} - \varepsilon}{\varepsilon_{\text{void}} + 2\varepsilon} = 0,$$

where  $f_{\text{PEN}}$  and  $f_{\text{void}}$  are the volume fractions of pentacene and void, respectively,  $\varepsilon_{\text{PEN}}$  is the pentacene dielectric function, and  $\varepsilon$  is the EMA layer function.

The simplest modelling of anisotropic thin film on a substrate can be done by Cauchy model. In a less simple situations, as in our case, adding to Cauchy model a Biaxial layer is needed with uniaxial anisotropy type and specifying optical constants with two Cauchy “dummy” dispersion relations. Both dummy layers are coupled to the Biaxial layer what allows the optical constants to vary within these layers. In order to improve the modelling of data GenOsc model can be employed. In this model contributions from a large variety of oscillators is allowed. The GenOsc layer is built from Cauchy layer defined at the beginning. GenOsc layer can consist of many different functions, an example of a simple sum including Lorentz oscillator is shown below:

$$(8) \quad \varepsilon(E) \equiv \varepsilon_1 + i\varepsilon_2 = \varepsilon_0 + \frac{A_1}{E_1^2 - E^2} + \frac{A_1}{E_1^2 - E^2} + \frac{A_2}{E_2^2 - E^2 - iB_2E},$$

where  $\varepsilon(E)$  is the complex dielectric function as a function of photon energy  $E$  and the first term  $\varepsilon_0$  is the offset parameter. The second and the third terms are Pole (or Sellmeier) terms, and the last one is the Lorentz oscillator term. The imaginary part of this complex function models a Lorentzian absorption and the real part is its Kramers-Kronig transform. The Pole (Sellmeier) [34] terms are two zero-width Lorentz oscillators simulating the dispersion in  $\varepsilon_1$  created by absorption that occurs outside the measured spectral range of the model. The Lorentzian oscillator models electron-vibrational progression already successfully applied in deconvolution of the visible absorption spectrum (Fig. 3b). Having the polarizability ( $\alpha$ ) as an energy-dependent function for a single atom  $n$ :

$$(9) \quad \alpha_n(E) = \frac{e^2}{m_e} \frac{1}{(E_n^2 - E^2) - i\Gamma_n E},$$

where  $e$  is the electron charge,  $m_e$  – the electron mass,  $\Gamma$  is the broadening of the oscillator, the DF is given through the polarizability  $\alpha(E)$  as follows [35]:

$$(10) \quad \varepsilon(E) \equiv \varepsilon_1 + i\varepsilon_2 = \varepsilon_0 + \sum \frac{A_n}{(E_n^2 - E^2) - i\Gamma_n E},$$

where  $\varepsilon(E)$  is the complex dielectric function as a function of photon energy  $E$  with

the maximum energy position at  $E_n$ , and  $\varepsilon_0$  is the additional offset parameter.  $A_n$  is the amplitude of the  $n^{\text{th}}$  oscillator defined as:

$$(11) \quad A_n = \frac{Ne^2}{\varepsilon_0 m_e} f_n,$$

where  $N$  is the number of atoms,  $f_n$  is the oscillator strength which measures the relative probability of a quantum mechanical transition. For free atoms it satisfies a sum rule  $\sum_n f_n = 1$ .

## 4. Results and discussion

### 4.1. AFM examinations

Morphological features of a vacuum deposited pentacene film on Si/SiO<sub>2</sub> substrate were observed using tapping mode of AFM in a height and amplitude contrast. The height resolution of AFM allows identification of the growth mode. Pentacene is known to grow on SiO<sub>2</sub> in the Stranski-Krastanov mode as a thin film phase, forming 3D dendritic islands with 2D layers between them [14, 21, 36]. Above a critical thickness the islands transform into larger crystallites of a flattened globular shape. This growth model is called the Vollmer-Weber 3D islands mode. Fig. 2 shows a representative AFM image of the surface height profile of 32-nm-thick pentacene film grown on amorphous SiO<sub>2</sub> substrate with discernible crystalline grains of globular shape. The shapes observable under higher resolution are not spherical but strongly flattened. The lateral dimensions of the grains are 180–380 nm, with 16 nm-heights and  $R_{RMS}$  roughness of 4.3 nm. An example of a single grain is shown in inset of Fig. 2. The resolution of our AFM measurements allowed inspection of the grains down as much as to 10–11 monolayers assuming that the length of single pentacene molecule is 1.62 nm. We do not observe individual pentacene layers ordered in a well visible flattened terraces, such observations require better resolutions, especially prepared AFM tip, low temperature and *in situ* measurements [37, 38]. For the thickness studied here the pentacene molecules crystalize in orthorhombic phase with the tilt angle of 12–14° with respect to the substrate normal [1, 11].

The grain size determines its surface area to volume ratio. The smaller the grains are, the more the surface effect influences the properties of pentacene layer. The distribution of surface potential in organic-semiconductor/insulator interface region is very important for OFETs operation and has significant implications for charge mobility [9] and electrical transport mechanism [25]. It was already reported that larger grains with improved mobility could be obtained by reducing the surface roughness or by modifying the conditions of pentacene deposition such as deposition rate, substrate temperature, or post deposition annealing [39, 40]. Our measurements clearly indicate that the 32-nm-thick sample has larger and more homogeneous grains than thicker sample [29] and thus would be more efficient in terms of electron mobility.

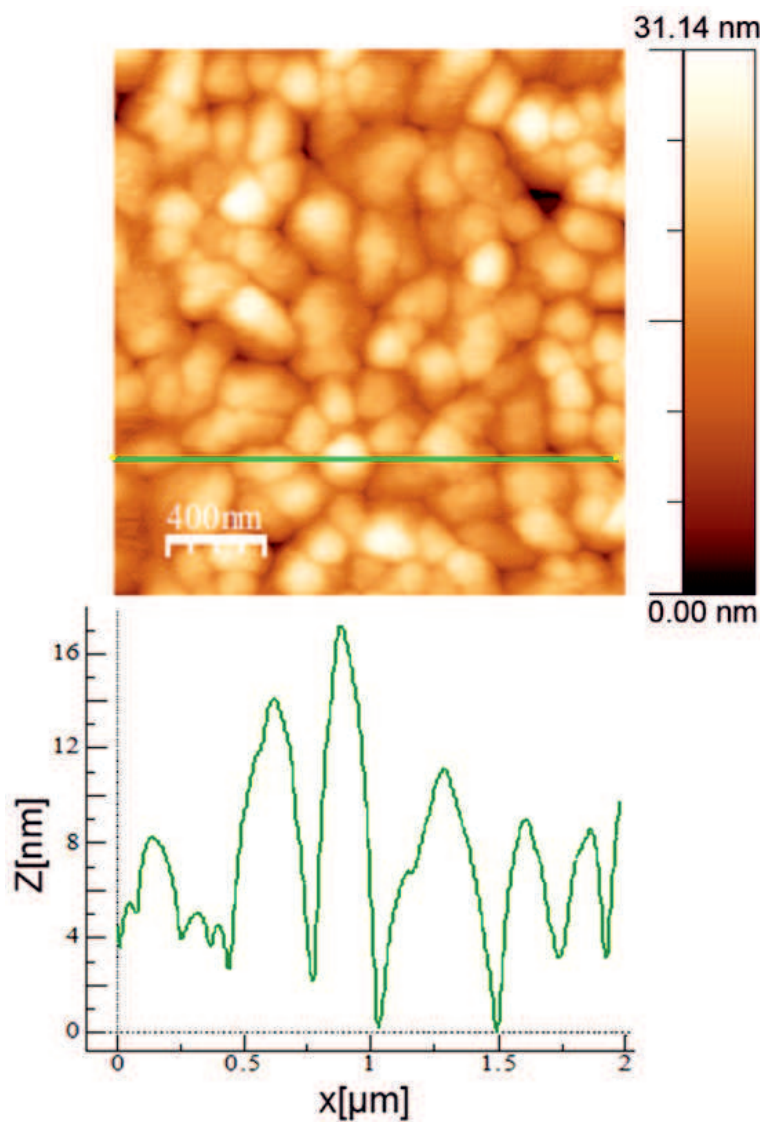


Fig. 2: AFM image and height profile of 32 nm pentacene film deposited on Si/SiO<sub>2</sub> substrate. Pentacene forms flattened globular crystallites. The morphology of globules is shown in the inset. The scan size was 2 μm.

#### 4.2. Optical properties

The purpose of our studies was to demonstrate how anisotropy and well defined molecular ordering of PEN affect the optical and electronic properties which are important in understanding the performance of organic photoactive devices. The

examination has been carried out using absorption spectroscopy and spectroscopic ellipsometry. The sample deposited on fused silica shows uniaxial alignment with a symmetry axis perpendicular to the surface, as it was established in literature [41]. Indeed, in polarizing microscope with crossed polarizers, the total extinction was observed independent of the azimuthal direction of the film. Vibronic progression in the UV-VIS spectrum is directly connected with IR internal vibrations in  $\pi$ -conjugated molecular solids by vibronic coupling. UV-VIS absorption spectra of evaporated PEN thin films on fused silica are similar to the previously reported (Fig. 3) [44, 46, 48–50]. The energy spacing in vibronic progression between subsequent maxima starting from the low energy peak is 1406, 1327 and 1338  $\text{cm}^{-1}$ , respectively. These wavenumbers match up with oscillating frequencies of PEN ring breathing vibrations discussed in previous section. The lowest absorption band in the solid state for the film at 14976  $\text{cm}^{-1}$  is red shifted as compared to that one in solution due to Coulombic and exchange interactions, and shows Davydov splitting ( $\Delta D$ ) reflecting interactions between molecules having different site symmetries [10, 25]. The red shift exhibits the value of 2421  $\text{cm}^{-1}$  with respect to the position in hot toluene (60° C) while the band splitting of  $\Delta D = 790 \text{ cm}^{-1}$  is smaller with respect to that in single crystal phase [41]. This lower value could indicate reduced intermolecular interactions, due to a lower molecular-orbital overlapping between molecules that might be attributed to less ordered “thin-film phase” and/or some structural defects in our vacuum deposited sample observed for thicker samples [11]. The level of molecular ordering is significant also for collective interactions or exchange interactions between translationally equivalent molecules and usually manifests itself in the broad absorption tail. In the film on (Fig. 3, curve 2) the broad tail is hardly seen which suggests relatively low molecular ordering.

Ellipsometric psi  $\Psi$  and delta  $\Delta$  angles were measured over the range of 260–1300 nm, at four incident angles from 45° to 75° in steps of 10°, taking 20 analyzer revolutions for averaging of each measurement point signal. SE spectra were analyzed by model calculations consisting of a stack of dielectric layers: Si substrate, native silicon oxide of thickness 1.5 nm, deposited pentacene, and a layer modeling surface roughness. The surface layer effective optical constants, according to the morphological AFM characterization, were modeled using EMA as a physical mixture of 50% of pentacene under layer and 50% of voids (air). The thickness of the surface roughness layer, which was calculated from fitting of multilayer model to ellipsometric data, was 5.9 nm. Similar value was observed for surface roughness measured by AFM ( $R_{RMS}$ ), although the calculated roughness from modeling of SE data is higher. The difference may reflect the well known fact that the apparent depth measured by AFM arises from the penetration of the tip into the grain boundary, which gives, due to a tip geometry, underestimation of the grain thickness. The thickness of the pentacene layer was determined in a transparent range of the spectrum between 0.95 and 1.45 eV using uniaxial parameterized Cauchy model. Even at this simplified case, the attempts to apply the isotropic model failed, giving poor fit to the experimental



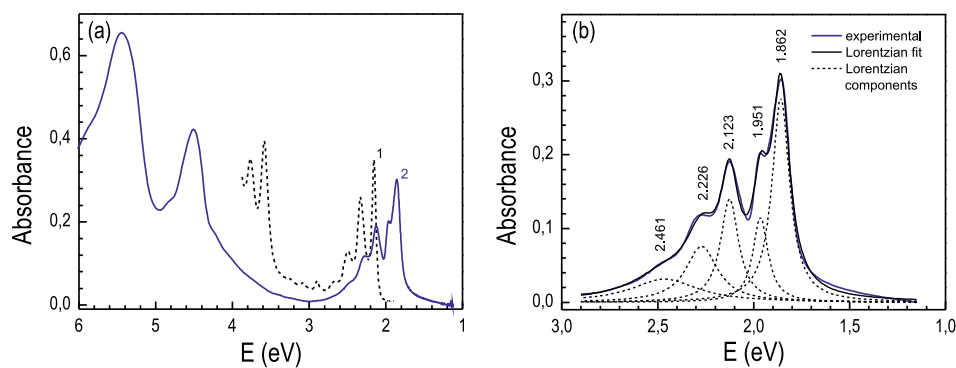


Fig. 3: (a) UV-VIS absorption spectra of pentacene dissolved in hot toluene (60°C) (dashed line 1) and for thin film deposited on fused silica substrate (solid line 2). (b) Fit of Lorentz model oscillators to the experimental spectrum of the solid film of spectrum (2) from part (a).

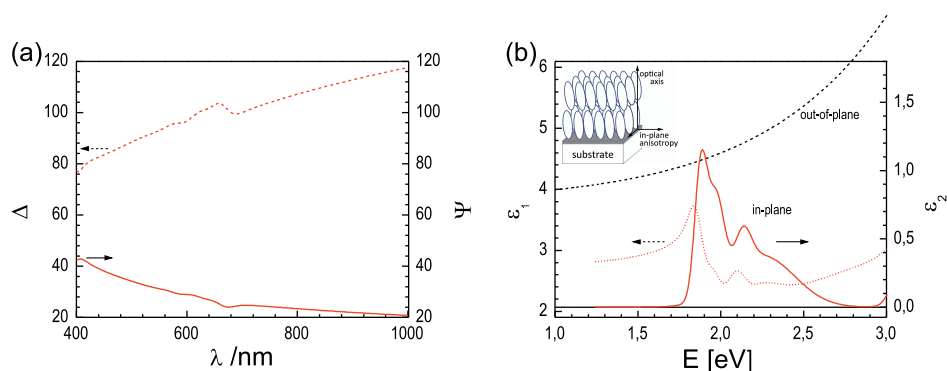


Fig. 4: (a) SE data collected at angle of incidence 65° for thin film. The dashed and solid lines represent respectively  $\Delta$  and  $\Psi$ . (b) Dielectric functions for the in-plane (in red) and normal to the plane (in black) components of PEN film. The dashed and continues lines represent respectively real ( $\epsilon_1$ ) and imaginary part ( $\epsilon_2$ ) of dielectric function.

data with distinctly higher mean square error (MSE) values than for uniaxial one. In the energy range of 1–3 eV the experimental data were calculated using a model of complex dielectric functions (DF) which describes electronic properties of pentacene in terms of electronic polarizability and intrinsic vibrations of a skeleton due to the vibronic coupling. We use GenOsc model with Lorentzian oscillator to model electron-vibrational progression already successfully applied in deconvolution of the visible absorption spectrum (Fig. 3b). Upon a fitting of the Lorentzian model with the ellipsometric parameters  $\Psi(\lambda)$  and  $\Delta(\lambda)$  for 100-nm-thick sample (not shown)

in-plane and out-of-plane DF components were calculated (Fig. 4). A significant difference between these components is observed. While for the in-plane component the shape of the dielectric function shows five optical transitions with values 1.879, 1.970, 2.134, 2.248  $\text{cm}^{-1}$ , which are in agreement with previously reported [13, 42], the perpendicular one is featureless within the measured spectral range (Fig. 4b). Under our experimental conditions absorption for the perpendicular component of DF is probably small and is approximated by the fitting algorithm to zero. Consequently, the refractive index decreases monotonically with the energy. This finding is in agreement with the transition moment being polarized along the short  $z$ -axis and the orientation of PEN molecules on native silica being close to the surface normal (explained in the subsection 4.3). Note, that the real part  $\varepsilon_1$  of DF is consistent with Kramers-Kronig imaginary counterparts  $\varepsilon_2$  in the uniaxial ellipsometric model. A similar smaller red shift of the exciton band as for UV-VIS absorption is observed (Fig. 4). The four low-lying excitonic bands give the Davydov splitting as low as  $\Delta D = 734 \text{ cm}^{-1}$ .

### 4.3. Grazing angle ATR infrared spectroscopy

The average orientation of PEN molecules in the layer can be precisely deduced from X-ray diffraction pattern. However in this work, we have applied a polarized grazing angle method already successfully applied to thin polymeric film on Si substrate [23]. At first, the assignment of the infrared vibrations obtained in GATR measurements in non-polarized light for the vacuum evaporated PEN sample of 32-nm was performed by comparison with PEN microcrystalline powder detected by diamond-ATR technique (Fig. 5). As can be noted all vibrations recorded by GATR are observed in the ATR spectra, however, some bands are attenuated and other amplified. It suggests a change in order or/and interaction between molecules in the deposited thin film comparing to the powdered polycrystalline sample (Table 1). The first one is anisotropic with uniaxially distributed molecules on Si/SiO<sub>2</sub> surface (*vide infra*) whereas the other is composed of randomly oriented microcrystals. Our findings of vibrations in deposited film using GATR measurements agree with other experimental works for crystalline pentacene samples and thin films as well as with the computations with the *B3LYP DFT* level of calculations [17, 18, 20, 43, 44]. The positions of the most intense IR peaks with defined vibration modes are marked in Fig. 5 and collected in Table 1.

The analysis of molecular ordering in anisotropic samples with spectroscopic methods requires knowledge of polarization of each transition moment within molecular framework. Crystalline pentacene is a polyaromatic hydrocarbon molecule consisting of five fused benzene rings in a rod-like order. It belongs to the  $D_{2h}$  symmetry point group [45] specifying 43 infrared active vibrational modes which are assigned to three irreducible representations  $B_{1u}$  (17),  $B_{2u}$  (17) and  $B_{3u}$  (9) with polarization directions of IR transitions along the  $z$ ,  $y$  and  $x$  molecular axes, respectively (inset in Fig. 6a) [18]. In the GATR measurements with  $s$ - and  $p$ -polarized IR radiation

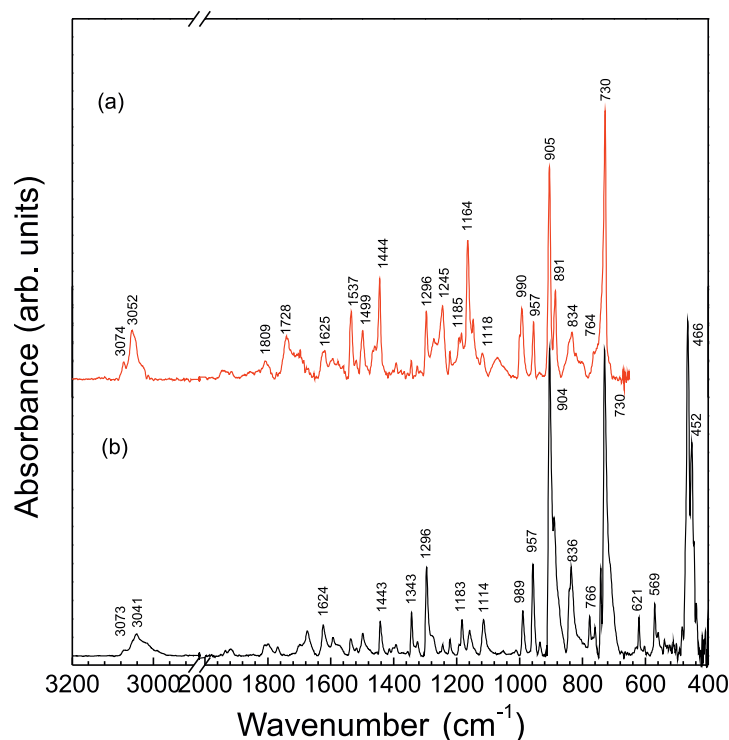


Fig. 5: Comparison of the infrared spectra of pentacene thin film and pentacene powder. The upper curve (a) shows grazing angle GATR spectrum of pentacene measured with non-polarized light at the incidence angle of 63°. The lower curve (b) presents the ATR spectrum of pentacene powder (recorded with a non-polarized light at the incidence angle of 45°). Relative peak intensities for the samples are different due to molecular orientation.

only those modes are observed which have non-zero components of transition dipole moments parallel or perpendicular to the surface [22]. Indeed, the both spectra of deposited film in the sandwich configuration Ge/PEN/SiO<sub>2</sub>/Si are significantly different, while maintaining the peak position (Fig. 6a and b). Inset in Fig. 6b shows a scheme of geometry of the GATR accessory with a Ge crystal as an optical element. In the *p*-polarized spectrum the bands with a perpendicular dipole component to the Si surface are more enhanced than the vibrations with a parallel component [22]. Analogously, for the *s*-polarized light only the vibrations parallel to the substrate are excited and have distinguished intensity [31, 46].

Transmission spectra of PEN provide additional useful information on molecular orientation on Si/SiO<sub>2</sub> surface (Fig. 6c). For light at normal incidence, unpolarized IR beam excites only the vibrational modes having transition dipole components parallel to the substrate surface. In parts c and b of Fig. 6 the transmission spec-

Tab. 1: Comparison between the experimental major frequencies ( $\text{cm}^{-1}$ ) and relative intensities  $A_p/A_s$  of the IR bands for pentacene powder and thin film on Si/SiO<sub>2</sub> substrate measured in ATR, transmission, and GATR configuration geometry.

Mode <sup>a-d</sup>	Polarization <sup>e</sup>	Frequency (relative intensity) <sup>f</sup>						Intensity ratio A <sub>p</sub> /A <sub>s</sub>
		Powder ATR (unpol.)		film transmission		film GATR (unpol.)		
CH o.p. bend	<i>x</i>	730	(1.00)	731	(0.66)	730	(1.26)	(0.61)
CH o.p.	<i>z</i>	836	(0.289)	838	(0.09)	834	(0.22)	(0.6)
CH o.p. bend	<i>x</i>	905	(1.00)	905	(1.00)	905	(1.00)	(0.65)
CH o.p. bend	<i>x</i>	957	(0.298)	957	(0.13)	957	(0.27)	(0.6)
CH o.p.	<i>y</i>	990	(0.15)			990	(0.33)	(16.8)
	<i>z</i>	1114	(0.117)			1118	(0.13)	(-)
CH i.p.	<i>y</i>	1158	(0.081)			1164	(0.65)	(10.1)
CH i.p.	<i>z</i> ( <i>y</i> <sup>g</sup> )	1183	(0.114)			1184	(0.21)	(2.5)
CH i.p.	<i>y</i>	1221	(0.051)			1221	(0.13)	(5.4)
CC str.	<i>z</i>	1295	(0.286)	1297	(0.18)	1296	(0.32)	(1.3)
	<i>y</i>	1324	(0.042)			1324	(0.05)	(5.3)
CC str.	<i>z</i>	1343	(0.138)	1344	(0.04)	1343	(0.08)	(2.4)
CC str.	<i>y</i>	1393	(0.036)			1392	(0.01)	(12.3)
CC str.	<i>y</i>	1443	(0.114)			1444	(0.47)	(10.0)
CC str.	<i>y</i>	1498	(0.024)			1499	(0.23)	(13.4)
	<i>z</i>	1518	(0.008)			1518	(0.08)	(-)
	<i>y</i>	1536	(0.024)			1537	(0.32)	(10.5)
CC str.	<i>z</i>	1593	(0.06)			1593	(0.14)	(3.3)
CC str.	<i>z</i>	1624	(0.01)			1625	(0.13)	(2.7)
CH str.	<i>y</i>	3041	(0.072)			3052	(0.23)	(2.3)
CH str.	<i>y</i>	3073	(0.018)			3074	(0.01)	(3.1)

o.p. – out-of-plane; i.p. – in-plane vibrations.

<sup>a</sup> Ref. [16]; <sup>b</sup> Ref. [19]; <sup>c</sup> Ref. [17]; <sup>d</sup> Ref. [18].

<sup>e</sup> Symmetry assigned from *B3LYP* calculations [18].

<sup>f</sup> Intensities relative to 905  $\text{cm}^{-1}$  band.

<sup>g</sup> Assignment proposed in this work.

trum is compared with the  $s$ -polarized GATR spectrum. The most intense bands are at 730, 836, 860, 904, 955, 1296 and 1344  $\text{cm}^{-1}$  which are assigned to the in-plane vibrations of  $B_{1u}$  symmetry ( $z$ -polarized) or out-of-plane vibrations of  $B_{3u}$  symmetry ( $x$ -polarized). These modes have their transition dipoles aligned normal to the long molecular axis and the most intense modes are simultaneously observed in the transmission spectrum. This finding strongly suggests that the pentacene molecules

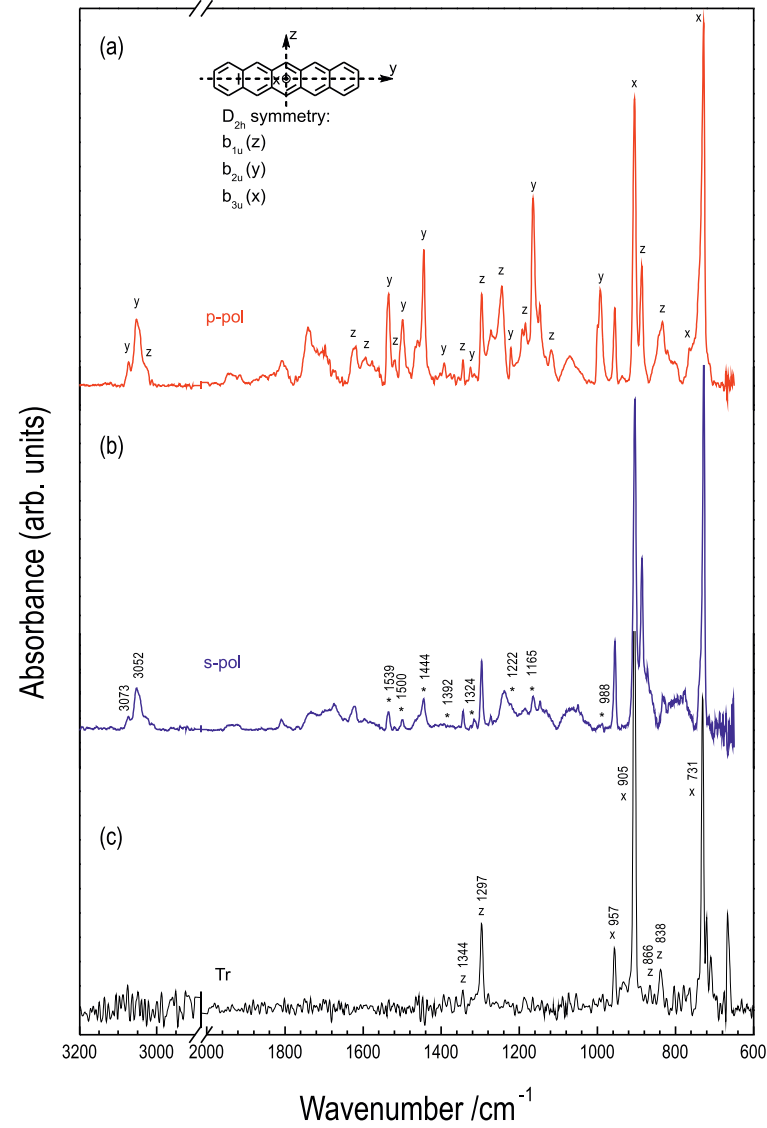


Fig. 6: Comparison of the polarized GATR and transmission spectra of 32-nm thick pentacene film on Si/SiO<sub>2</sub>. Upper curve (a) presents the *p*-polarized GATR spectrum with assignment of transition moment directions of individual bands to *x*, *y* and *z* molecular axes indicated in the formula [18]. (b) *s*-polarized GATR spectrum. Selected bands marked with an asterisk are associated with the *y*-polarized transitions and are remarkably attenuated as compared to the spectrum in (a). (c) common transmission spectrum of pentacene thin film.

are standing more or less perpendicularly to the  $\text{SiO}_2$  substrate.

In the analyzed wavenumber region ( $4000\text{--}600\text{ cm}^{-1}$ ) all vibrational modes, i.e. stretching, in-plane and out-of-plane deformation vibrations are observed in the spectrum measured with the  $p$ -polarized IR beam (Fig. 6a) [27, 43, 44, 47]. However, as was mentioned before, some bands at  $730$ ,  $904$ ,  $955\text{ cm}^{-1}$  gain their intensity in the  $s$ -polarized spectrum (Fig. 6b), while other vibrations with maxima at  $988$ ,  $1165$ ,  $1222$ ,  $1324$ ,  $1392$ ,  $1500$ , and  $1539\text{ cm}^{-1}$  (assigned with asterisk in Fig. 6b) are significantly reduced. These vibrations are associated with the  $B_{2u}$  symmetry ( $y$ -polarized) and are intense in the  $p$ -polarized spectrum. Unfortunately it is not possible to determine an average transition moment orientation with respect to the surface and hence the molecular order, using the ratio of peak intensities  $A_p$  and  $A_s$  measured in the  $p$ -polarized and  $s$ -polarized absorption spectrum. In the sandwiched geometry of GATR technique the electric field strength perpendicular to the Ge surface is enhanced within the film [22] and introduces strengthening of the  $p$ -polarized component relatively to the  $s$ -polarized one. Thus the orientation of pentacene molecules extracted from the polarized GATR spectra is overestimated and gives values deviating from a perpendicular orientation by the angle as low as  $\sim 7^\circ$ . On the other hand one can estimate a degree of orientation measured as the ratio of  $A_p/A_s$  taking into account the symmetry of transition moments.

Previous experimental verification of computed vibrational modes was based only on the most intense peaks extracted from the spectra provided by reflection-absorption infrared (RAIRS) method [18], polarized multiple internal reflection [20, 31], and transmission spectra [18, 46] where the low intensity peaks were out of detection limit. In the GATR spectra most of the assignments corresponds to the calculated ones [18]. However, the vibration at  $1184\text{ cm}^{-1}$  reported as  $B_{1u}$  type, according to its GATR dichroism is polarized along the long axis. We are aware that this change should be accompanied by reassignment of another band of previous  $B_{2u}$  symmetry for which the polarization assignment must be also changed and which is predicted by quantum mechanical calculations [12]. Though any of additional reassignment cannot be done unambiguously in the analyzed spectral range ( $4000\text{--}600\text{ cm}^{-1}$ ), this vibration may be located in the far IR spectral range. Moreover two assignments at  $764$  and  $1245\text{ cm}^{-1}$  (Fig. 5) are not predicted by calculations, but mentioned in [17].

## 5. Conclusions

We have investigated optical and structural properties of 32-nm pentacene films grown by OMBD on native  $\text{SiO}_2$  and fused silica substrates using spectroscopic ellipsometry and polarized GATR infrared spectroscopy with complementary UV-VIS absorption, and AFM microscopy. The thickness was selected to obtain orthorhombic phase which exists when the thickness level is below 30 nm [11]. Pentacene molecules within this phase are oriented almost perpendicularly to the substrate surface. The

surface morphology obtained from the AFM measurements consists of grainy crystallites of different average sizes. The sample shows grain sizes of 180–380 nm. In the ellipsometric analysis the GenOsc model with Lorentzian oscillator was used as the one which reflects the shape of the experimental spectra in the finest way. On this basis two perpendicular components of dielectric function in uniaxially oriented sample were calculated. The in-plane component agrees fully with other works, while the perpendicular component is featureless. This finding is in agreement with the  $z$ -axis polarization of the lowest transition and perpendicular orientation of pentacene on native silica. We have demonstrated the utility of the IR GATR technique in the analysis of organization and optical properties of uniaxially oriented organic thin films. The orientation of pentacene molecules extracted from vibrational modes of polarized GATR points out that the molecules, in the thin film are standing almost perpendicular to the SiO<sub>2</sub> substrate.

## References

- [1] C. D. Dimitrakopoulos and P. R. L. Malenfant, *Advanced Materials* **14** (2002), 99.
- [2] S. A. DiBenedetto, A. Facchetti, M. A. Ratner, and T. J. Marks, *Advanced Materials* **21** (2009), 1407.
- [3] J. A. Venables, J. L. Seguin, J. Suzanne, and M. Bienfait, *Surface Science* **145** (1984), 345.
- [4] B. P. G. Rosenfeld, and G. Comsa, *The Chemical Physics of Solid Surfaces*, Elsevier, Amsterdam 1997.
- [5] C. Ratsch, A. Zangwill, P. Smilauer, and D. D. Vvedensky, *Physical Review Letters* **72** (1994), 3194.
- [6] S. Kowarik, A. Gerlach, and F. Schreiber, *Journal of Physics-Condensed Matter* **20** (2008), 184005.
- [7] A. Rao, M. W. B. Wilson, J. M. Hodgkiss, S. Albert-Seifried, H. Bässler, and R. Friend, *Journal of the American Chemical Society* **132** (2010), 12698.
- [8] S. E. Fritz, S. M. Martin, C. D. Frisbie, M. D. Ward, and M. F. Toney, *Journal of the American Chemical Society* **126** (2004), 4084.
- [9] S. E. Fritz, T. W. Kelley, and C. D. Frisbie, *The Journal of Physical Chemistry B* **109** (2005), 10574.
- [10] D. Qi, H. Su, M. Bastjan, O. D. Jurchescu, T. M. Palstra, A. T. S. Wee, M. Rübhausen, and A. Rusydi, *Applied Physics Letters* **103** (2013), 113303.
- [11] H. L. Cheng, Y. S. Mai, W. Y. Chou, L. R. Chang, X. W. Liang, *Advanced Functional Materials* **17** (2007), 3639.
- [12] T. Breuer, M. A. Celik, P. Jakob, R. Tonner, and G. Witte, *The Journal of Physical Chemistry C* **116** (2012), 14491.
- [13] S. H. Han, S. Yoo, B. Kippelen, and D. Levi, *Appl. Phys. B* **104** (2011), 139.
- [14] R. Ruiz, D. Choudhary, B. Nickel, T. Toccoli, K.-C. Chang, A. C. Mayer, P. Clancy, J. M. Blakely, R. L. Headrick, S. Iannotta, and G. G. Malliaras, *Chemistry of Materials* **16** (2004), 4497.
- [15] D. K. Rai, D. Datta, S. K. Ram, S. Sarkar, R. Gupta, and S. Kumar, *Solid State Sciences* **12** (2010), 1449.

- [16] J. Szczepanski, C. Wehlburg, and M. Vala, *Chemical Physics Letters* **232** (1995), 221.
- [17] K. H. Michaelian, Q. Wen, B. E. Billingham, J. M. Shaw, and V. Lastovka, *Vibrational Spectroscopy* **58** (2012), 50.
- [18] D. Ross and R. Aroca, *The Journal of Chemical Physics* **117** (2002), 8095.
- [19] D. M. Hudgins and S. A. Sandford, *The Journal of Physical Chemistry A* **102** (1998), 344.
- [20] Y. Hosoi, K. Okamura, Y. Kimura, H. Ishii, and M. Niwano, *Applied Surface Science* **244** (2005), 607.
- [21] R. Ruiz, B. Nickel, N. Koch, L. Feldman, R. Haglund, A. Kahn, G. Scoles, *Physical Review B* **67** (2003), 125406.
- [22] M. Milosevic, S. L. Berets, and A. Y. Fadeev, *Applied Spectroscopy* **57** (2003), 724.
- [23] M. Milosevic, *Internal Reflection and ATR Spectroscopy*, Wiley, 2012.
- [24] W. S. Hu, Y. T. Tao, Y. J. Hsu, D. H. Wei, and Y. S. Wu, *Langmuir* **21** (2005), 2260.
- [25] H. Yoshida and N. Sato, *Applied Physics Letters* **89** (2006), 101919.
- [26] C. C. Mattheus, G. A. de Wijs, R. A. de Groot, and T. T. M. Palstra, *Journal of the American Chemical Society* **125** (2003), 6323.
- [27] M. Schubert, C. Bundesmann, G. Jacopic, H. Maresch, and H. Arwin, *Applied Physics Letters* **84** (2004), 200.
- [28] V. Coropceanu, M. Malagoli, D. A. da Silva, N. E. Gruhn, T. G. Bill, and J. L. Bredas, *Physical Review Letters* **89** (2002), 275503.
- [29] E. Z. Frątczak, P. Uznański, and M. E. Moneta, *Chemical Physics* **456** (2015), 49.
- [30] R. M. A. Azzam and N. M. Bashara, *Ellipsometry and Polarized Light*, 1st edn., North-Holland, Amsterdam 1977.
- [31] T. Lummerstorfer, J. Kattner, and H. Hoffmann, *Analytical and Bioanalytical Chemistry* **388** (2007), 55.
- [32] I. Horcas, R. Fernandez, J. M. Gomez-Rodriguez, J. Colchero, J. Gomez-Herrero, and A. M. Baro, *Review of Scientific Instruments* **78** (2007), 013705.
- [33] A. L. Cauchy, *Bulletin des Sciences Mathématiques* **14**, no. 9 (1836).
- [34] W. Sellmeier, *Annalen der Physik und Chemie* **219** (1871), 272.
- [35] D. Datta and S. Kumar, *Solar Energy Materials and Solar Cells* **94** (2010), 420.
- [36] K. Puntambekar, J. Dong, G. Haugstad, and C. D. Frisbie, *Advanced Functional Materials* **16** (2006), 879.
- [37] L. Gross, F. Mohn, N. Moll, P. Liljeroth, and G. Meyer, *Science* **325** (2009), 1110.
- [38] S. Steudel, S. De Vusser, S. De Jonge, D. Janssen, S. Verlaak, J. Genoe, and P. Heremans, *Applied Physics Letters* **85** (2004), 4400.
- [39] D. Knipp, R. A. Street, A. Volkel, and J. Ho, *Journal of Applied Physics* **93** (2003), 347.
- [40] S. J. Kang, M. Noh, D. S. Park, H. J. Kim, C. N. Whang, and C. H. Chang, *Journal of Applied Physics* **95** (2004), 2293.
- [41] O. Ostroverkhova, S. Shcherbyna, D. Cooke, R. Egerton, F. Hegmann, R. Tykwinski, S. R. Parkin, and J. E. Anthony, *Journal of Applied Physics* **98** (2005), 033701.
- [42] S. P. Park, S. S. Kim, J. H. Kim, C. N. Whang, and S. Im, *Applied Physics Letters* **80** (2002), 2872.
- [43] S. R. Langhoff, *Journal of Physical Chemistry* **100** (1996), 2819.
- [44] E. Heinecke, D. Hartmann, R. Muller, and A. Hese, *Journal of Chemical Physics* **109** (1998), 906.



- [45] R. B. Campbell, J. Trotter, and J. Monteath, *Acta Crystallographica* **15** (1962), 289.
- [46] T. M. Halasinski, D. M. Hudgins, F. Salama, L. J. Allamandola, and T. Bally, *Journal of Physical Chemistry A* **104** (2000), 7484.
- [47] A. L. Deman, M. Erouel, D. Lallemand, M. Phaner-Goutorbe, P. Lang, and J. Tardy, *Journal of Non-Crystalline Solids* **354** (2008), 1598.
- [48] A. Afzali, C. D. Dimitrakopoulos, and T. L. Breen, *Journal of the American Chemical Society* **124** (2002), 8812.
- [49] D. Faltermeier, B. Gompf, M. Dressel, A. K. Tripathi, and J. Pflaum, *Physical Review B* **74** (2006), 125416.
- [50] S. Koestler, A. Rudorfer, A. Haase, V. Satzinger, G. Jakopic, and V. Ribitsch, *Advanced Materials* **21** (2009), 2505.

Department of Solid State Physics  
Faculty of Physics and Applied Informatics  
University of Łódź  
Pomorska 149/153, PL-90-236 Łódź  
Poland  
e-mail: ewelinazofia@gmail.com

Centre of Molecular and Macromolecular  
Studies  
Polish Academy of Sciences  
Sienkiewicza 112, PL-90-132 Łódź  
Poland  
e-mail: puznansk@cbmm.lodz.pl

Presented by Marek Moneta at the Session of the Mathematical-Physical Commission of the Łódź Society of Sciences and Arts on September 10, 2015

## ORGANIZACJA MOLEKULARNA W WARSTWIE PENTACENU OSADZONEJ NA POWIERZCHNI SiO<sub>2</sub> PRZEBADANA ELIPSOMETRIĄ, SPEKTROSKOPIĄ PODCZERWIENI I MIKROSKOPIĄ SIŁ ATOMOWYCH

### Streszczenie

W artykule zostały opisane cienkie warstwy pentacenu o grubości 32 nm uzyskane metodą osadzania z organicznej wiązki molekularnej (OMBD) w warunkach wysokiej próżni na podłożach naturalnie utlenionego krzemu (Si/SiO<sub>2</sub>) i termicznie uzyskanej krzemionki. Zostały przebadane optyczne własności anizotropowe, uporządkowanie molekul w warstwach i morfologia próbek metodami elipsometrii spektroskopowej o zmiennym kącie padania wiązki (VASE), absorpcji UV-VIS, techniki transmisji w podczerwieni (IR) i techniki osłabionego całkowitego wewnętrznego odbicia dla kąta ślizgowego wiązki spolaryzowanej (GATR), oraz mikroskopii sił atomowych (AFM).

Zostało również omówione przypisanie symetrii poszczególnym przejściom wibronowym molekul pentacenu tworzących warstwę. Warstwy wykazują teksturę ciągłą o jednoosiowym uporządkowaniu molekul i silnie anizotropowych własnościach optycznych co wykazały pomiary elipsometryczne.

Po raz pierwszy dichroiczne widma GATR IR zostały wykonane dla cienkich warstw i wnioski dotyczące orientacji molekul pentacenu zostały wydedukowane na podstawie stosunku dichroicznego drgań aktywnych w zakresie widma podczerwieni.

*Słowa kluczowe:* pentacen, własności optyczne, orientacja molekularna, elipsometria, spektroskopia podczerwieni, mikroskopia sił atomowych

## B U L L E T I N

DE LA SOCIÉTÉ DES SCIENCES ET DES LETTRES DE ŁÓDŹ

2016

Vol. LXVI

Recherches sur les déformations

no. 1

pp. 123–133

*Contribution to the jubilee volume, dedicated  
to Professors J. Lawrynowicz and L. Wojtczak  
on the splendid occasion of the 50th anniversary  
of their scientific activity*

Małgorzata Nowak-Kępczyk

# AN ALGEBRA GOVERNING REDUCTION OF QUATERNARY STRUCTURES TO TERNARY STRUCTURES III

A STUDY OF GENERATORS OF THE RESULTING ALGEBRA

**Summary**

By applying the reduction matrices of Part I we analyzed in Part II the multiplication tables of generators of the cubic and nonion algebras, deduced the remaining  $3 \times 3$  sub-tables for the resulting algebra, determined the remaining 9 generators, and studied the corresponding multiplication tables. In this, Part III of the paper, we consider the problem of linear independence of the resulting generators. After checking the dimension 18 of the algebra (duodevencenion algebra), we extend the Peirce-Sylvester matrix quarter-plane to the whole plane. Choose in each quarter the generator related bridging scales, and analyse from that point of view the resulting duodevencenion algebra and other related “daughter algebras”: quasi-quaternion, quasi-para-quaternion, quasi-octonion and quasi-para-octonion.

*Keywords and phrases:* noncommutative Galois extensions, finite dimensional algebras, associative rings and algebras, matrix rings

**16. The dimension of the algebra in question**

The algebra in question, denoted by  $\mathcal{A}$ , considered in Parts I and II [5, 6] has formally 18 generators:

$$(21) \quad R_1 = \begin{pmatrix} 1 & 0 & 0 \\ 0 & 1 & 0 \\ 0 & 0 & 1 \end{pmatrix}, \quad Q_3 = \begin{pmatrix} 0 & 1 & 0 \\ 0 & 0 & 1 \\ 1 & 0 & 0 \end{pmatrix}, \quad \overline{Q}_3 = \begin{pmatrix} 0 & 0 & 1 \\ 1 & 0 & 0 \\ 0 & 1 & 0 \end{pmatrix},$$

$$(22) \quad R_3 = \begin{pmatrix} 1 & 0 & 0 \\ 0 & \mathbf{j}^2 & 0 \\ 0 & 0 & \mathbf{j} \end{pmatrix}, \quad Q_2 = \begin{pmatrix} 0 & \mathbf{j}^2 & 0 \\ 0 & 0 & \mathbf{j} \\ 1 & 0 & 0 \end{pmatrix}, \quad \overline{Q}_1 = \begin{pmatrix} 0 & 0 & 1 \\ \mathbf{j}^2 & 0 & 0 \\ 0 & \mathbf{j} & 0 \end{pmatrix},$$

$$(23) \quad R_2 = \begin{pmatrix} 1 & 0 & 0 \\ 0 & \mathbf{j} & 0 \\ 0 & 0 & \mathbf{j}^2 \end{pmatrix}, \quad Q_1 = \begin{pmatrix} 0 & \mathbf{j} & 0 \\ 0 & 0 & \mathbf{j}^2 \\ 1 & 0 & 0 \end{pmatrix}, \quad \overline{Q}_2 = \begin{pmatrix} 0 & 0 & 1 \\ \mathbf{j} & 0 & 0 \\ 0 & \mathbf{j}^2 & 0 \end{pmatrix},$$

$$(24) \quad R_4 = \begin{pmatrix} 0 & 0 & 1 \\ 0 & 1 & 0 \\ 1 & 0 & 0 \end{pmatrix}, \quad Q_6 = \begin{pmatrix} 0 & 1 & 0 \\ 1 & 0 & 0 \\ 0 & 0 & 1 \end{pmatrix}, \quad \overline{Q}_6 = \begin{pmatrix} 1 & 0 & 0 \\ 0 & 0 & 1 \\ 0 & 1 & 0 \end{pmatrix},$$

$$(25) \quad R_6 = \begin{pmatrix} 0 & 0 & 1 \\ 0 & \mathbf{j}^2 & 0 \\ \mathbf{j} & 0 & 0 \end{pmatrix}, \quad Q_5 = \begin{pmatrix} 0 & \mathbf{j}^2 & 0 \\ \mathbf{j} & 0 & 0 \\ 0 & 0 & 1 \end{pmatrix}, \quad \overline{Q}_4 = \begin{pmatrix} 1 & 0 & 0 \\ 0 & 0 & \mathbf{j}^2 \\ 0 & \mathbf{j} & 0 \end{pmatrix},$$

$$(26) \quad R_5 = \begin{pmatrix} 0 & 0 & 1 \\ 0 & \mathbf{j} & 0 \\ \mathbf{j}^2 & 0 & 0 \end{pmatrix}, \quad Q_4 = \begin{pmatrix} 0 & \mathbf{j} & 0 \\ \mathbf{j}^2 & 0 & 0 \\ 0 & 0 & 1 \end{pmatrix}, \quad \overline{Q}_5 = \begin{pmatrix} 1 & 0 & 0 \\ 0 & 0 & \mathbf{j} \\ 0 & \mathbf{j}^2 & 0 \end{pmatrix},$$

where  $\mathbf{j}^3 = 1$ ,  $\mathbf{j} \neq 1$ .

A natural question that arises is about linear independence of these generators. It is also important to find the *base* (or *bases*) of the algebra, i.e. the minimal subset of the set of generators (21)–(26) that linearly spans  $\mathcal{A}$ .

We have remarked already in [6] that  $\mathcal{A}$  might be generated by merely 15 generators because of  $12 \times 12$  complex matrices in (10)–(13) of [5] similarly to the case of nonion algebra and the related  $6 \times 6$  complex matrices in (8) and (9) of [5]:

$$12 + (6 - 9) = 15.$$

This is, however, not the case. Precisely, considering the Theorem in [6], Section 12, as Theorem 1, we formulate

**Theorem 2.** *We have*

$$\dim_{\mathbb{R}} \mathcal{A} = 18 \quad \text{and} \quad \mathcal{A} \cong M_3(\mathbb{C}).$$

Proof. Obviously,  $\dim_{\mathbb{C}} \mathcal{A} \leq 9$ . Let us note that

$$\dim_{\mathbb{R}} \mathcal{A} = \dim_{\mathbb{R}} \mathbb{C} \cdot \dim_{\mathbb{C}} \mathcal{A}.$$

We shall show that  $\dim_{\mathbb{C}} \mathcal{A} = 9$ , namely that matrices (21)–(26) span  $M_3(\mathbb{C})$ . It will be the case if, for every matrix  $X \in M_3(\mathbb{C})$ , there exist  $\alpha_1, \alpha_2, \dots, \alpha_{18} \in \mathbb{C}$  such that

$$(27) \quad X = \sum_{i=1}^{18} \alpha_i A_i,$$



where  $\{A_1, A_2, \dots, A_{18}\}$  is the set of matrices (21)–(26). The latter is equivalent to the existence of solution of the system of nine equations

$$(28) \quad \begin{cases} \alpha_1 a_{11}^1 + \alpha_2 a_{11}^2 + \dots + \alpha_{11}^{18} = x_{11} \\ \alpha_1 a_{12}^1 + \alpha_2 a_{12}^2 + \dots + \alpha_{12}^{18} = x_{12} \\ \vdots \\ \alpha_1 a_{33}^1 + \alpha_2 a_{33}^2 + \dots + \alpha_{33}^{18} = x_{33}, \end{cases}$$

where  $a_{ij}^k$  are entries of matrices  $A_k$ ,  $i, j = 1, 2, 3$ ,  $k = 1, 2, \dots, 18$ . This, however, is equivalent to

$$(29) \quad \text{rank} \begin{bmatrix} a_{11}^1 & a_{11}^2 & \cdots & a_{11}^{18} \\ a_{12}^1 & a_{12}^2 & \cdots & a_{12}^{18} \\ \vdots & & \cdots & \vdots \\ a_{33}^1 & a_{33}^2 & \cdots & a_{33}^{18} \end{bmatrix} = 9.$$

We can naturally divide the generators of the algebra into six groups

$$(30) \quad \begin{aligned} L_1 &= Ls\{R_1, Q_3, \overline{Q}_3\}, & L_2 &= Ls\{R_3, Q_2, \overline{Q}_1\}, & L_3 &= Ls\{R_2, Q_1, \overline{Q}_2\}, \\ L_4 &= Ls\{R_4, Q_6, \overline{Q}_6\}, & L_5 &= Ls\{R_6, Q_5, \overline{Q}_4\}, & L_6 &= Ls\{R_5, Q_4, \overline{Q}_5\}, \end{aligned}$$

and mark them with different colours as can be seen in Fig. 3. Obviously, 18 matrices (21)–(26) are too many for the base of  $\mathcal{A}$ , so we shall choose a smaller set, based on Fig. 3, namely

$$(31) \quad \{A_1, A_2, \dots, A_9\} = \{R_1, Q_3, \overline{Q}_3, R_3, Q_2, \overline{Q}_1, R_2, Q_1, \overline{Q}_2\}$$

and, by straightforward calculation, thanks to [20], we verify that

$$(32) \quad \text{rank} \begin{bmatrix} a_{11}^1 & a_{11}^2 & \cdots & a_{11}^9 \\ a_{12}^1 & a_{12}^2 & \cdots & a_{12}^9 \\ \vdots & & \cdots & \vdots \\ a_{33}^1 & a_{33}^2 & \cdots & a_{33}^9 \end{bmatrix} = 9.$$

We have thus also obtained that the set (31) forms a base of the algebra  $\mathcal{A}$ .

## 17. Choice of the six generators forming the basic bridging scales

Following Peirce [11] and Sylvester [13] it is natural to consider a matrix first quarter-plane  $uR_1v$  with origin at  $R_1 = I_3$  and positive half-axes  $u$  and  $v$  containing points

$$u = \overline{Q}_2, \quad u^2 = Q_2, \quad \text{and} \quad v = \overline{Q}_1, \quad v^2 = Q_1,$$

respectively. Clearly, considering negative half-axes  $u$  and  $v$  has no sense. However, observe that  $u^3 = v^3 = I_3$ .

More generally, let  $\mathcal{A}$  be the considered  $3 \times 3$  matrix algebra over  $\mathbb{C}$ . Let  $A \in \mathcal{A}$ . Let  $\text{rang}$  of  $A$  (and we shall write  $r(A)$ ) denote the smallest positive integer  $n$  such that  $A^n = \alpha R_1 = \alpha I_3$ ,  $\alpha \in \{1, \mathbf{j}, \mathbf{j}^2\}$ . We have

$$r(A) = \begin{cases} 1 & \text{for } A = R_1, \\ 2 & \text{for } A \in \{R_4, Q_6, \overline{Q}_6, R_6, Q_5, \overline{Q}_4, R_5, Q_4, \overline{Q}_5\}, \\ 3 & \text{for } A \in \{Q_3, \overline{Q}_3, R_3, Q_2, \overline{Q}_1, R_2, Q_1, \overline{Q}_2\}. \end{cases}$$

We also have

$$r(A \cdot B) = \begin{cases} 3 & \text{if } r(A) = r(B) \neq 1, \\ 2 & \text{if } r(A) \neq r(B), \text{ and } r(A), r(B) \neq 1. \end{cases}$$

Consider the operator  $\perp$  defined in the following way

$$(33) \quad A^\perp = \begin{pmatrix} a & b & c \\ d & e & f \\ g & h & i \end{pmatrix}^\perp = \begin{pmatrix} c & f & i \\ b & e & h \\ a & d & g \end{pmatrix}.$$

We can easily check that (and it is clearly visible in the colorful table)

$$r(A^\perp) = \begin{cases} 2 & \text{if } r(A) = 1 \text{ or } r(A) = 3, \\ 3 & \text{if } r(A) = 2. \end{cases}$$

If we construct the diagram with the use of  $\perp$  operator then the axes scaling matrices of rang 3 are transformed into matrices of rang 2 and vice-versa.

Therefore, taking into account that, by (33)

$$(34) \quad a_{\alpha,\beta} \xrightarrow{\perp} a_{\beta,4-\alpha} \xrightarrow{\perp} a_{4-\alpha,4-\beta} \xrightarrow{\perp} a_{4-\beta,\alpha} \xrightarrow{\perp} a_{\alpha\beta}, \quad \alpha, \beta = 1, 2, 3,$$

we have

$$\begin{aligned} R_1 &\xrightarrow{\perp} R_4 \xrightarrow{\perp} R_1 \xrightarrow{\perp} R_4 \xrightarrow{\perp} R_1, \\ \overline{Q}_2 &\xrightarrow{\perp} \overline{Q}_4 \xrightarrow{\perp} Q_2 \xrightarrow{\perp} Q_4 \xrightarrow{\perp} \overline{Q}_2, \quad \overline{Q}_1 \xrightarrow{\perp} \overline{Q}_5 \xrightarrow{\perp} Q_1 \xrightarrow{\perp} Q_5 \xrightarrow{\perp} \overline{Q}_1, \\ Q_2 &\xrightarrow{\perp} Q_1 \xrightarrow{\perp} \overline{Q}_2 \xrightarrow{\perp} \overline{Q}_4 \xrightarrow{\perp} Q_2, \quad Q_1 \xrightarrow{\perp} Q_5 \xrightarrow{\perp} \overline{Q}_1 \xrightarrow{\perp} \overline{Q}_5 \xrightarrow{\perp} Q_1. \end{aligned}$$

This means we are naturally led to the six generators

$$(35) \quad R_1, \overline{Q}_2, Q_2, \overline{Q}_1, Q_1, R_4$$

forming the bridging scales on four matrix quarter-planes

$$uR_1v, u_\perp R_4v_\perp, u_{\perp\perp} R_1v_{\perp\perp}, u_{\perp\perp\perp} R_4v_{\perp\perp\perp},$$

where  $u$  and  $v$  stand for the positive  $u$  and  $v$  half-axes, respectively. The motivation for choosing (35) is visualized on the multiplication table expressed as on Fig. 4.

*	$R_1$	$Q_3$	$\overline{Q_3}$	$R_3$	$Q_2$	$\overline{Q_1}$	$R_2$	$Q_1$	$\overline{Q_2}$	$R_4$	$Q_5$	$\overline{Q_6}$	$R_6$	$Q_5$	$\overline{Q_4}$	$R_5$	$Q_4$	$\overline{Q_5}$
$R_1$	$R_1$	$Q_3$	$\overline{Q_3}$	$R_3$	$Q_2$	$\overline{Q_1}$	$R_2$	$Q_1$	$\overline{Q_2}$	$R_4$	$Q_6$	$\overline{Q_6}$	$R_6$	$Q_5$	$\overline{Q_4}$	$R_5$	$Q_4$	$\overline{Q_5}$
$Q_3$	$Q_3$	$\overline{Q_3}$	$R_1$	$Q_2$	$\overline{Q_1}$	$j^2 R_3$	$Q_1$	$j^2 \overline{Q_2}$	$j R_2$	$Q_6$	$\overline{Q_6}$	$R_4$	$Q_5$	$j^2 \overline{Q_4}$	$j^2 R_6$	$Q_4$	$j^2 \overline{Q_5}$	$j R_5$
$\overline{Q_3}$	$\overline{Q_3}$	$R_1$	$Q_3$	$j \overline{Q_1}$	$R_3$	$j^2 Q_2$	$j^2 \overline{Q_2}$	$R_2$	$j Q_1$	$\overline{Q_6}$	$R_4$	$Q_6$	$j \overline{Q_4}$	$R_6$	$j^2 Q_5$	$j^2 \overline{Q_5}$	$R_5$	$j Q_4$
$R_3$	$R_3$	$j Q_2$	$\overline{Q_1}$	$R_2$	$j Q_1$	$\overline{Q_2}$	$R_1$	$j Q_3$	$\overline{Q_3}$	$R_6$	$j Q_5$	$\overline{Q_4}$	$R_5$	$j Q_4$	$\overline{Q_5}$	$R_4$	$j Q_6$	$\overline{Q_6}$
$Q_2$	$Q_2$	$j^2 \overline{Q_1}$	$j^2 R_3$	$Q_1$	$\overline{Q_2}$	$j R_2$	$Q_3$	$j \overline{Q_3}$	$R_1$	$Q_5$	$j^2 \overline{Q_4}$	$j^2 R_6$	$Q_4$	$\overline{Q_5}$	$j R_5$	$Q_6$	$j \overline{Q_6}$	$R_4$
$\overline{Q_1}$	$\overline{Q_1}$	$R_3$	$j Q_2$	$j \overline{Q_2}$	$R_2$	$Q_1$	$j^2 \overline{Q_3}$	$R_1$	$j^2 Q_3$	$\overline{Q_4}$	$R_6$	$j Q_5$	$j \overline{Q_5}$	$R_5$	$Q_4$	$j^2 \overline{Q_6}$	$R_4$	$j^2 Q_6$
$R_2$	$R_2$	$j^2 Q_1$	$\overline{Q_2}$	$R_1$	$j^2 Q_3$	$\overline{Q_3}$	$R_3$	$j^2 Q_2$	$\overline{Q_1}$	$R_5$	$j^2 Q_4$	$\overline{Q_5}$	$R_4$	$j^2 Q_6$	$\overline{Q_6}$	$R_6$	$j^2 Q_5$	$\overline{Q_4}$
$Q_1$	$Q_1$	$j \overline{Q_2}$	$j R_2$	$Q_3$	$j^2 \overline{Q_3}$	$R_1$	$Q_2$	$\overline{Q_1}$	$j^2 R_3$	$Q_4$	$j \overline{Q_5}$	$j R_5$	$Q_6$	$j^2 \overline{Q_6}$	$R_4$	$Q_5$	$\overline{Q_4}$	$j^2 R_6$
$\overline{Q_2}$	$\overline{Q_2}$	$R_2$	$j^2 Q_1$	$j \overline{Q_3}$	$R_1$	$j Q_3$	$j^2 \overline{Q_1}$	$R_3$	$Q_2$	$\overline{Q_5}$	$R_5$	$j^2 Q_4$	$j \overline{Q_6}$	$R_4$	$j Q_6$	$j^2 \overline{Q_4}$	$R_6$	$Q_5$
$R_4$	$R_4$	$\overline{Q_6}$	$Q_6$	$j R_5$	$\overline{Q_5}$	$Q_4$	$j^2 R_6$	$\overline{Q_4}$	$Q_5$	$R_1$	$\overline{Q_3}$	$Q_3$	$j R_2$	$\overline{Q_2}$	$Q_1$	$j^2 R_3$	$\overline{Q_1}$	$Q_2$
$Q_6$	$Q_6$	$R_4$	$\overline{Q_6}$	$j Q_4$	$j R_5$	$j^2 \overline{Q_3}$	$j^2 Q_5$	$j^2 R_6$	$j \overline{Q_4}$	$Q_3$	$\overline{Q_3}$	$\overline{Q_1}$	$j Q_1$	$j R_2$	$j^2 \overline{Q_2}$	$j^2 Q_2$	$j^2 R_3$	$j \overline{Q_1}$
$\overline{Q_6}$	$\overline{Q_6}$	$Q_6$	$R_4$	$\overline{Q_5}$	$j Q_4$	$R_5$	$\overline{Q_4}$	$j^2 Q_5$	$R_6$	$\overline{Q_3}$	$Q_3$	$\overline{Q_3}$	$\overline{Q_2}$	$j Q_1$	$R_2$	$\overline{Q_1}$	$j^2 Q_2$	$R_3$
$R_6$	$R_6$	$j \overline{Q_4}$	$j Q_5$	$j R_4$	$\overline{Q_6}$	$j Q_6$	$j^2 R_5$	$\overline{Q_5}$	$j Q_4$	$R_3$	$\overline{Q_1}$	$j Q_2$	$j R_1$	$\overline{Q_3}$	$j Q_3$	$j^2 R_2$	$\overline{Q_2}$	$j Q_1$
$Q_5$	$Q_5$	$j^2 R_6$	$j^2 \overline{Q_4}$	$j Q_6$	$R_4$	$j \overline{Q_6}$	$j^2 Q_4$	$j R_5$	$\overline{Q_5}$	$Q_2$	$j^2 R_3$	$j^2 \overline{Q_1}$	$j Q_3$	$R_1$	$j \overline{Q_3}$	$j^2 Q_1$	$j R_2$	$\overline{Q_2}$
$\overline{Q_4}$	$\overline{Q_4}$	$j Q_5$	$R_6$	$\overline{Q_6}$	$j^2 Q_6$	$R_4$	$\overline{Q_5}$	$R_5$	$Q_4$	$\overline{Q_1}$	$j Q_2$	$R_3$	$\overline{Q_3}$	$j^2 Q_3$	$R_1$	$\overline{Q_2}$	$Q_1$	$R_2$
$R_5$	$R_5$	$\overline{Q_5}$	$j^2 Q_4$	$j R_6$	$\overline{Q_4}$	$j^2 Q_5$	$j^2 R_4$	$\overline{Q_6}$	$j^2 Q_6$	$R_2$	$\overline{Q_2}$	$j^2 Q_1$	$j R_3$	$\overline{Q_1}$	$j^2 Q_2$	$j^2 R_1$	$\overline{Q_3}$	$j^2 Q_3$
$Q_4$	$Q_4$	$j R_5$	$j \overline{Q_5}$	$j Q_5$	$j^2 R_6$	$\overline{Q_4}$	$j^2 Q_6$	$R_4$	$j^2 \overline{Q_6}$	$Q_1$	$j R_2$	$j \overline{Q_2}$	$j Q_2$	$j^2 R_3$	$\overline{Q_1}$	$j^2 Q_3$	$R_1$	$j^2 \overline{Q_3}$
$\overline{Q_5}$	$\overline{Q_5}$	$j^2 Q_4$	$R_5$	$\overline{Q_4}$	$Q_5$	$j^2 Q_4$	$\overline{Q_6}$	$\overline{Q_2}$	$j^2 Q_1$	$\overline{Q_2}$	$j^2 Q_1$	$j^2 Q_1$	$j Q_1$	$\overline{Q_1}$	$Q_2$	$\overline{Q_3}$	$j Q_3$	$R_1$

Fig. 4: Motivation for the choice of the six generators  $R_1$ ,  $\overline{Q_2}$ ,  $\overline{Q_1}$  and  $R_4$ ,  $\overline{Q_4}$ ,  $\overline{Q_5}$  forming the basic bridging scales.



## 18. The Riemann surface approach. The “daughter algebras”: quasi-quaternion and quasi-para-quaternion

Studying closer the matrix quarter-plane concerned we can see how to construct their inner points [6, 8, 11]:

$$(36) \quad \begin{aligned} (u, v) &= uv = \frac{1}{j}vu = jQ_2, & (u^2, v^2) &= u^2v^2 = j^2v^2u^2 = j\bar{Q}_3, \\ (u^2, v) &= u^2v = jvu^2 = jR_2, & (u, v^2) &= uv^2 = jv^2u = R_3. \end{aligned}$$

Then we have

$$(37) \quad \begin{aligned} jQ_3 &\mapsto jQ_6 \mapsto j\bar{Q}_3 \mapsto j\bar{Q}_6 \mapsto jQ_3, & \bar{Q}_3 &\mapsto j\bar{Q}_6 \mapsto Q_3 \mapsto jQ_6 \mapsto j\bar{Q}_3, \\ jR_2 &\mapsto R_6 \mapsto R_3 \mapsto j\bar{R}_5 \mapsto jR_2, & R_3 &\mapsto j\bar{R}_5 \mapsto jR_2 \mapsto R_6 \mapsto R_3. \end{aligned}$$

The resulting collection of four matrix quarter-planes is visualized in Fig. 4.

Following [3] we may construct from the quarter-planes concerned a Riemann surface gluing

$$(38) \quad v \text{ to } u_{\perp}, \quad v_{\perp} \text{ to } u_{\perp\perp}, \quad v_{\perp\perp} \text{ to } u_{\perp\perp\perp}, \quad v_{\perp\perp\perp} \text{ to } u,$$

with piercing *two copies* of the plane along the cut  $v_{\perp\perp\perp}$  in the case of the 4-sheeted Riemann surface model, or, alternatively, with gluing (38) as before, but with piercing *no copy* of the plane along the cut  $v_{\perp\perp\perp}$ ,  $u$ , in the case of two-sheeted Riemann surface model.

By relations (36) and (37) we have the following Corollary to Theorem 2.

**Corollary 1.** The **para-nonion algebra** spanned by the generators (21)–(23), discussed in the third matrix quarter-plane in question, coincides with the nonion algebra. However, different order of the generators allows for a new geometrical interpretation, analogous to that for para-quaternions in relation to quaternions. In contrast, the **quasi-para-quaternion algebra** spanned by

$$(39) \quad R_1 = I_3, \quad u_{\perp\perp} = Q_2, \quad v_{\perp\perp} = Q_1, \quad uv_{\perp\perp} = jQ_3$$

is different from the **quasi-quaternion algebra** spanned by

$$(40) \quad R_1 = I_3, \quad u = Q_2, \quad v = \bar{Q}_1, \quad uv = jQ_3.$$

However, the para-quaternion algebra contains, as its subalgebra, the quasi-quaternion algebra thanks to the transformation

$$(41) \quad (I_3)_{\perp\perp}^2 \mapsto I_3, \quad u_{\perp\perp}^2 \mapsto u, \quad v_{\perp\perp}^2 \mapsto v, \quad (u^2v^2)_{\perp\perp} \mapsto uv.$$

For para-quaternions we refer to [17] and references therein. In study of quasi-quaternions and quasi-para-quaternions in [3]. Further studies of a Riemann surface approach to para-quaternions, referring to Vaccaro Obitz [19] will be continued in [8].

## 19. Further “daughter algebras”: quasi-octonion, quasi-para-octonion, and para-duodevicenion

We proceed to study still closer the second and fourth matrix quarter-planes concerned; see Fig. 6. In analogy to Corollary 1 we distinguish the following objects: the quasi octonion algebra, spanned by the generators

$$(42) \quad \begin{aligned} R_1, R_4, u = \overline{Q}_2, u_\perp = \overline{Q}_4, \\ v = \overline{Q}_1, v_\perp = \overline{Q}_5, uv = \mathbf{j}Q_3, (uv)_\perp = \mathbf{j}Q_6; \end{aligned}$$

the *quasi-para-octonion algebra*, spanned by the generators

$$(43) \quad \begin{aligned} R_1, R_4, u_{\perp\perp} = Q_2, u_{\perp\perp\perp} = Q_4, v_{\perp\perp} = Q_1, v_{\perp\perp\perp} = Q_5, \\ (uv)_{\perp\perp} = \mathbf{j}\overline{Q}_3, (uv)_{\perp\perp\perp} = \mathbf{j}\overline{Q}_6; \end{aligned}$$

the *para-duodevicenion algebra*, spanned by

$$(44) \quad (L_\alpha)_{\perp\perp}, \alpha = 1, \dots, 6, \text{ with } L_\alpha \text{ given by (30).}$$

We conclude with the following

**Corollary 2.** The para-duodevicenion algebra spanned by generators (21)–(26) or equivalently, by (45) discovered in the 3rd and 4th matrix-quarter-planes in questions, coincides with the duodeviceinon algebra. However, different order of the generators allows a new geometrical interpretation, analogous to that for para-quaternions with quaternions. In contrast, the quasi-para-octonion algebra, spanned by (43), is different from the quasi-para-octonion algebra spanned by (42). Moreover, the para-duodevicenion algebra contains, as subalgebra the quasi-octonion algebra thanks to the transformation consisting of (41) and

$$(45) \quad (I_3)_{\perp\perp\perp}^2 \mapsto (I_3)_\perp, u_{\perp\perp\perp}^2 \mapsto u_\perp, v_{\perp\perp\perp}^2 \mapsto v_\perp, (uv)_{\perp\perp\perp}^2 \mapsto uv_\perp.$$

For nonions we also refer to [14–19], for Clifford-algebraic background – to [12, 1, 2]. Further study of a Riemann surface approach to nonions and duodevicenions, including the corresponding  $\partial$ ,  $\overline{\partial}$ -type operators and Galois extensions (cf. [2]) will be continued in [7, 9, 10].

## 20. Conclusions

Further study mentioned at the end of Sections 18 and 19 has to be connected with the identifications discussed in the first part of this paper [5] and the relationship between Observations 1–6 in the second part of this paper [6] and the structures observed in Figs. 3–6 of the present, third part of the paper in relation with the group (30) of generators.

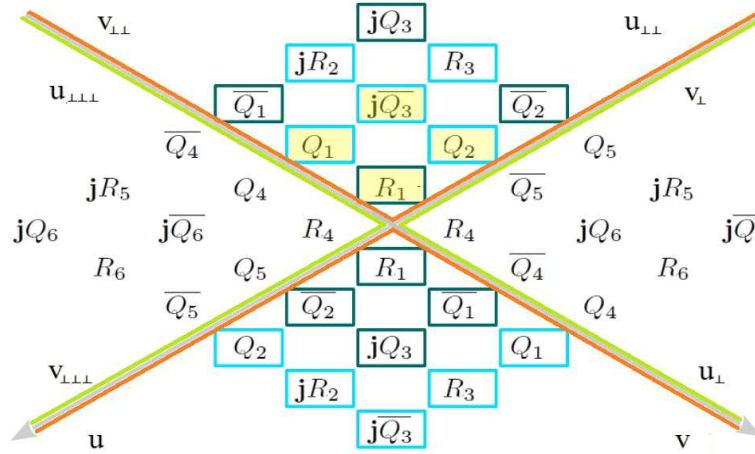


Fig. 5: Four matrix quarter-planes with the chosen generator related bridging scales. The quasi-quaternion (blue) algebra with the generators (40) and the quasi-para-quaternion (yellow) algebra with generators (39).

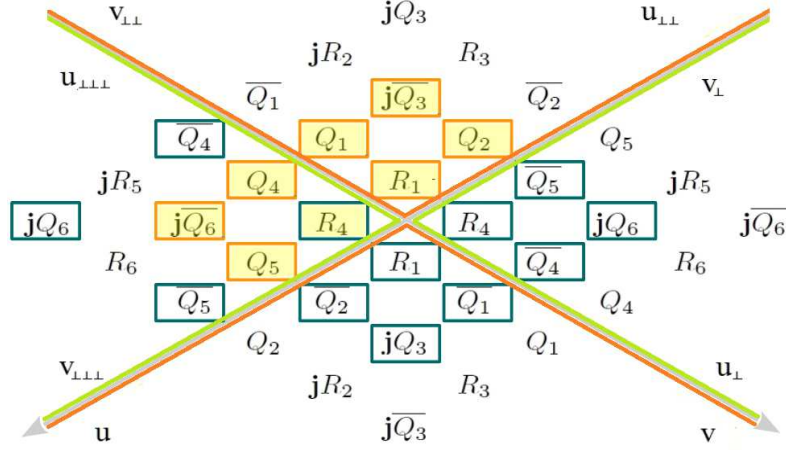


Fig. 6: The quasi-octonion (blue) algebra with the generators (42) and the quasi-para-octonion (yellow) algebra with generators (43).

A deeper understanding is needed for comparing the process of construction  
cubic algebra  $\longrightarrow$  nonion algebra  $\longrightarrow$  duodevicienion algebra  
**with** the Cayley-Dickson doubling process  
complex algebra  $\longrightarrow$  quaternion algebra  $\longrightarrow$  duodevicienion algebra  
as well as the process of construction  
ternary approach vs. binary approach  $\longrightarrow$  quaternary approach vs. ternary  
approach  
(in connection with fractal and chaos related to Ising-Onsager-Zhang lattices  
[1, 2, 4]) **with** optimization procedures for the total energy in physics of complex  
alloys [3].

## References

- [1] F. L. Castillo Alvarado, J. Lawrynowicz, and M. Nowak-Kępczyk, *Fractal modelling of alloy thin films. Temperatures characteristic for local phase transitions*, in: Applied Complex and Quaternionic Approximation, ed. R. K. Kovacheva, J. Lawrynowicz, and S. Marchiafava, Ediz. Nuova Cultura, Univ. 'La Sapienza', Roma 2009, pp. 207–236.
- [2] J. Lawrynowicz, K. Nôno, and O. Suzuki, *Binary and ternary Clifford analysis vs noncommutative Galois extensions II. The correspondence between the binary and ternary field operators*, Bull. Soc. Sci. Lettres Łódź Sér. Rech. Déform. **62**, no. 3 (2012), 109–118.
- [3] J. Lawrynowicz, M. Nowak-Kępczyk, A. Valianti, and M. Zubert, *Physics of complex alloys – one-dimensional relaxation problem and the role of total energy calculation*, *ibid.* **65**, no. 2 (2015), 25–46.
- [4] J. Lawrynowicz, O. Suzuki, A. Niemczynowicz, and M. Nowak-Kępczyk, *Fractals and chaos related to Ising-Onsager-Zhang lattices. Quaternary approach vs. ternary approach*, Ms. (2015) ca. 16 pp., to appear.
- [5] M. Nowak-Kępczyk, *An algebra governing reduction of quaternary structures to ternary structures I, Reductions of quaternary structures to ternary structures*, Bull. Soc. Sci. Lettres Łódź Sér. Rech. Déform. **64**, no. 2 (2014), 101–109.
- [6] M. Nowak-Kępczyk, *An algebra governing reduction of quaternary structures to ternary structures II. A study of the multiplication table for the resulting algebra generators*, Bull. Soc. Sci. Lettres Łódź, Sér. Rech. Déform. **64**, no. 3 (2014), 81–90.
- [7] M. Nowak-Kępczyk, *Riemann surface approach to duodevicienions*, *ibid.* **66**, no. 3 (2016), ca. 10pp., to appear.
- [8] M. Nowak-Kępczyk, *Riemann surface approach to para-quaternions*, Ms. (2016), ca. 16pp., in preparation.
- [9] M. Nowak-Kępczyk, *From nonions to duodevicienions*, Ms. (2015), ca. 10pp., in preparation.
- [10] M. Nowak-Kępczyk, *Duodevicienions equipped with  $\partial$ ,  $\delta$ -type operators and the corresponding Galois extensions*, Ms. (2016), ca. 12pp., in preparation.
- [11] C. S. Peirce, *On Nonions*, in: Collected Papers of Charles Sanders Peirce, 3rd ed., vol. III, Harvard University Press, Cambridge Mass. 1967, pp. 411–416.
- [12] I. R. Porteous, *Clifford Algebras and the Classical Groups*, Cambridge Studies in Advanced Mathematics **50**, Cambridge Univ. Press, 1995.

- [13] J. J. Sylvester, *A word on nonions*, John Hopkins Univ. Circulars **1** (1882), 241–242 (1883), 46; in: The Collected Mathematical Papers of James Joseph Sylvester, vol. III, Cambridge Univ. Press, Cambridge 1909, pp. 647–650.
- [14] J. J. Sylvester, *On the involution of two matrices of the second order*, Brit. Assoc. Report 1883, 430–432; in: The Collected Mathematical Papers of James Joseph Sylvester, vol. IV, Cambridge Univ. Press, Cambridge 1912, pp. 115–117.
- [15] J. J. Sylvester, *Sur les quantités formant un groupe de nonions analogues aux quaternions de Hamilton*, C. R. Acad. Sci. Paris **97** (1883), 1336–1340; **98** (1884), 273–276, 471–473; in: The Collected Mathematical Papers of James Joseph Sylvester, vol. IV, Cambridge Univ. Press, Cambridge 1912, pp. 154–159.
- [16] J. J. Sylvester, *On quaternions, nonions, sedenions etc.*, Johns Hopkins Univ. Circulars **3** (1984), 7–9; in: The Collected Mathematical Papers of James Joseph Sylvester, vol. IV, Cambridge Univ. Press, Cambridge 1909, pp. 122–132.
- [17] M. Vaccaro, *Subspaces of a paraquaternionic Hermitian vector space*, Internat. J. of Geom. Methods in Modern Phys. **8**, no. 7 (2011), 1487–1506.
- [18] M. Vaccaro, *Orbits of the real Grassmanian of 2 planes under the action of the groups  $Sp(n)$  and  $Sp(n) \cdot Sp(1)$* , Bull. Soc. Sci. Lettres Łódź, Sér. Rech. Déform. **65**, no. 3 (2015), 121–140, to appear.
- [19] J. H. M. Wedderburn, *On hypercomplex numbers*, Proc. London Math. Soc. **26** (1908), 77118.
- [20] Calculating software on: [www.matrix.reshish.com](http://www.matrix.reshish.com), ©reshish.com 2011–2015.

Institute of Mathematics and Informatics  
 The State School of Higher Education in Chełm  
 54 Pocztowa Street, PL-22-100 Chełm  
 Poland  
 e-mail: gosianmk@wp.pl

Presented by Julian Ławrynowicz at the Session of the Mathematical-Physical Commission of the Łódź Society of Sciences and Arts on November 20, 2014

## O ALGEBRZE, W KTÓREJ STRUKTURY TYPU KWATERNARNEGO SĄ REDUKOWANE DO STRUKTUR TYPU TERNARNEGO III

### ANALIZA TABELI MNOŻENIA GENERATORÓW ODPOWIEDNIEJ ALGEBRY

#### Streszczenie

Analizowana jest tabela mnożenia generatorów algebry rozważanej w Części I tego artykułu. Stosując macierze redukujące z Części I analizowane są tabele mnożenia generatorów algebr kubicznej i nonionowej i stąd wywodzone pozostałe 9 generatorów, a następnie analizowane ich tabele mnożenia. Zagadnienie liniowej niezależności tak otrzymanych generatorów zostanie poruszone w Części III.

*Słowa kluczowe:* nieprzemienne rozszerzenia Galois, algebry skończonego wymiaru, łączne algebry i pierścienie, pierścienie macierzy



## B U L L E T I N

DE LA SOCIÉTÉ DES SCIENCES ET DES LETTRES DE ŁÓDŹ

2016

Vol. LXVI

Recherches sur les déformations

no. 1

pp. 135–148

*Contribution to the jubilee volume, dedicated  
to Professors J. Ławrynowicz and L. Wojtczak*

*Aleksandra Baszczyńska*

## NONCLASSICAL PARAMETERS IN KERNEL ESTIMATION

**Summary**

In kernel method, using in estimation as well as in hypothesis testing problems, two parameters should be fixed: kernel function and smoothing parameter. Some methods of kernel estimation and methods of choosing kernel parameters (classical and nonclassical) are presented. Basing on simulation study results, chosen kernel estimation methods are compared, taking into account their properties.

*Keywords and phrases:* kernel method, kernel function, smoothing parameter, estimation

**1. Introduction**

Nonparametric methods are becoming more and more popular in statistical analyses of not only economic but also technical, medical, biometric and environmental problems. The term “nonparametric” is used in a very general sense that broadly widens the area of nonparametric methods applications on one hand and allows the users to treat nonparametric methods as fundamental ones on the other. Applying nonparametric methods in statistical analysis means that the assumption that data being analyzed do not belong to any particular distribution is not absolutely necessary or that the researchers do not assume that the structure of a statistical model is fixed.

Using statistical procedures without necessity of assuming the parameterized family of probability distribution of regarded random variable seems to be very convincing. In many economic problems, a lack of information about analyzed random variable is noticeable. We cannot rely on the assumption that the data are drawn

from a given distribution (in mostly cases it is normal distribution). These are situations where nonparametric methods are the only ones that can be used in practice. Parametric approach, in which the researchers are obligated to know the form of distribution is treated as risky one. In many cases we do not have any information about economic phenomenon, for example we are not able to collect proper historical data that can be used to verify assumptions. In nonparametric approach there is no need to take the assumptions that may not be true. From theoretical considerations follows that nonparametric procedures are only slightly less effective than the procedures based on normal distributions [1].

In statistical literature various nonparametric methods are described and their properties are presented [2–4].

Kernel methods, belonging to a class of nonparametric procedures, are well-known and broadly used statistical procedures by nonparametricians. It is caused by two aspects of these methods, that are particular emphasized in statistical literature: their simplicity and ease of implementation. Kernel estimation may concern, for example, density function, distribution function, regression function or hazard function. There are also kernel methods of estimating numerical characteristics of random variable, for example mode or quantiles. Among the statistical tests based on kernel methods there are goodness-of-fit tests, symmetry tests or independence tests. Some of these procedures are presented in, e.g. [5–7] with studies of these inference methods properties.

## 2. Kernel method in estimation

Kernel estimator of density  $f(x)$  of random variable  $X$ , calculated using the random sample  $X_1, \dots, X_n$ , where  $n$  is a sample size, was introduced by Parzen [8] and Rosenblatt [9]. It is defined in the following way (cf.: [10], [11]):

$$(1) \quad \hat{f}(x) = \frac{1}{nh} \sum_{i=1}^n K\left(\frac{x - X_i}{h}\right),$$

where  $h$  is a smoothing parameter (bandwidth) depending on the sample size  $n$  ( $h = h(n)$ );  $K(u)$  is a kernel function with the following properties:

$$\begin{aligned} \int_{-\infty}^{+\infty} K(u) du &= 1, \\ \int_{-\infty}^{+\infty} u^l K(u) du &= \mu_l(K) = 0 \quad \text{for } l = 1, \dots, k-1, \\ \int_{-\infty}^{+\infty} u^k K(u) du &= \mu_k(K) \neq 0; \end{aligned}$$

$k$  is called the order of the kernel function.



Formula (1) indicates that kernel density estimator is a way of counting the number of observations that are falling into the interval around  $x$ . Bandwidth  $h$  controls the smoothness of the estimator (for bigger values of  $h$ , the estimator is smoother) while kernel function is a weighted function centered at one of the observations from the sample  $X_1, \dots, X_n$ .

The bias of the estimator (1) is proportional to  $h^2$ . Small values of smoothing parameter guarantee reduction of the bias. While the variance of the estimator is proportional to  $\frac{1}{nh}$ . To make the variance of the estimator small, the smoothing parameter should be large. For  $h \rightarrow 0$  and  $nh \rightarrow \infty$  Mean Square Error (MSE) goes to infinity. It means that kernel density estimator  $\hat{f}(x)$  is consistent estimator of unknown density function  $f(x)$ .

The idea of Parzen-Rosenblatt kernel density estimator (1) is using in many inference procedure for functional or numerical characteristics of random variable.

Nadaraya kernel distribution function estimator is obtained by integrating kernel density estimator (1). For random variables  $X_1, \dots, X_n$  with density  $f(x)$  and distribution function  $F(x)$  it is defined as:

$$(2) \quad \hat{F}(x) = \frac{1}{n} \sum_{i=1}^n W\left(\frac{x - X_i}{h}\right),$$

where

$$W(x) = \int_{-\infty}^{+\infty} K(t) dt,$$

$K(t) \geq 0$  is kernel function of second order.

Kernel distribution function  $\hat{F}(x)$  is asymptotically unbiased and its variance is the same as for well-known empirical distribution function.

As it is for kernel density estimator, the choice of smoothing parameter in kernel estimation of distribution function is more important than kernel function choice.

Estimators of distribution function and other functional and numerical probabilistic characteristics of random variable, including estimators of quantiles and estimators of conditional characteristics, are presented in [12].

In the reliability assessment, for kernel estimates of distribution functions  $\hat{F}_1(x)$  and  $\hat{F}_2(x)$  of samples  $X_{11}, \dots, X_{1n_1}$  and  $X_{21}, \dots, X_{2n_2}$ , respectively, the kernel estimator of *ROC (Receiver Operating Characteristic)* function can be defined as:

$$(3) \quad \hat{R}(p) = 1 - \hat{F}_2\left(\hat{F}_1^{-1}(1 - p)\right) \quad \text{for } 0 \leq p \leq 1,$$

where

$$\hat{F}_j(x) = \frac{1}{n_j} \sum_{i=1}^{n_j} W\left(\frac{x - X_{ji}}{h_j}\right), \quad j = 1, 2.$$

For constructing the kernel estimator of *ROC* it is necessary to use kernel function  $K(u)$  and two smoothing parameters  $h_1$  and  $h_2$ . The quartic kernel function is recommended in this case:

$$K(u) = \begin{cases} \frac{15}{16}(1-u^2)^2 & \text{for } |u| \leq 1, \\ 0 & \text{otherwise.} \end{cases}$$

The kernel estimator of the  $\nu$ -th derivative of the hazard function

$$\lambda(x) = \frac{f(x)}{1-F(x)}$$

is the convolution of the kernel  $K(u)$  and the Nelson estimator of the cumulative hazard function

$$H_n(x) = \sum_{X_{(i)} \leq x} \frac{\delta_{(i)}}{n-i+1},$$

where  $\delta_i$  is indicator whether the observation is censored or not. In the random censorship model  $(X_i, \delta_i)$  for  $i = 1, \dots, n$ ,  $X_i = \min(T_i, C_i)$ , where  $T_1, \dots, T_n$  are survival times with the distribution function  $F$  and  $C_1, \dots, C_n$  are censoring times with the distribution  $G$  (independent from survival times). The kernel estimator of the  $\nu$ -th derivative of the hazard function is following:

$$\begin{aligned} \tilde{\lambda}^{(\nu)}(x) &= \frac{1}{h^{\nu+1}} \int_{-\infty}^{+\infty} K^{(\nu)}\left(\frac{x-u}{h}\right) dH_n(u) \\ (4) \quad &= \frac{1}{h^{\nu+1}} \sum_{i=1}^n K^{(\nu)}\left(\frac{x-X_{(i)}}{h}\right) \frac{\delta_{(i)}}{n-i+1}, \end{aligned}$$

where  $K^{(\nu)}$  is  $\nu$ -th order kernel function.

Nadaraya-Watson kernel estimator of regression function  $m$ , in a standard regression model  $Y_i = m(X_i) + \varepsilon_i$ ,  $i = 1, \dots, n$ , where  $\{(X_i, Y_i)\}$  are  $n$  independent observations,  $m$  is unknown regression function,  $E(\varepsilon_i) = 0$  and  $D^2(\varepsilon_i) = \sigma^2 > 0$ , is defined as:

$$(5) \quad \hat{m}(x) = \frac{\sum_{i=1}^n K_h(x_i - x) Y_i}{\sum_{i=1}^n K_h(x_i - x)},$$

where

$$K_h(u) = \frac{1}{h} K\left(\frac{u}{h}\right).$$

In Nadaraya-Watson estimator observations  $Y_i$  obtain more weight in those areas where the corresponding  $X_i$  are sparse. Estimator (5) is consistent estimate of the regression curve for  $h \rightarrow 0$  and  $nh \rightarrow \infty$ .

### 3. Kernel function

Kernel function plays a role of weighting function in the estimation procedure and it is characterized by its order which indicates both the number of vanishing moments and the number of existing derivatives for the curve being estimated.

The choice of kernel function has less of importance in the appropriate construction of kernel estimator, especially when asymptotic behavior is regarded. It leads to the situation that the analysis of the influence of kernel function on the estimator is overlooked by researchers. Nevertheless, it is easy to notice that in many cases the shape of kernel function has influence on the resulting estimator, especially when graphical presentation of estimator is taking into consideration.

When the order of the kernel function  $k$  is equal to 2 it is called the classical kernel function. In this class of kernel functions there is, among others, quartic kernel function used in the *ROC* estimation and Gaussian kernel function which is one of the mostly used kernels in practical applications. Gaussian kernel function is standardized normal density function and has the form:

$$K(u) = \frac{1}{\sqrt{2\pi}} e^{-\frac{u^2}{2}}.$$

Other kernel functions (classical and nonclassical) are presented in literature e.g.: [2, 13–14]. The class  $S_{\nu,k}$  (for  $0 \leq \nu \leq k$ ) of kernel function  $K$  of order  $k$ , being a real valued function and satisfying  $K \in S_{\nu,k}$ , is defined in the following way [15]:

$$S_{\nu,k} = \left\{ \begin{array}{l} K \in Lip[-1,1], \text{ support}(K) = [-1,1], \\ \int_{-1}^1 x^j K(x) dx = \begin{cases} 0 & \text{for } 0 \leq j \leq k, \quad j \neq \nu, \\ (-1)^\nu \nu! & \text{for } j = \nu, \\ \beta_k(K) \neq 0 & \text{for } j = k. \end{cases} \end{array} \right.$$

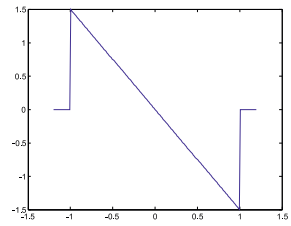
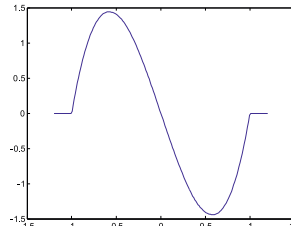
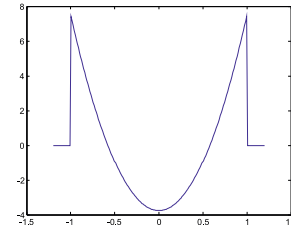
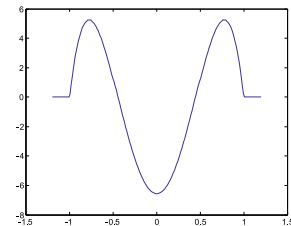
According to this definition, Gaussian kernel does not belong to the class  $S_{\nu,k}$  because of its unbounded support. The class  $S_{\nu,k}$  includes, for example: quartic kernel mentioned earlier ( $\nu = 0, k = 2$ ) and Epanechnikov kernel ( $\nu = 0, k = 2$ ) of the form:

$$K(u) = \begin{cases} \frac{3}{4}(1 - u^2) & \text{for } |u| \leq 1, \\ 0 & \text{for } |u| > 1. \end{cases}$$

Examples of nonclassical kernels (kernels of order  $k > 2$ ) from the class  $S_{\nu,k}$  are presented in Tab. 1. It should be noticed that for even  $k$  kernel functions are symmetric, if  $k$  is odd kernels are asymmetric.

Kernel density estimator based on classical kernel (second order kernel function) is easily explainable. Taking negative values of nonclassical kernel seems to be unappealing feature in estimation procedure. On the other hand, using classical kernel in estimation means that the estimate bias is always of order  $n^{-2/5}$  even when the choice of smoothing parameter is treated as the optimal. It can cause some distortion in graphical representation of structure of the data (for example the number of modes and the height of the density at the modes). Using higher order kernels reduces the amount of estimate bias. In this way nonclassical approach in choosing the shape of kernel function in density estimation provides better properties of the estimator, especially it is significant in finite-sample situations.

Tab. 1: Examples of nonclassical kernel functions from the class  $S_{\nu,k}$ .

Values of $\nu$ and $k$	Kernel function $K(u)$	
$\nu = 1, k = 3$	$K_1(u) = \begin{cases} -\frac{3}{2}u & \text{for }  u  \leq 1, \\ 0 & \text{for }  u  > 1 \end{cases}$	
$\nu = 1, k = 3$	$K_2(u) = \begin{cases} -\frac{15}{4}u(1-u^2) & \text{for }  u  \leq 1, \\ 0 & \text{for }  u  > 1 \end{cases}$	
$\nu = 2, k = 4$	$K_3(u) = \begin{cases} -\frac{15}{4}(1-3u^2) & \text{for }  u  \leq 1, \\ 0 & \text{for }  u  > 1 \end{cases}$	
$\nu = 2, k = 4$	$K_4(u) = \begin{cases} -\frac{105}{16}(1-u^2)(1-5u^2) & \text{for }  u  \leq 1, \\ 0 & \text{for }  u  > 1 \end{cases}$	

#### 4. Smoothing parameter

Smoothing parameter (bandwidth) controls the amount of smoothing in the inference procedure. Hence, the choice of smoothing parameter is treated as most important factor in kernel estimation. Its importance is easy to notice because smoothing parameter affects the features of the estimated functional characteristic of random

variable. Smoothing parameter  $h$  depends on the sample size  $n$  ( $h = h(n)$ ), it is a sequence of a nonrandom positive numbers.

Classical approach of the smoothing parameter choice is represented, among others, by subjective method. In this method different values of parameters are used in some estimation procedures and next this smoothing parameter is taken that fulfills the users' needs and expectations. This method seems to be quite sufficient when the kernel density estimator is only the way of exploring the structure of the data on the initial stage of statistical inference. There is a problem of choosing the appropriate value of smoothing parameter without a priori information about distribution of random variable. Different parameter values in kernel density may indicate, for example, different information about multimodality. Fig. 1 presents the results of kernel density estimation that are constructed using the sample ( $n = 50$ ) taken from population with bimodal asymmetric distribution (mixture of two normal distributions with unequal parameters and weights). In the kernel estimators of density functions Gaussian kernel functions are applied with the following smoothing parameters  $h = 0.05; 0.1; 0.2; 0.3; 0.4; 0.5; 0.6; 0.7; 0.8; 0.9$ .

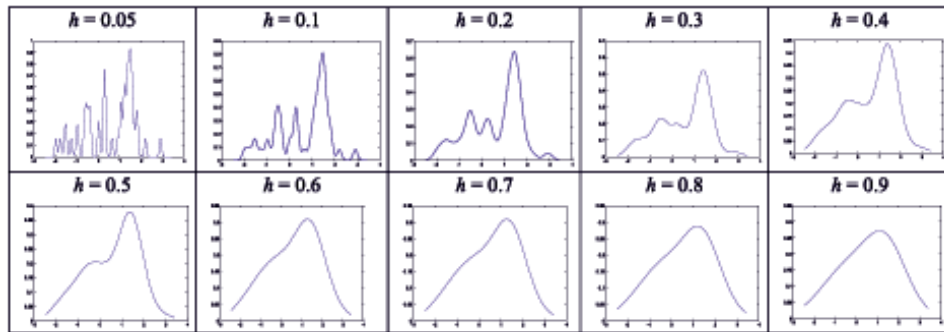


Fig. 1: Kernel density estimators for different values of smoothing parameter.

Small values of smoothing parameters result in “jagged” estimators with a great deal of modes, whereas already for  $h = 0.6$  the estimator of density function becomes strongly unimodal. Exploring several kernel estimators allows to give more insight into the data but it is rather inconvenient to decide, especially for inexperienced users, which value is appropriate in particular research problem.

Another classical method of smoothing parameter choice is a method based on assuming that population from which data are taken has a standard normal distribution. According to this assumption for Gaussian kernel, smoothing parameter, calculated by Silverman's reference rule, has the value

$$\hat{h}_S = 0.9 \min \left( \sigma, \frac{IQ}{1.34} \right) n^{-\frac{1}{5}},$$

where  $\sigma$  is standard deviation,  $IQ$  is interquantile range from the population and may be estimated from the sample  $X_1, \dots, X_n$ . This method works quite good when

the true population is normal, but using this formula in the case of multimodality of density being estimated results in oversmoothing. When this method is used for sample from above example the value of smoothing parameter, calculated by Silverman's rule, is equal to 0.56.

Fully automatic methods of choosing smoothing parameter may be treated as nonclassical ones. They are data-driven methods, in contrast to subjective or Silverman's rule which depend on additional information or assumptions (coming from in most cases from user's experience and knowledge). Their relevance to data makes them more difficult to calculate what results in much longer process of choosing the parameter.

Cross-validation methods are the earliest among automatic methods of choosing the smoothing parameter. The least-squares cross-validation parameter is the following:

$$(6) \quad \hat{h}_{LSCV} = \arg \min LSCV(h),$$

where

$$LSCV(h) = \frac{1}{n^2 h} \sum_{i=1}^n \sum_{j=1}^n K * K \left( \frac{X_j - X_i}{h} \right) - \frac{2}{n(n-1)h} \sum_{i=1}^n \sum_{\substack{j=1 \\ j \neq i}}^n K \left( \frac{X_i - X_j}{h} \right),$$

$$K * K(u) = \int K(u - \nu) K(\nu) d\nu.$$

The biased cross-validation parameter  $\hat{h}_{BCV}$  is as follows:

$$(7) \quad \hat{h}_{BCV} = \arg \min BCV(h),$$

where

$$BCV(h) = \frac{R(K)}{nh} + \frac{h^4 \mu_2^2(K)}{4n^2} \sum_{i=1}^n \sum_{\substack{j=1 \\ j \neq i}}^n K_h^{(2)} * K_n^{(2)}(X_i - X_j),$$

$$R(g) = \int_{-\infty}^{+\infty} g^2(x) dx,$$

$$K_h(X_i - X_j) = \frac{1}{h} K \left( \frac{X_i - X_j}{h} \right).$$

In least squares cross-validation method, the estimation of Mean Integrated Square Error (MISE) is used in choosing the smoothing parameter, whereas in biased cross-validation the asymptotic formula of MISE (AMISE) is involved. The appropriate estimator of AMISE is also used in iterative method of choosing the smoothing parameter. The iterative parameter  $\hat{h}_{IT}$  is:

$$(8) \quad \hat{h}_{IT} = \arg \min AMISE \left\{ \hat{f}(\cdot, h) \right\},$$

where  $AM\hat{I}SE\{\hat{f}(\cdot, h)\}$  is the estimate of AMISE and has the form:

$$AM\hat{I}SE\{\hat{f}(\cdot, h)\} = \frac{R(K)}{nh} + \frac{1}{n^2h} \sum_{i=1}^n \sum_{\substack{j=1 \\ j \neq i}}^n (K * K * K * K - 2K * K * K + K * K) \left( \frac{X_i - X_j}{h} \right).$$

Plug-in method of smoothing parameter choosing belongs to class of nonclassical methods though Silverman's reference rule can be treated as the simplest possible plug-in method. In minimization of AMISE of kernel density estimator unknown  $\int_{-\infty}^{+\infty} (f'')^2(u) du$  in Silverman's reference rule is estimated with assumption that  $f$  belongs to a family of normal distributions. Refined version of estimation of  $\int_{-\infty}^{+\infty} (f'')^2(u) du$  leads to nonclassical plug-in methods. There is a possibility of direct, nonparametric estimation of this term, by using kernel estimate of  $f$  and taking the second derivative from this estimate. The direct plug-in smoothing parameter is the following:

$$(9) \quad \hat{h}_{PI} = \left[ \frac{\gamma_{0k}^{2k+1} (k!)^2}{2nk(-1)^k \hat{\psi}_k(g)} \right]^{\frac{1}{2k+1}},$$

where  $\gamma_{0k}$  is the canonical factor of kernel function  $K$ , i.e.:

$$\gamma_{0k} = \left( \frac{\int_{-\infty}^{+\infty} K^2(u) du}{\mu_k^2(K)} \right)^{\frac{1}{2k+1}},$$

$\hat{\psi}_k(g)$  is the kernel estimator with kernel function  $L$  and the initial smoothing parameter  $g$ , i.e.:

$$\hat{\psi}_k(g) = \frac{1}{n^2g} \sum_{i,j=1}^n L^{(2k)} \left( \frac{X_i - X_j}{g} \right).$$

## 5. Simulation study

In order to evaluate properties of chosen nonclassical methods of choosing kernel density estimation parameters, a study was carried out using simulation methods. From populations with densities being mixtures of normal distributions, samples were chosen and kernel density estimators were calculated. Values of smoothing parameters were compared taken into account different kernel functions (classical and nonclassical) and the resulting density estimators are presented. An attempt to compare nonclassical methods with classical ones was made in appropriate types of densities shapes of populations.

The population density is described by density function:

$$f(x) = \alpha \varphi(x|\mu_1, \sigma_1) + (1 - \alpha) \varphi(x|\mu_2, \sigma_2),$$

where  $\varphi(x|\mu_i, \sigma_i)$  ( $i = 1, 2$ ) is normal density function with mean  $\mu_i$  and standard deviation  $\sigma_i$ , i.e.:

$$\varphi(x|\mu, \sigma) = \frac{1}{\sigma\sqrt{2\pi}} e^{-\frac{(x-\mu)^2}{2\sigma^2}},$$

$\alpha \in \langle 0, 1 \rangle$  is a mixture coefficient. In the simulation study the following values of normal distributions are regarded:

$$\begin{aligned} \mu_1 &= 0, & \mu_2 &= 1.5; \\ \sigma_1 &= 1, & \sigma_2 &= 0.333. \end{aligned}$$

Taking different values of mixture coefficients, i.e.  $\alpha = 0, 0.05, 0.10, 0.15, \dots, 0.90, 0.95$  the simulation study is widened to regard different shapes of population density functions (evident unimodal to multimodal and symmetric to asymmetric). In this way, the so-called Gaussians mixtures (populations P1–P20) are only considered but with diversified both level of density modality and level of density skewness. Histograms for populations for chosen values of mixture coefficients are presented in Fig. 2–3.

Population is unimodal and symmetric only in one case, for  $\alpha = 0$ . Other populations (for  $\alpha \neq 0$ ) are left-skewed. Asymmetry is stronger for smaller values of mixture coefficients, but for the bigger  $\alpha$ , the bimodality is easier to notice.

The values of smoothing parameters for sample size  $n = 100$  and for chosen values of mixture coefficients are presented in Tab. 2–5.

As can be seen, value of smoothing parameter in kernel density estimator depends not only on the population density shape but also on kernel function used in density estimator. When sample comes from unimodal and symmetric population, the bandwidths are in most cases smaller than in bimodal and asymmetric populations. The stronger the population asymmetry is, the bigger smoothing parameter is used.

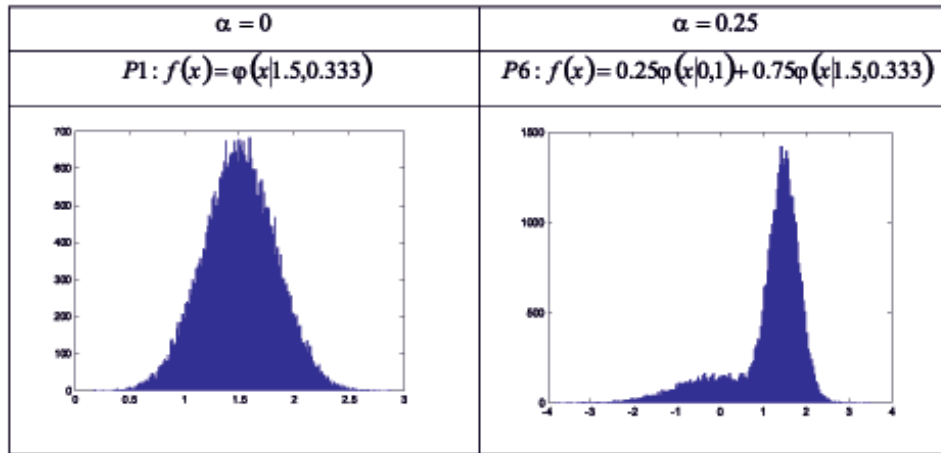
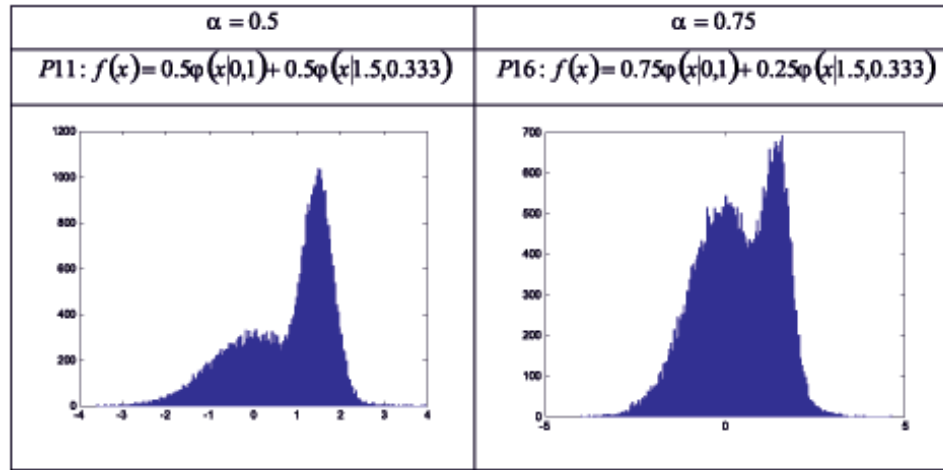


Fig. 2: Populations histograms (P1 and P6) for chosen values of  $\alpha$ .



Fig. 3: Populations histograms (P11 and P16) for chosen values of  $\alpha$ .Tab. 2: Values of smoothing parameters (sample from P1, sample size  $n = 100$ ).

Kernel function	Smoothing parameter				
	$\hat{h}_S$	$\hat{h}_{LSCV}$	$\hat{h}_{BCV}$	$\hat{h}_{IT}$	$\hat{h}_{PI}$
Gaussian	0.13	0.14	0.18	0.15	0.17
$K_1(u)$	0.30	0.01	0.61	0.44	0.56
$K_2(u)$	0.39	0.01	0.02	0.01	0.01
$K_3(u)$	0.38	0.15	0.77	0.65	0.40
$K_4(u)$	0.47	0.22	0.03	0.02	0.50

Tab. 3: Values of smoothing parameters (sample from P6, sample size  $n = 100$ ).

Kernel function	Smoothing parameter				
	$\hat{h}_S$	$\hat{h}_{LSCV}$	$\hat{h}_{BCV}$	$\hat{h}_{IT}$	$\hat{h}_{PI}$
Gaussian	0.23	0.09	0.18	0.15	0.25
$K_1(u)$	0.52	0.76	1.07	0.36	0.51
$K_2(u)$	0.69	1.08	0.15	0.11	0.73
$K_3(u)$	0.67	0.32	1.35	1.01	0.64
$K_4(u)$	0.83	0.41	0.05	0.02	0.79

Moreover, smaller values of bandwidth are used when asymmetric kernel functions are applied in density estimators. It can be seen especially in the case of the cross-validation methods of choosing the smoothing parameters. Nonclassical kernel function  $K_2(u)$  is that one for which the bandwidth calculated by classical method (Silverman's reference rule) is significantly bigger. In almost all regarded populations

there are similar values of Silverman's reference rule and plug-in method of choosing the smoothing parameter.

Tab. 4: Values of smoothing parameters (sample from P11, sample size  $n = 100$ ).

Kernel function	Smoothing parameter				
	$\hat{h}_S$	$\hat{h}_{LSCV}$	$\hat{h}_{BCV}$	$\hat{h}_{IT}$	$\hat{h}_{PI}$
Gaussian	0.44	0.01	0.96	0.18	0.44
$K_1(u)$	1.01	0.06	2.05	0.39	1.06
$K_2(u)$	1.32	0.06	0.12	0.09	1.33
$K_3(u)$	1.29	0.29	2.60	2.02	1.09
$K_4(u)$	0.44	0.01	0.96	0.19	0.44

Tab. 5: Values of smoothing parameters (sample from P16, sample size  $n = 100$ ).

Kernel function	Smoothing parameter				
	$\hat{h}_S$	$\hat{h}_{LSCV}$	$\hat{h}_{BCV}$	$\hat{h}_{IT}$	$\hat{h}_{PI}$
Gaussian	0.41	0.51	0.51	0.48	0.55
$K_1(u)$	0.92	1.88	1.88	1.25	1.02
$K_2(u)$	1.21	0.08	0.35	0.29	1.25
$K_3(u)$	1.18	0.33	2.38	2.12	1.36
$K_4(u)$	1.45	1.45	0.16	0.09	1.67

The kernel density estimators for chosen classical and nonclassical parameters (sample size  $n = 100$ ) and chosen values of mixture coefficients for populations (P1, P6, P11, P16) are presented in Fig. 4.

Using nonclassical kernels functions in kernel density estimators may result in negative values of density estimators, as it is in the case of regarded samples, what may be not appealing to users. Furthermore, it is easy to notice that these nonclassical kernel functions influence on the shape of estimator in a large scale. This is rather a rule, regardless of the population properties from which the samples are taken.

## 6. Conclusions

Classical kernel parameters applied in density estimation are easy to use, the process of computation is short but their usage is based on assumptions which are not sometimes fulfilled. For example, Silverman's reference rule works good when the population distribution is normal and the kernel function is Gaussian. Applying nonclassical kernel parameters does not always improve the resulting density estimator, what is noticeable especially when graphical presentation is taking into consideration. But using different parameters (classical and nonclassical) is certainly advantageous because it widens user's knowledge of analyzed phenomena.

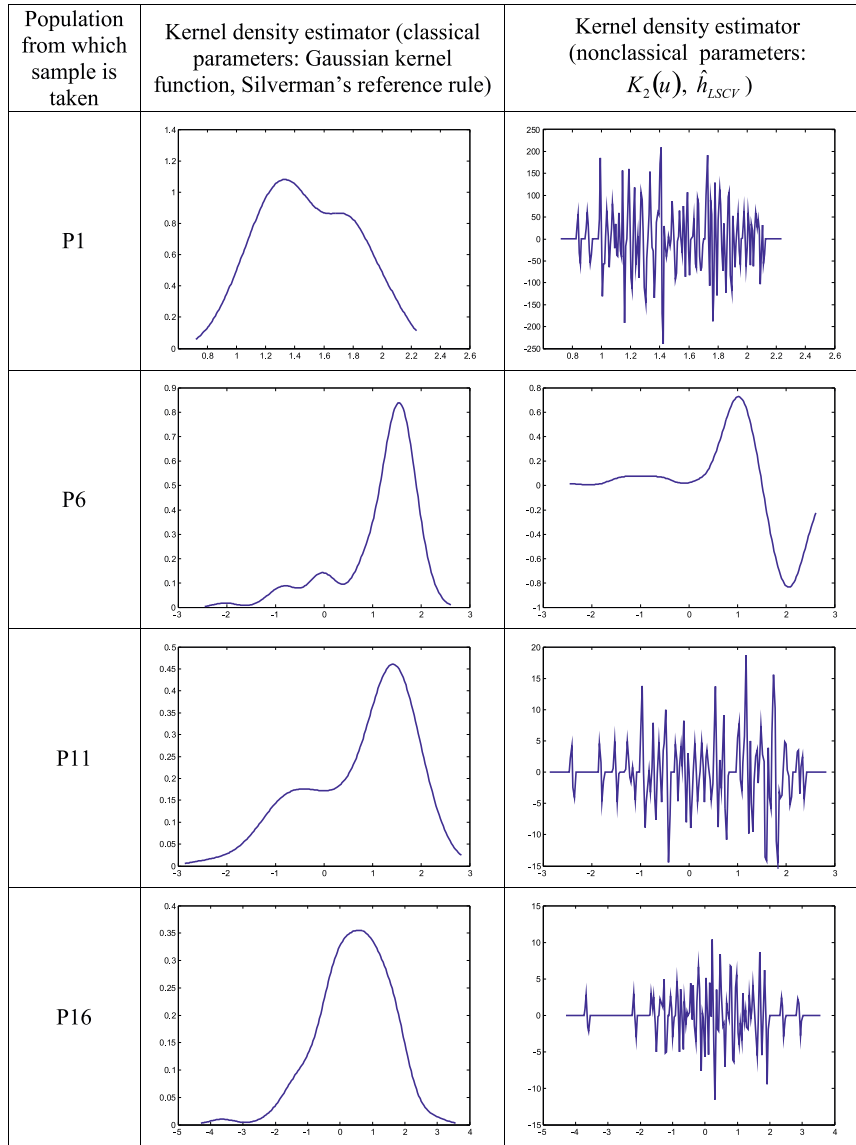


Fig. 4: Density kernel estimators for classical and nonclassical kernel parameters for samples from populations P1, P6, P11 and P16.

## References

- [1] C. Domański, *Statystyczne testy nieparametryczne*, Państwowe Wydawnictwo Ekonomiczne, Warszawa 1997.
- [2] C. Domański and K. Pruska, *Nieklasyczne metody statystyczne*, Państwowe Wydawnictwo Ekonomiczne, Warszawa 2000.

- [3] J. D. Gibbons and S. Chakraborti, *Nonparametric Statistical Inference*, Marcel Dekker, Inc., New York 2003.
- [4] Q. Li and J. S. Racine, *Nonparametric Econometrics. Theory and Practice*, Princeton University Press, Princeton and Oxford 2007.
- [5] A. Baszczyńska, *Estymacja funkcji gęstości z pakietem MATLAB*, Rola informatyki w naukach ekonomicznych i społecznych. Innowacje i implikacje interdyscyplinarne (2012), 7–16.
- [6] A. Baszczyńska, *Test symetryczności Li*, Acta Universitatis Lodziensis. Folia Oeconomica **271** (2012), 99–105.
- [7] A. Baszczyńska, *Some remarks on the symmetry kernel test*, Acta Universitatis Lodziensis. Folia Oeconomica **285** (2013), 21–29.
- [8] E. Parzen, *On estimation of a probability density function and mode*, The Annals of Mathematical Statistics **33**, no. 3 (1962), 1065–1075.
- [9] M. Rosenblatt, *Remarks on some nonparametric estimates of a density function*, The Annals of Mathematical Statistics **27**, no. 3 (1956), 832–837.
- [10] B. W. Silverman, *Density Estimation for Statistics and Data Analysis*, Chapman & Hall, London 1996.
- [11] M. P. Wand and M. C. Jones, *Kernel Smoothing*, Chapman & Hall, London 1995.
- [12] P. Kulczycki, *Estymatory jądrowe w analizie systemowej*, Wydawnictwa Naukowo-Techniczne, Warszawa 2005.
- [13] W. Härdle, *Smoothing Techniques with Implementation to S*, Springer-Verlag, New York 1990.
- [14] W. Härdle, M. Müller, S. Sperlich, and A. Werwatz, *Nonparametric and Semiparametric Models*, Springer, Berlin 2004.
- [15] I. Horová, J. Koláček, and J. Zelinka, *Kernel Smoothing in MATLAB. Theory and Practice of Kernel Smoothing*, World Scientific, New Jersey 2012.

Department of Statistical Methods  
University of Łódź  
Rewolucji 1905 41, PL-90-214 Łódź  
Poland  
e-mail: albasz@uni.lodz.pl

Presented by Julian Ławrynowicz at the Session of the Mathematical-Physical Commission of the Łódź Society of Sciences and Arts on October 29, 2015

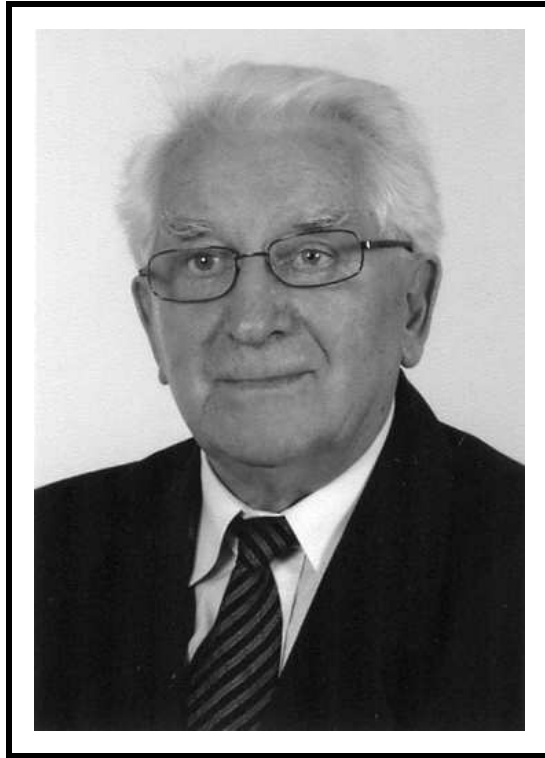
## NIEKLASYCZNE PARAMETRY W ESTYMACJI JĄDROWEJ

### S t r e s z c z e n i e

W metodzie jądrowej, stosowanej w estymacji oraz weryfikacji hipotez statystycznych, konieczne jest ustalenie dwóch parametrów metody: funkcji jądra i parametru wygładzania. W pracy przedstawiono wybrane metody (klasyczne i nieklasyczne) wyboru parametrów metody jądrowej. Dokonano porównania własności omawianych metod, opierając się na wynikach badania symulacyjnego.

*Słowa kluczowe:* metoda jądrowa, funkcja jądra, parametr wygładzania, estymacja

## OBITUARY



On March 3, 2016 Professor **Leon Mikołajczyk** (\*1929),  
our close friend and collaborator, ordinary member  
of the Łódź Society of Sciences and Arts, has passed away.  
We keep him in our hearts.



## Rapporteurs – Referees

Aleksander Bakhtin (Kyiv)	Sergey Plaksa (Kyiv)
Daniel Baldomir (Santiago de Compostela)	Yaroslav G. Prytula (Kyiv)
Richard A. Carhart (Chicago)	Jakub Rembieliński (Łódź)
Stancho Dimiev (Sofia)	Carlos Rentería Marcos (México, D.F.)
Paweł Domański (Poznań)	Stanisław Romanowski (Łódź)
Mohamed Saladin El Nashie (London)	Monica Roşiu (Craiova)
Janusz Garecki (Szczecin)	Jerzy Rutkowski (Łódź)
Ryszard Jajte (Łódź)	Ken-Ichi Sakan (Osaka)
Zbigniew Jakubowski (Łódź)	Hideo Shimada (Sapporo)
Jan Janas (Kraków)	David Shoikhet (Karmiel, Israel)
Tomasz Kapitaniak (Łódź)	Józef Siciak (Kraków)
Grzegorz Karwasz (Toruń)	Francesco Succi (Roma)
Leopold Koczan (Lublin)	Osamu Suzuki (Tokyo)
Ralitza K. Kovacheva (Sofia)	Józef Szudy (Toruń)
Radosław Kycia (Kraków)	Luis Manuel Tovar Sánchez (México, D.F.)
Dominique Lambert (Namur)	Massimo Vaccaro (Salerno)
Andrzej Łuczak (Łódź)	Anna Urbaniak-Kucharczyk (Łódź)
Cecylia Malinowska-Adamska (Łódź)	Krzysztof Warda (Łódź)
Stefano Marchiafava (Roma)	Władysław Wilczyński (Łódź)
Andrzej Michalski (Lublin)	Hassan Zahouani (Font Romeu)
Dariusz Partyka (Lublin)	Lawrence Zalcman (Ramat-Gan)
Adam Paszkiewicz (Łódź)	Mariusz Zubert (Łódź)

## CONTENU DU VOLUME LXVI, no. 2

1. <b>A. Bakhtin, I. Dvorak and I. Denega</b> , Separating transformation and extremal decomposition of the complex plane .....	ca. 8 pp.
2. <b>J. Garecki</b> , Canonical superenergy density and local gravitational stability .....	ca. 12 pp.
3. <b>A. S. Serdyuk and T. A. Stepanyuk</b> , Estimates for approximations by Fourier sums, best approximations and best orthogonal trigonometric approximations of the classes of $(\psi, \beta)$ -differentiable functions .....	ca. 8 pp.
4. <b>O. Suzuki</b> , Binary and ternary structures in physics. I. The hierarchy structure in Turing machine in physics .....	ca. 16 pp.
5. <b>K. Warda, D. Baldomir, M. Pereiro, J. Arias, V. Pardo, and J. Botana</b> , Magnetoresistance in thin films uncluding the domain structure .....	ca. 14 pp.
6. <b>S. Artemi, A. Maidou, N. Dintsios, and H. M. Polatoglou</b> , Physical processes of energy transfer related to everyday life experiences .....	ca. 20 pp.
7. <b>J. Hejduk, W. Wilczyński, and W. Wojdowski</b> , On semi-regularization of the density-type topologies .....	ca. 10 pp.
8. <b>A. Makarewicz, W. Mozgawa, and P. Pikuta</b> , Volumes of polyhedra in terms of determinants of rectangular matrices ...	ca. 14 pp.
9. <b>O. Chojnacka and A. Lecko</b> , On the differential subordination of harmonic mean to a linear function .....	ca. 9 pp.
10. <b>A. Bojarska and A. Niemczynowicz</b> Integral equations in Puzyna's teaching and research as seen today .....	ca. 16 pp.